Geological Society of America Bulletin, published online on 29 July 2015 as doi:10.1130/B31269.1

Late Quaternary slip-rate along the central Bangong-Chaxikang segment of the Karakorum fault, western Tibet

Marie-Luce Chevalier[1,2,†], Jérôme Van der Woerd[3], Paul Tapponnier[2,4], Haibing Li[1], Frederick J. Ryerson[5], and Robert C. Finkel[6]

[1]*State Key Laboratory of Continental Tectonics and Dynamics, Institute of Geology, Chinese Academy of Geological Sciences, 26 Baiwanzhuang Road, Beijing 100037, People's Republic of China*

[2]*Laboratoire de Tectonique et Mécanique de la Lithosphère, Institut de Physique du Globe de Paris, 1, rue Jussieu, 75238 Paris cedex 05, France*

[3]*Institut de Physique du Globe de Strasbourg, UMR 7516 CNRS, Université de Strasbourg, 5 rue Descartes, 67084 Strasbourg cedex, France*

[4]*Earth Observatory of Singapore, 50 Nanyang Avenue, N2-01a-09, 639798, Singapore*

[5]*L-231, Atmospheric, Earth and Energy Division, Physical and Life Sciences Directorate, Lawrence Livermore National Laboratory, Livermore, California 94550, USA*

[6]*Earth and Planetary Science Department, University of California–Berkeley, 371 McCone Hall, Berkeley, California 94720, USA*

ABSTRACT

Insight into the spatial and temporal changes of slip-rate is essential to understand the kinematic role of large strike-slip faults in continental collision zones. Geodetic and geologic rates from present to several million years ago along the Karakorum fault range from 0 to 11 mm/yr. Here, we determine the first late Quaternary slip-rate at the southern end of the linear Bangong-Chaxikang segment of the Karakorum fault, using cumulative offsets (20–200 m) of fans and terraces at three sites, as well as 74 new ^{10}Be surface-exposure ages to constrain the age of these offset geomorphic markers. The rate is >3 mm/yr at sites Gun and Chaxikang, and it is >1.7–2.2 mm/yr at the Gar fan site. Together with rates obtained along the southernmost Menshi-Kailas segment, the Karakorum fault slip-rate seems to increase southeastward from south of Bangong Lake to Kailas (from >3 to >8 mm/yr). These Karakorum fault slip-rate data (>3–8 mm/yr), together with the total length of the fault (>1000 km) and its initiation age (>13–23 Ma), confirm that the Karakorum fault is the major fault accommodating dextral strike-slip motion NE of the western Himalayas. The dextral Karakorum fault in the south and the conjugate left-lateral Longmu Co–Altyn Tagh fault system in the north are thus the major strike-slip faults of western Tibet, which contribute to eastward extrusion of Tibet.

[†]mlchevalier@hotmail.com

INTRODUCTION

Detailed studies of the major intracontinental strike-slip faults in Tibet, and of the Karakorum fault in particular, are important to improve our understanding of the tectonics of Central Asia. Specifically, it is essential to determine whether deformation following the India-Asia collision is mostly localized along a few large structures (block model), with significant lateral transfer of material along strike-slip faults (e.g., Armijo et al., 1986, 1989; Peltzer and Tapponnier, 1988; Peltzer et al., 1989; Avouac and Tapponnier, 1993; Leloup et al., 2001; Tapponnier et al., 2001; Replumaz and Tapponnier, 2003), or if deformation is mostly distributed on numerous secondary structures (continuous deformation model) with minor lateral transfer along faults (e.g., Bendick et al., 2000; England and Molnar, 2005). Some studies (e.g., Flesch and Bendick, 2007; Meade, 2007a, 2007b; Thatcher, 2007, 2009; Loveless and Meade, 2011) suggest that existing velocity fields and geologic rates on active faults in Asia are still too sparse and poorly constrained (both spatially and temporally) to discriminate between these two end-member models. Therefore, in order to quantify the kinematic role of the main active faults in the India-Asia collision zone, it is essential to obtain new accurate slip-rate data at different time scales and locations along these faults.

Determining the slip-rates along the major strike-slip faults on the Tibetan Plateau has been the focus of numerous field studies in the past 20 yrs (e.g., Peltzer and Tapponnier, 1988; Gaudemer et al., 1995; Van der Woerd et al., 1998, 2002; Mériaux et al., 2004, 2005, 2012; Chevalier et al., 2005a, 2005b, 2011b, 2012, 2015a, 2015b; Cowgill, 2007; Kirby et al., 2007; Gold et al., 2011). Along the Altyn Tagh fault, for instance, the longest strike-slip fault in Asia bounding northern Tibet (inset Fig. 1), some studies have highlighted consistent geodetic (global positioning system [GPS] or interferometric synthetic aperture radar [InSAR]; e.g., Chen et al., 2000; Wang et al., 2001; Wallace et al., 2004; Zhang et al., 2004) and geologic rates along its central segment (e.g., Cowgill, 2007; Thatcher, 2007; Zhang et al., 2007; Cowgill et al., 2009), while other studies have obtained faster late Pleistocene to Holocene slip-rates when compared to geodetic rates (e.g., Mériaux et al., 2004, 2005, 2012; Xu et al., 2005; Hanks and Thatcher, 2006; Ryerson et al., 2006), suggesting millennial-scale slip-rate variations (e.g., Friedrich et al., 2003; Bennet et al., 2004). At the geological scale, zircon dating of offset conglomerates indicates slip-rate decrease from the early Miocene to present from about >20 mm/yr to ~5–15 mm/yr, highlighting long-term slip-rate changes (Yue et al., 2003).

The slip-rate of the >1000 km long right-lateral Karakorum fault (Fig. 1) is also debated (Fig. 2; Table 1). At short time scales, InSAR data suggest a rate of 1 ± 3 mm/yr (Wright et al., 2004) or <0–6 ± 2 mm/yr (with the highest rate being in the central portion, near the intersection with the Longmu–Gozha Co fault; Fig. 1; Wang and Wright, 2012), and GPS data yield between 3 and 7 mm/yr (Chen et al., 2004; Jade et al., 2004, 2010; Kundu et al., 2014) and up

GSA Bulletin; doi: 10.1130/B31269.1; 18 figures; 3 tables.

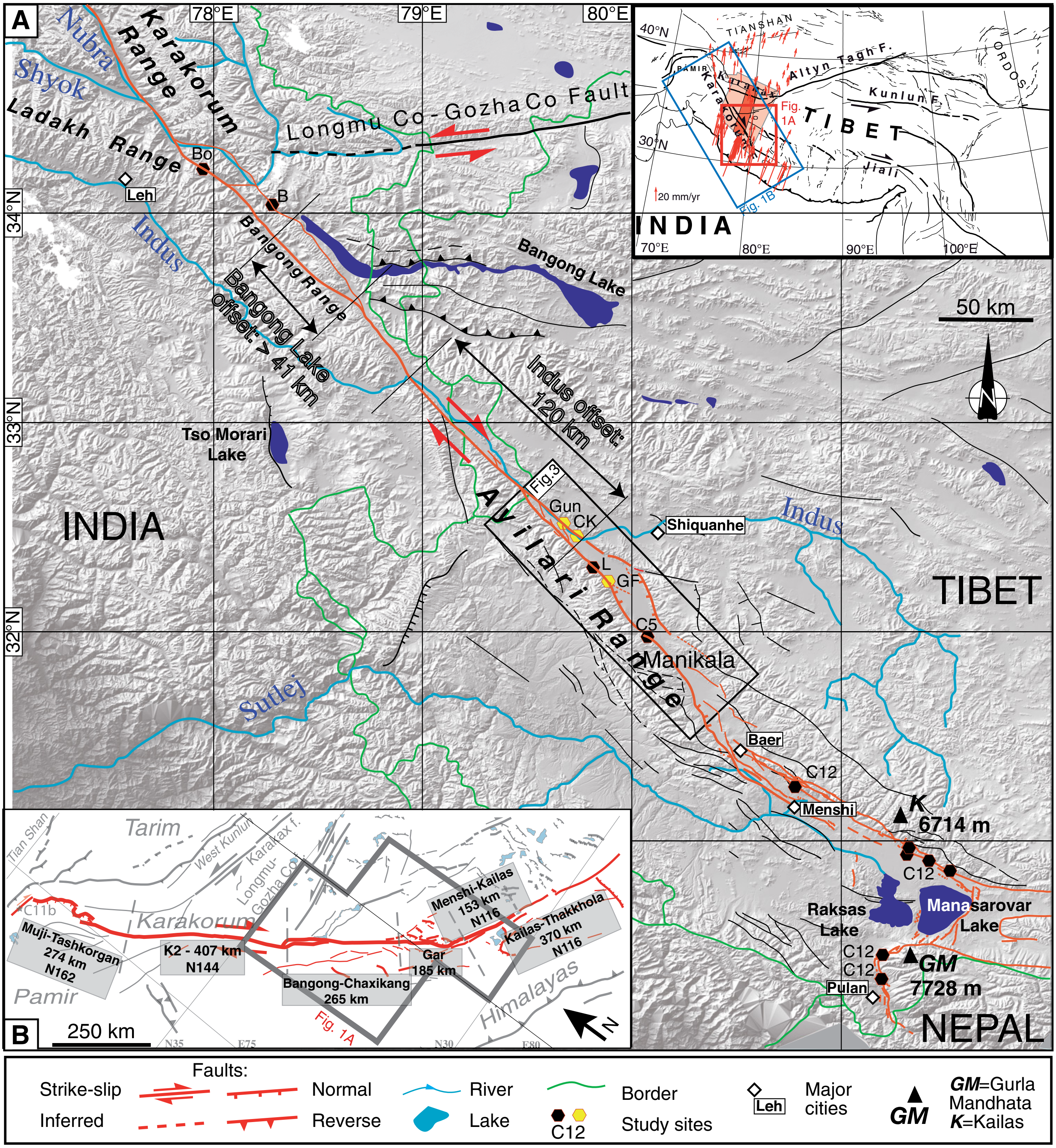

Figure 1. (A) Map of southern Karakorum fault (KF), showing active branches of the Karakorum fault zone (in red) and other faults (in black), as well as main landmarks along Bangong-Chaxikang and Gar Basin segments (Chevalier et al., 2005a). Yellow hexagons locate sites from this study, while black hexagons locate previous studies: B—Brown et al. (2002), Bo—Bohon (2014), L—Lacassin et al. (2004), C5—Chevalier et al. (2005a), C12—Chevalier et al. (2012). Note the 120 km offset of the Indus River (Gaudemer et al., 1989) and the >41 km offset of Bangong Lake (Liu, 1993). (B) First-order geometrical segmentation based on fault trace bends, step-overs, and fault junctions. C11b—Chevalier et al. (2011b). Inset is location of Karakorum fault within India-Asia collision zone. Red arrows are subset of representative global positioning system (GPS) velocities relative to stable Siberia (Gan et al., 2007). Shaded polygons show approximate locations of interferometric synthetic aperture radar (InSAR) swaths of Wright et al. (2004) and Wang and Wright (2012).

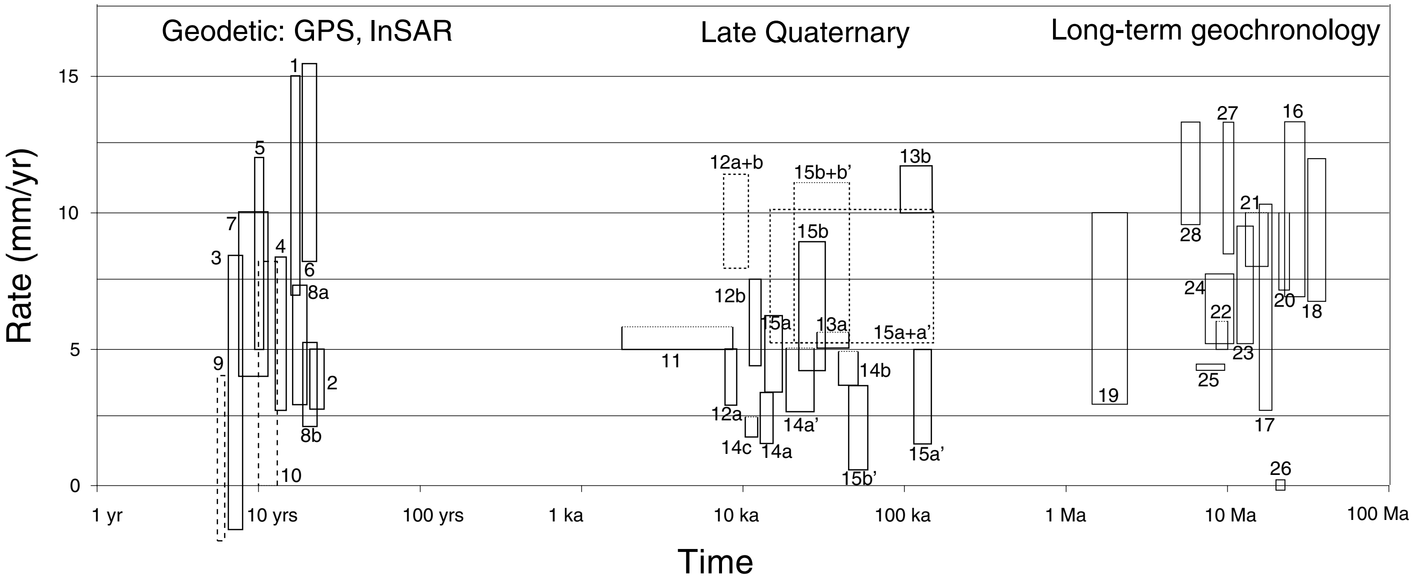

Figure 2. Karakorum fault slip-rates vs. time for geodetic (plain for global positioning system [GPS]; dashed for interferometric synthetic aperture radar [InSAR]), late Quaternary (plain for one fault branch; dashed for two), and long-term geochronology time scales. See Table 1 for a list of plotted studies.

to ~11 mm/yr (Banerjee and Bürgmann, 2002; H. Wang et al., 2011).

At the late Quaternary time scale, correlating the emplacement of offset geomorphic surfaces with climatic periods (no actual dates at that time), Liu (1993) inferred a slip-rate of ~18–35 mm/yr. Using ^{10}Be dating near Bangong Lake, Brown et al. (2002) obtained a Holocene slip-rate of 4 ± 1 mm/yr on the northern Bangong strand ("B" in Fig. 1), and Bohon (2014) suggested 5.6 (+1.7/–1.1) mm/yr on the southern Tangtse strand (33–5.7 ka; "Bo" in Fig. 1), together suggesting a possible Karakorum fault post–marine isotope stage (MIS) 3 (ca. 40 ka) slip-rate of ~10 mm/yr near Bangong Lake across the two branches, assuming that they were active at the same time. Bohon (2014), however, suggested that this was the case during the period 30–6 ka but not anymore (since 6 ka, slow rates at Tangtse and fast rates at Bangong). Using ^{10}Be dating, Chevalier et al. (2005a, 2005b) determined a late Quaternary slip-rate of 10.7 ± 0.7 mm/yr (for the last ~300 ka) further south along the Gar Basin at Manikala. Taking the oldest age among the moraine surface samples at this same site, Brown et al. (2005) suggested the possibility of a slower rate. The ~11 mm/yr rate is 2–10 times faster than InSAR rates and 2–3 times faster than the slowest GPS rates, leading Chevalier et al. (2005a, 2005b) to suggest secular slip-rate variations due to measurements over different periods of the earthquake cycle in relation to crust and mantle rheology below the seismogenic zone (Savage and Prescott, 1978; Segall, 2002; Perfettini and Avouac, 2004). Indeed, geodetic rates are sensitive to the variations in the earthquake cycle and might underestimate slip-rates if measured only over the interseismic interval, or if the fault is late in its earthquake cycle. In contrast, late Quaternary rates most certainly span multiple cycles, therefore minimizing postseismic relaxation or interseismic strain accumulation. In addition, there are no recorded nor historic earthquakes along the Karakorum fault, suggesting that it might be in the last phase of its seismic cycle. Chevalier et al. (2012) determined a late Quaternary (ca. 200 ka) rate of >7–8 mm/yr across the two main branches of the Karakorum fault along its southernmost segment, in the Menshi-Kailas Basin, and suggested, in the absence of along-strike slip-rate gradient, that the Karakorum fault does not end east of Kailas but probably extends eastward along the Yarlung Zangbo suture (Peltzer and Tapponnier, 1988; Lacassin et al., 2004). It has also been proposed that the fault extends southeastward along the Gurla Mandhata–Humla fault system (e.g., Armijo et al., 1989; Chen et al., 2004; Lacassin et al., 2004; Murphy and Copeland, 2005; Styron et al., 2011; McCallister et al., 2014), and even to the Main Frontal thrust through the Western Nepal fault system, delimiting a western Himalayan wedge sliver (Murphy et al., 2014). Further north in the Pamir, along the Muji-Tashkorgan fault zone of the Kongur Shan extensional system, right-lateral separation between the western Himalaya-Pamir and Tibet-Tarim was determined for the Holocene at ~5 mm/yr along the main Muji fault in the north, and possibly at >9 mm/yr across the entire fault system (Chevalier et al., 2011b). While a direct connection between the Kongur Shan extensional system and the Karakorum fault to the south is questioned (Robinson et al., 2007, 2015; Robinson, 2009a), this extensional right-lateral fault system accommodates right-lateral movement between the Pamir and the western Tarim (e.g., Liu, 1993; Ratschbacher et al., 1994; Murphy et al., 2000; Chevalier et al., 2011b, 2015b).

At the long-term time scale (millions of years), the rates range from 0 mm/yr (Robinson, 2009b) north of Bangong Lake to 27 mm/yr (Valli et al., 2008), even though most studies suggest a rate around 5–13 mm/yr (Fig. 2; e.g., Murphy et al., 2000; Lacassin et al., 2004; Phillips et al., 2004; Rutter et al., 2007; Valli et al., 2007, 2008; Robinson, 2009a; S. Wang et al., 2009, 2011, 2012; Boutonnet et al., 2012, 2013; Gourbet et al., 2015).

Here, we document the first quantitative geomorphologic and chronologic data from sites located NW of the study conducted by Chevalier et al. (2005a, 2005b), along the Bangong-Chaxikang and Gar Basin segments (Fig. 1), which are inaccessible today. This segment is unique in the sense that it is the only segment along the entire Karakorum fault that is purely linear (not transpressive nor transtensive, no change of direction, one single main fault, etc.). It has long been studied to constrain long-term slip-rates and initiation age of the Karakorum fault (e.g., Valli et al., 2007), especially due to the presence of the 120 km offset of the Indus River (Gaudemer et al., 1989). Measuring geomorphic offsets across the main branch of the

TABLE 1. SUMMARY OF STUDIES PLOTTED IN FIGURE 18C

Number	Rate (mm/yr)	Notes	Reference
Geodetic global positioning system (GPS)			
1	11 ± 4		Banerjee and Bürgmann (2002)
2	4 ± 1		Chen et al. (2004)
3	3–3.4 ± 5		Jade et al. (2004, 2010)
4	3 ± 0.1–8	Joint geodetic-geologic inversion	Loveless and Meade (2011)
5	5–12	Two-dimensional, linear elastic, deformable microplate model for the upper crust, based on the behavior of an idealized earthquake cycle.	Langstaff and Meade (2013)
6	11.6 ± 3.7		H. Wang et al. (2011)
7	7 ± 3		Zhang et al. (2004)
8a	5 ± 2	NW of 79°E	Kundu et al. (2014)
8b	3.6 ± 1.5	SE of 79°E	Kundu et al. (2014)
Geodetic interferometric synthetic aperture radar (InSAR)			
9	1 ± 3		Wright et al. (2004)
10	<0–6 ± 2		Wang and Wright (2012)
Late Quaternary			
11	>5	One strand at Muji	Chevalier et al. (2011b)
12a	4 ± 1	One strand at Bangong	Brown et al. (2002)
12b	5.6 (+1.9/–1.2)	One strand at Tangtse	Bohon (2014)
12a + 12b	9.6 (+2.1/–1.6)	Two strands (Bangong and Tangtse)	Brown et al. (2002) and Bohon (2014)
13a	>5.4	One strand at Manikala if oldest age	Chevalier et al. (2005a, 2005b)
13b	10.7 ± 0.7	One strand at Manikala if mean age	Chevalier et al. (2005a, 2005b)
14a	2.5 ± 1	One strand at Gun (smaller offset)	This study
14a′	>3.8 (+1.5/–1.1)	One strand at Gun (larger offset)	This study
14b	>3.4	One strand at Chaxikang	This study
14c	>1.7–2.2	One strand at Gar fan	This study
15a	4.7 (+1.8/–1.4)	KRFF at Menshi	Chevalier et al. (2012)
15a′	2.4 (+2.6/–0.8)	DF at Menshi	Chevalier et al. (2012)
15a + 15a′	7.1 (+3.2/–1.7)	Two strands at Menshi	Chevalier et al. (2012)
15b	6.4 (+2.4/–2.3)	KRFF at Kailas	Chevalier et al. (2012)
15b′	1.5 (+2.1/–0.9)	DF at Kailas	Chevalier et al. (2012)
15b + 15b′	>7.9 (+3.2/–2.5)	Two strands at Kailas	Chevalier et al. (2012)
Long-term geochronology			
16	10 ± 3	250–400 km offset, 23–32 Ma	Lacassin et al. (2004)
17	2.7–10.2	40–150 km offset, 14–16 Ma	Phillips et al. (2004)
18	6.89 ± 0.8–10.8 ±1.3	149–167 km offset	Robinson (2009a)
19	3–10	3–5 Ma	Rutter et al. (2007)
20	>8.5 ± 1.5	120 km Indus River offset, 14 Ma	Valli et al. (2007)
21	>8–10 (south) and <27 (north)	>200–240 km and ~480 km offset, 13–23 Ma	Valli et al. (2008)
22	>5	66 km offset, 13 Ma	Murphy et al. (2000)
23	7.3 ± 1.8	100 km offset, 12 Ma	S. Wang et al. (2009)
24	6.4 ± 1.3	13 Ma	S. Wang et al. (2011)
25	4.5 ± 0.1	52 ± 2 km offset, 12 Ma	S. Wang et al. (2012)
26	0	0 km offset	Robinson (2009b)
27	8.4–13	200–240 km offset, 22.7 Ma	Boutonnet et al. (2012)
28	9–13	Quartz-strain-rate (QSR) method, at Tangtse	Boutonnet et al. (2013)

Note: KRFF—Kailas range-front fault; DF—Darchen fault.

Karakorum fault and constraining their ages with ^{10}Be cosmogenic surface-exposure dating of alluvial surfaces allowed us to determine its slip-rate at the longitude of ~80°E. We then compared our rate with that on other segments of the Karakorum fault and at different time scales. Eventually, these types of studies may shed light on whether deformation in Tibet is mostly localized or distributed.

REGIONAL ACTIVE TECTONICS

The Karakorum fault extends from the Pamir to Mount Kailas and can be divided into six segments based on major bends and fault junctions (Fig. 1B). The Muji-Tashkorgan segment, possibly the northernmost segment of the Karakorum fault (Chevalier et al., 2011b, 2015b), is ~270 km long with a mainly normal component of motion along the Kongur Shan extensional system of the Pamir (Fig. 1B; Liu, 1993; Brunel et al., 1994) between the strike-slip segments of Muji and K2. The longest segment (K2, ~400 km long from southern Pamir to Bangong Lake; Fig. 1B) is located in remote northern India at very high elevation and near politically unstable borders, and it is thus barely accessible. This transpressional segment, as suggested by fault branches with both thrust and strike-slip kinematics (e.g., Searle et al., 1998; Raterman et al., 2007), lies in a deeper and narrower valley than the transtensional segments to the south and helped raise the second highest mountain in the world (K2 in the Karakorum Range; e.g., Searle et al., 1998). Based on satellite image interpretation and field investigation, Robinson (2009b) and Robinson et al. (2015) suggested that this segment, as well as the southern part of the Muji-Tashkorgan segment to the north, was no longer active (fault trace covered by undisturbed loess, fluvial, and glacial deposits), since at least 24–200 ka (Owen et al., 2012). It has been proposed that initiation of the Longmu–Gozha Co fault between 3 and 9 Ma (Raterman et al., 2007), which approaches the Karakorum fault at Bangong Lake (Fig. 1), could have shut off movement along the Karakorum fault to the NW (Robinson, 2009b). Houlié and Phillips (2013) recently suggested that no matter where thrust seismic events occur along the Himalayan front, they may inhibit seismic activity along the northern portion of the fault, which may serve as an explanation for the lack of Quaternary offset evidence along the northwestern K2 segment, with most slip therefore taking place toward the southern segments of the fault. However, oblique plate convergence at depth along the slip-partitioned boundary between India and Tibet may indicate a more complex convergence accommodation mechanism than previously thought (Kundu et al., 2014).

From Bangong Lake, the southern half of the Karakorum fault can be divided into four segments from NW to SE: Bangong-Chaxikang, Gar Basin, Menshi-Kailas (Chevalier et al., 2012; Fig. 1B), and Kailas-Thakkhola. In Figure 3, we present detailed mapping of the main and secondary fault strands that offset Quaternary moraines, alluvial fans, and terraces along the SE end of the Bangong-Chaxikang segment and along the NW end of the Gar Basin segment.

Bangong-Chaxikang Segment

The Bangong-Chaxikang segment strikes N142°E and is ~265 km long (Fig. 1). Over a length of 150 km, this segment is very linear and single stranded and almost purely strike-slip (not transpressive nor transtensive), and it shows particularly clear long-term cumulative offsets of both the western part of Bangong Lake (41–101 km; Fig. 1A; Liu, 1993) and the dog-leg offset of the Indus River (120 km; Fig. 1A; Gaudemer et al., 1989). Southeast of 79.5°E (Fig. 1), the Karakorum fault splits into two main branches, where one branch (range-front fault) follows the base of the Ayilari Range and has a complex geometry, with multiple traces at places, as well as bends and steps. Prominent triangular facets (Fig. 3) attest to a significant normal component of slip in addition to a probable right-lateral strike-slip component. The other branch (mid-valley fault) lies within the Indus Valley and is very linear, as highlighted on various satellite images (Fig. 3) by vegetation patches fed by small springs. It is mainly strike-slip, with vertical motion due to local fault bends responsible for the formation of pressure ridges and pull-apart basins.

The range-front and mid-valley branches are roughly parallel along most of the fault zone. While they are ~5 km apart south of 32°35′N, they stand only 1.5 km from each other to the north (Fig. 3). Oblique splays, or transfer faults, roughly striking N-S, connect the two branches (Fig. 3). The northernmost splay zone corresponds to a releasing jog in the range front, a broadening of the Indus Valley, and the widening of the separation between the two main fault strands. Overall, the geometry of faulting between 32°26′N and 32°45′N is therefore indicative of transtensional slip partitioning, as observed for instance along the Damxung fault along the Nyainqentanghla Range in southern Tibet (Armijo et al., 1986), the Red River fault (e.g., Allen et al., 1984; Replumaz et al., 2001), or along the Kunlun fault (e.g., King et al., 2005; Klinger et al., 2005). In all these cases, partitioning results from oblique faulting at depth and appears to occur above a buried sediment-basement interface, within

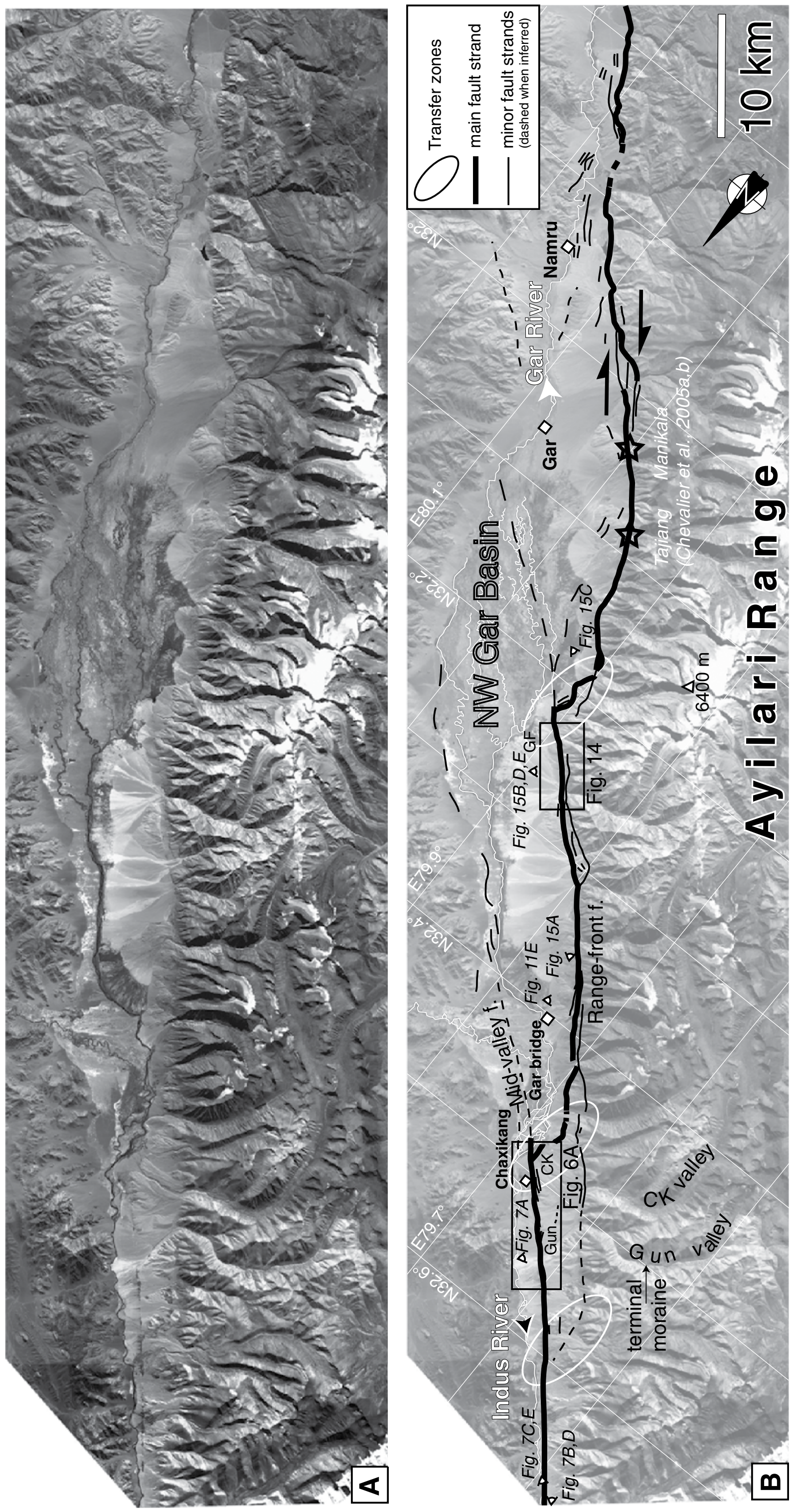

Figure 3. (A) *Landsat 7* satellite image of the Bangong-Chaxikang and Gar Basin segments of the Karakorum fault. (B) Active fault map of area shown in A. Right-lateral movement is distributed over several NW-SE, right-stepping subparallel strands (mostly the mid-valley and range-front faults), which connect through approximately N-S–trending transfer faults (white ellipses). Black boxes indicate location of study sites Gun, Chaxikang (CK), and Gar fan (GF; Figs. 6A and 14). Locations of field photos in Figures 7, 11, and 15 are shown. Stars show location of the largest till accumulation coming from the largest valleys at Manikala and Tajiang (Chevalier et al., 2005a, 2005b).

extensional half grabens. Here, the southward-increasing distance between the two partitioned faults likely results from the fact that the fault zone enters the greater Gar pull-apart basin to the south (Figs. 1 and 3).

Gar Basin Segment

The Gar Basin segment of the Karakorum fault (Fig. 1) strikes N140°–N170°E and is ~185 km long. Here, the main Karakorum fault is also divided into two main branches, the mid-valley fault, which continues into the swamps of the Gar Basin, where its trace becomes difficult to follow, and the range-front fault, which continues to follow the steep flank of the Ayilari Range (Fig. 3). The normal component of slip along the range-front fault appears to increase south of Chaxikang, as well as the average and summit elevations of the range. The average height of the triangular facets increases by at least 30% (up to ~1800 m; Fig. 3).

The Gar Basin has the geometry of an active dextral pull-apart basin (Armijo et al., 1986, 1989; Sanchez et al., 2010) and is composed of two rhomb-shaped subbasins ~15 km wide at most, over a total length of ~150 km. The two subbasins have approximately the same size and are bounded by high mountains. The topography across the NW basin shows clear asymmetry, with the Ayilari Range to the SW being ~400 m higher than the mountains to the NE, which implies that active normal throw is larger along the Ayilari range-front fault than on the opposite side (NE) of the NW Gar Basin. Note that fault strands are also present along the southern side of the Ayilari Range, the Quaternary activity of which is unclear (Fig. 1).

About one third of the way into the NW Gar Basin, at the foot of the Ayilari Range, a transfer step analogous to that observed south of Chaxikang is visible (Fig. 3). At this location, the range-front fault of the Bangong-Chaxikang segment continues straight into swamps fed by meandering channels of the Gar River (likely outlining a deep extensional sag in the center of the pull-apart), where its trace becomes difficult to follow. Sanchez et al. (2010) noted that the main fault strand is composed of fewer segments along the narrow, NW-striking, strike-slip zones, and of multiple segments along the wider, N-S–striking, dip-slip zones. They suggested that the dip-slip zones propagate basinward, leaving inactive segments behind and forming new segments as they move to the SE.

The Ayilari Range on the west side of the NW Gar Basin is still topped by a residual ice cap, which feeds many valley glaciers, most of them on the NE flank of the range (Fig. 3). As evidenced by deep glacial incisions extending much lower than the present termini, most of these glaciers have reached into the basin during the coldest epochs of the Pleistocene, abandoning impressive moraines that are still clearly visible today. The largest till accumulations come from the largest valleys at Manikala and Tajiang (stars in Fig. 3; Chevalier et al., 2005a, 2005b, 2011a).

METHODS

The active fault strands orthogonally cut most of the abandoned fluvioglacial terraces and moraines, which is an optimal setting to study faulting behavior. We used field observations, Chinese topographic maps (1:50,000 scale), and satellite images such as high-resolution *Quickbird*, *Ikonos*, *Landsat 7*, Advanced Spaceborne Thermal Emission and Reflection Radiometer (ASTER), *Satellite Pour l'Observation de la Terre* (SPOT), and *Corona* images to map and assess the relative importance of the active fault strands (Fig. 3). The relative ages of landforms were determined based on their imbrications and relative height above active riverbeds, and absolute ages were determined from ^{10}Be cosmogenic surface-exposure dating at targeted sites.

In total, 74 quartz-rich surface samples, mainly from cobbles (<25 cm in diameter), were collected at three sites: 28 from terraces at site Gun (7 km NW of Chaxikang), 32 from fan surfaces at site CK (Chaxikang), and 14 from a fan surface at site GF (Gar Fan, near Gar; Table 2). The ^{10}Be concentration in surface cobbles results mainly from nuclide accumulation due to exposure to cosmic rays at the sampling site. However, these concentrations may be biased toward higher values due to prior exposure (or inheritance; e.g., Van der Woerd et al., 1998; Schmidt et al., 2011; LeDortz et al., 2012) or toward lower values due to postdepositional erosion (e.g., Ritz et al., 2006; Vassallo et al., 2011; Benedetti and Van der Woerd, 2014). Pre-exposure can manifest itself in two ways. Either inheritance is random and expresses exposure of the cobble somewhere in the catchment, or it is evenly distributed within all the clast population and expresses a common exposure process, which in general corresponds to the transport time from the source to the sampling site. In the first scenario, single pre-exposed samples can easily be detected as outliers because they have much larger ^{10}Be concentrations than all the others (Van der Woerd et al., 1998). In the second scenario, average inheritance is usually determined by modeling the ^{10}Be concentration variation with depth (e.g., Anderson et al., 1996). Since depth profiles have not been collected at the sites studied here, it is thus possible that the ^{10}Be concentrations are biased toward higher values, particularly for sites Gun and Chaxikang, for which inheritance due to transport time and hillslope erosion can be significant (because the valleys are >10 km long at Gun and Chaxikang, compared to <3 km long at Gar fan).

Erosion can affect the deposits in several ways. First, the depositional surface may be affected by incision of rills developing in inherited lows (bar-and-swale morphology) from the depositional event. Second, erosion can affect clast surfaces due to chemical or physical alteration of the rock minerals, frost spallation, etc. Third, the fine-grained matrix of the inhomogeneous conglomeratic deposit may be evacuated due to erosion, leaving behind a cobble lag deposit. The first case is avoided by sampling the flattest, highest parts of the surfaces away from the incised rills. The second case affects the samples randomly (depending on sample lithology), can sometimes be detected during sampling, and usually leads to lower ^{10}Be concentration than other samples. The third case is usually addressed by modeling the depth dependence of ^{10}Be concentration in a depth profile and may be detected with a detailed stratigraphic description of the deposit. Again, depth profiles and stratigraphic logs have not been performed at our sites, and surface lowering due to matrix erosion may affect our results (by boulder toppling, yielding lower ^{10}Be concentration).

Although it has been proposed to model ^{10}Be concentration populations of moraines to distinguish among the various processes affecting these surfaces, models are usually underconstrained due to the low number of analyzed samples per surface (e.g., Hallet and Putkonen, 1994; Applegate et al., 2012). In order to be able to discuss the ^{10}Be concentration distributions, it is thus necessary to analyze a large set of samples per surface (Chevalier et al., 2011a). Here, we analyzed at least 10 clasts on each of five distinct surfaces and 5–6 samples on two of them. A population of 10 starts to be statistically significant and allows the shape of the distribution to be deciphered and distinction of potential outliers (e.g., Bierman, 1994; Van der Woerd et al., 1998; Matmon et al., 2006; Mériaux et al., 2012).

With all these drawbacks in mind, a few assumptions are thus necessary to analyze the ^{10}Be distributions, or here, the ^{10}Be modeled surface ages, for each surface. If a sample shows a significantly different age from the rest of the sample population (e.g., no overlapping error bars), it is considered an outlier and excluded from the data set. We applied a statistical criterion, Chauvenet's criterion, that numerically validates an eyeballed choice of outlier sorting (e.g., Mériaux et al., 2012), even though it does not prove any geomorphic process at play.

TABLE 2. ANALYTICAL RESULTS OF ^{10}Be GEOCHRONOLOGY AND SURFACE-EXPOSURE AGES ALONG THE BANGONG-CHAXIKANG AND GAR BASIN SEGMENTS

	Sample number	Lat (°N)	Long (°E)	Elev (m)	Thickness (cm)	Quartz/ granite	Quartz (g)	Be carrier (mg)	^{10}Be/^{9}Be ($\times10^{-15}$)	^{10}Be ($\times10^{6}$ atom/g)	Standard used*	Desilets ages (yr)#	Dunai ages (yr)#	Lifton ages (yr)#	LS indep ages (yr)#	**LS dep ages (yr)#**
Gun†																
T1 down	Gun-1	32.54	79.63	4262	5	g	24.97	0.442	629 ± 17	0.744 ± 0.021	KNSTD	11,673 ± 1420	12,134 ± 1470	11,344 ± 1167	11,802 ± 1082	**11,691 ± 1043**
	Gun-2	32.54	79.63	4262	5	g	12.05	0.4	461 ± 15	1.024 ± 0.034	LLNL3000	14,991 ± 1845	15,352 ± 1881	14,508 ± 1516	15,542 ± 1453	**15,267 ± 1390**
	Gun-3	32.54	79.63	4262	5	g	25.15	0.43	714 ± 22	0.816 ± 0.025	KNSTD	12,722 ± 1557	13,160 ± 1604	12,342 ± 1281	12,945 ± 1200	**12,820 ± 1157**
	Gun-5	32.54	79.63	4262	5	g	18.6	0.4	300 ± 13	0.432 ± 0.019	LLNL3000	6728 ± 852	7221 ± 911	6647 ± 723	6537 ± 643	**6502 ± 624**
	Gun-6	32.54	79.63	4262	5	g	9.41	0.422	211 ± 11	0.635 ± 0.034	LLNL3000	9697 ± 1260	10,155 ± 1314	9490 ± 1068	9627 ± 986	**9553 ± 957**
T2 down	Gun-7	32.54	79.63	4263	5	g	18.77	0.421	2432 ± 32	3.651 ± 0.048	KNSTD	46,039 ± 5526	44,919 ± 5366	43,652 ± 4389	58,522 ± 5218	**50,508 ± 4364**
	Gun-8	32.54	79.63	4263	5	g	18.7	0.403	777 ± 20	1.119 ± 0.03	LLNL3000	16,178 ± 1964	16,497 ± 1995	15,642 ± 1604	16,982 ± 1551	**16,565 ± 1471**
	Gun-9	32.54	79.63	4263	5	g	26.94	0.404	1417 ± 29	1.422 ± 0.029	KNSTD	20,773 ± 2499	20,944 ± 2509	19,973 ± 2021	22,592 ± 2028	**21,597 ± 1884**
	Gun-10	32.54	79.63	4263	5	g	24.97	0.43	975 ± 19	1.123 ± 0.022	KNSTD	16,863 ± 2025	17,160 ± 2052	16,292 ± 1645	17,822 ± 1595	**17,320 ± 1506**
	Gun-11	32.54	79.63	4263	5	g	25.04	0.428	663 ± 16	0.759 ± 0.018	KNSTD	11,895 ± 1436	12,346 ± 1484	11,547 ± 1175	12,038 ± 1089	**11,930 ± 1049**
	Gun-12	32.54	79.63	4263	5	g	21.3	0.403	707 ± 29	0.895 ± 0.037	KNSTD	13,831 ± 1734	14,238 ± 1778	13,397 ± 1437	14,189 ± 1370	**14,018 ± 1321**
T1 up	Gun-13	32.54	79.63	4265	5	g	14.62	0.42	1561 ± 44	2.996 ± 0.085	LLNL3000	37,610 ± 4606	37,018 ± 4514	36,089 ± 3737	45,725 ± 4229	**40,064 ± 3601**
	Gun-14	32.54	79.63	4265	5	g	24.09	0.403	1334 ± 26	1.493 ± 0.029	KNSTD	21,664 ± 2604	21,795 ± 2608	20,827 ± 2104	23,710 ± 2124	**22,565 ± 1964**
	Gun-15	32.54	79.63	4265	5	g	10.02	0.422	380 ± 13	1.072 ± 0.038	LLNL3000	15,564 ± 1925	15,907 ± 1960	15,062 ± 1585	16,239 ± 1532	**15,898 ± 1461**
	Gun-16	32.54	79.63	4265	5	g	24.95	0.429	3438 ± 44	3.955 ± 0.051	KNSTD	50,007 ± 6007	48,498 ± 5798	46,953 ± 4723	63,404 ± 5658	**55,404 ± 4791**
	Gun-17	32.54	79.63	4265	5	g	25.13	0.43	2215 ± 43	2.539 ± 0.049	KNSTD	34,173 ± 4119	33,675 ± 4041	32,668 ± 3309	40,471 ± 3639	**36,322 ± 3171**
	Gun-18	32.54	79.63	4265	5	g	24.98	0.429	555 ± 16	0.637 ± 0.018	KNSTD	10,103 ± 1231	10,557 ± 1281	9872 ± 1018	10,077 ± 927	**9994 ± 894**
T2 up	Gun-19	32.54	79.63	4267	5	g	25.25	0.468	915 ± 23	1.135 ± 0.029	KNSTD	16,985 ± 2060	17,278 ± 2087	16,406 ± 1680	17,975 ± 1638	**17,457 ± 1548**
	Gun-20	32.54	79.63	4267	5	g	24.95	0.429	724 ± 19	0.833 ± 0.022	KNSTD	12,940 ± 1571	13,370 ± 1616	12,547 ± 1287	13,188 ± 1204	**13,058 ± 1160**
	Gun-21	32.54	79.63	4267	5	g	20.24	0.428	1131 ± 22	1.599 ± 0.031	KNSTD	22,949 ± 2759	23,017 ± 2755	22,066 ± 2229	25,371 ± 2273	**23,983 ± 2087**
	Gun-22	32.54	79.63	4267	5	g	25.01	0.406	2764 ± 49	3.001 ± 0.053	KNSTD	38,955 ± 4691	38,304 ± 4591	37,340 ± 3775	47,886 ± 4297	**41,613 ± 3622**
	Gun-23	32.54	79.63	4267	5	g	25	0.509	7724 ± 73	10.512 ± 0.099	KNSTD	130,726 ± 15,980	125,767 ± 15,286	122,881 ± 12,549	172,975 ± 15,786	**145,776 ± 12,825**
	Gun-24	32.54	79.63	4267	5	g	20.83	0.402	1812 ± 54	2.342 ± 0.07	KNSTD	31,848 ± 3908	31,470 ± 3845	30,464 ± 3165	37,263 ± 3460	**33,863 ± 3058**
T3 down	Gun-25	32.54	79.63	4264	5	g	10.53	0.381	822 ± 27	1.99 ± 0.066	LLNL3000	26,727 ± 3297	26,622 ± 3271	25,617 ± 2683	30,264 ± 2838	**28,137 ± 2569**
	Gun-26	32.54	79.63	4264	5	g	10.26	0.406	1180 ± 22	3.126 ± 0.059	LLNL3000	38,877 ± 4690	38,230 ± 4591	37,269 ± 3777	47,751 ± 4298	**41,515 ± 3626**
	Gun-27	32.54	79.63	4264	5	g	24.93	0.415	4874 ± 81	5.431 ± 0.09	KNSTD	69,844 ± 8464	67,980 ± 8198	66,024 ± 6710	87,628 ± 7922	**76,540 ± 6703**
	Gun-28	32.54	79.63	4264	5	g	10.4	0.411	760 ± 29	2.01 ± 0.077	LLNL3000	26,960 ± 3368	26,844 ± 3340	25,842 ± 2754	30,571 ± 2929	**28,384 ± 2651**
	Gun-30	32.54	79.63	4264	5	g	25.29	0.407	2150 ± 51	2.316 ± 0.055	KNSTD	31,594 ± 3830	31,230 ± 3770	30,223 ± 3087	36,907 ± 3354	**33,575 ± 2965**

(*continued*)

TABLE 2. ANALYTICAL RESULTS OF ^{10}Be GEOCHRONOLOGY AND SURFACE-EXPOSURE AGES ALONG THE BANGONG-CHAXIKANG AND GAR BASIN SEGMENTS (*continued*)

	Sample number	Lat (°N)	Long (°E)	Elev (m)	Thickness (cm)	Quartz/granite	Quartz (g)	Be carrier (mg)	$^{10}Be/^{9}Be$ ($\times10^{-15}$)	^{10}Be ($\times10^{6}$ atom/g)	Standard used*	Desilets ages (yr)#	Dunai ages (yr)#	Lifton ages (yr)#	LS indep ages (yr)#	**LS dep ages (yr)#**
Chaxikang																
F3′	CK-1A	32.49445	79.68428	4224	5	g	10.49	0.427	977 ± 24	2.662 ± 0.066	LLNL3000	34,978 ± 4253	34,454 ± 4170	33,452 ± 3430	41,498 ± 3789	**37,050 ± 3287**
	CK-1B	32.49445	79.68428	4224	5	q	10.6	0.418	1497 ± 35	3.953 ± 0.093	LLNL3000	48,853 ± 5948	47,465 ± 5752	46,001 ± 4717	61,879 ± 5658	**53,846 ± 4778**
	CK-2A	32.49495	79.68443	4224	5	g	10.15	0.419	1184 ± 28	3.274 ± 0.077	LLNL3000	41,113 ± 4996	40,385 ± 4885	39,324 ± 4026	51,151 ± 4665	**44,068 ± 3901**
	CK-2B	32.49495	79.68443	4224	5	q	10.34	0.419	1199 ± 20	3.255 ± 0.056	LLNL3000	40,902 ± 4926	40,184 ± 4817	39,128 ± 3955	50,819 ± 4560	**43,810 ± 3812**
	CK-3A	32.49503	79.68438	4224	5	g	10.38	0.409	1170 ± 27	3.085 ± 0.073	LLNL3000	39,233 ± 4767	38,580 ± 4666	37,594 ± 3849	48,176 ± 4393	**41,813 ± 3702**
	CK-3B	32.49503	79.68438	4224	5	q	15	0.408	2337 ± 81	4.256 ± 0.149	LLNL3000	53,246 ± 6637	51,590 ± 6402	49,688 ± 5262	66,712 ± 6353	**58,614 ± 5429**
	CK-5	32.49547	79.68455	4224	5	g	10.67	0.424	1218 ± 25	3.24 ± 0.068	LLNL3000	40,778 ± 4935	40,065 ± 4827	39,012 ± 3971	50,622 ± 4584	**43,658 ± 3836**
	CK-6	32.49562	79.68485	4224	5	g	10.38	0.407	1129 ± 26	2.963 ± 0.07	LLNL3000	38,013 ± 4616	37,417 ± 4523	36,475 ± 3731	46,240 ± 4212	**40,422 ± 3575**
	CK-7A	32.49600	79.68467	4224	5	g	11.99	0.422	1417 ± 41	3.337 ± 0.098	LLNL3000	41,751 ± 5128	40,988 ± 5012	39,913 ± 4147	52,151 ± 4846	**44,858 ± 4050**
	CK-7B	32.49600	79.68467	4224	5	q	10.18	0.421	1322 ± 41	3.656 ± 0.114	LLNL3000	45,173 ± 5573	44,147 ± 5422	42,903 ± 4484	57,168 ± 5353	**49,197 ± 4477**
	CK-8A	32.49610	79.68487	4224	5	g	10.1	0.413	1326 ± 37	3.628 ± 0.102	LLNL3000	44,889 ± 5503	43,888 ± 5356	42,660 ± 4419	56,774 ± 5257	**48,831 ± 4392**
	CK-8B	32.49610	79.68487	4224	5	q	10.04	0.42	1121 ± 22	3.141 ± 0.063	LLNL3000	39,768 ± 4805	39,089 ± 4701	38,076 ± 3867	49,017 ± 4424	**42,437 ± 3717**
	CK-9	32.49683	79.68535	4224	5	g	20.07	0.423	2745 ± 53	3.866 ± 0.075	LLNL3000	47,749 ± 5776	46,465 ± 5594	45,089 ± 4582	60,541 ± 5473	**52,511 ± 4604**
	CK-25	32.49662	79.67762	4249	7	g	10.49	0.45	869 ± 20	2.491 ± 0.059	KNSTD	34,414 ± 4177	33,915 ± 4098	32,903 ± 3366	40,767 ± 3712	**36,526 ± 3230**
	CK-26	32.49743	79.67698	4249	7	g	8.07	0.44	328 ± 9	1.195 ± 0.033	KNSTD	18,226 ± 2220	18,484 ± 2242	17,571 ± 1810	19,466 ± 1787	**18,800 ± 1679**
	CK-27	32.49767	79.67672	4249	8	g	10.04	0.384	1180 ± 29	3.018 ± 0.075	KNSTD	40,282 ± 4906	39,580 ± 4798	38,548 ± 3959	49,924 ± 4571	**43,118 ± 3833**
F2	CK-12	32.49112	79.68070	4225	5	g	6.49	0.452	197 ± 5	0.919 ± 0.026	KNSTD	14,457 ± 1760	14,845 ± 1799	14,007 ± 1442	14,881 ± 1365	**14,658 ± 1308**
	CK1-13A	32.49083	79.68087	4225	5	g	10.26	0.41	568 ± 13	1.521 ± 0.036	LLNL3000	21,624 ± 2616	21,761 ± 2622	20,792 ± 2120	23,597 ± 2139	**22,464 ± 1980**
	CK1-13B	32.49083	79.68087	4225	5	q	10.13	0.486	851 ± 20	2.73 ± 0.064	LLNL3000	35,658 ± 4327	35,121 ± 4243	34,134 ± 3490	42,515 ± 3868	**37,761 ± 3337**
	CK1-14A	32.49142	79.68112	4225	5	g	10.24	0.423	470 ± 13	1.3 ± 0.036	LLNL3000	18,817 ± 2291	19,058 ± 2311	18,125 ± 1865	20,151 ± 1848	**19,417 ± 1733**
	CK-14B	32.49142	79.68112	4225	5	q	10.39	0.424	344 ± 9	0.939 ± 0.024	KNSTD	14,729 ± 1786	15,106 ± 1824	14,263 ± 1460	15,199 ± 1384	**14,953 ± 1325**
	CK-15	32.49057	79.68025	4225	5	g	8.56	0.448	476 ± 12	1.665 ± 0.042	KNSTD	24,292 ± 2949	24,301 ± 2938	23,332 ± 2391	27,047 ± 2467	**25,427 ± 2255**
	CK-16A	32.48988	79.68070	4225	5	g	7.839	0.402	207 ± 6	0.71 ± 0.022	KNSTD	11,414 ± 1397	11,878 ± 1448	11,108 ± 1152	11,498 ± 1065	**11,385 ± 1027**
	CK-16B	32.48988	79.68070	4225	7	q	10.089	0.408	129 ± 4	0.35 ± 0.011	KNSTD	5915 ± 723	6280 ± 765	5858 ± 607	5744 ± 532	**5783 ± 521**
	CK-17	32.48978	79.68087	4225	7	g	6.639	0.443	275 ± 7	1.232 ± 0.033	KNSTD	18,944 ± 2302	19,180 ± 2321	18,245 ± 1873	20,305 ± 1856	**19,555 ± 1739**

(*continued*)

TABLE 2. ANALYTICAL RESULTS OF ^{10}Be GEOCHRONOLOGY AND SURFACE-EXPOSURE AGES ALONG THE BANGONG-CHAXIKANG AND GAR BASIN SEGMENTS (*continued*)

	Sample number	Lat (°N)	Long (°E)	Elev (m)	Thickness (cm)	Quartz/ granite	Quartz (g)	Be carrier (mg)	^{10}Be/^{9}Be ($\times10^{-15}$)	^{10}Be ($\times10^{6}$ atom/g)	Standard used*	Desilets ages (yr)#	Dunai ages (yr)#	Lifton ages (yr)#	LS indep ages (yr)#	**LS dep ages (yr)#**
Chaxikang (*continued*)																
	CK-18	32.49018	79.68047	4225	5	g	10.129	0.42	286 ± 7	0.795 ± 0.021	KNSTD	12,680 ± 1540	13,120 ± 1587	12,304 ± 1262	12,869 ± 1176	**12,744 ± 1133**
F3	CK-19§	32.49420	79.67830	4244	10	g	10.179	3.39	78 ± 3	0.738 ± 0.08	KNSTD	25,907 ± 3302	25,844 ± 3281	24,828 ± 2719	29,146 ± 2888	**27,215 ± 2633**
	CK-20	32.49432	79.67765	4244	5	g	10.109	0.438	290 ± 13	0.841 ± 0.039	KNSTD	13,219 ± 1683	13,646 ± 1731	12,816 ± 1403	13,483 ± 1335	**13,339 ± 1291**
	CK-21	32.49425	79.67740	4244	5	g	11.23	0.455	532 ± 25	1.441 ± 0.068	KNSTD	21,259 ± 2715	21,410 ± 2724	20,437 ± 2245	23,166 ± 2304	**22,095 ± 2147**
	CK-22	32.49448	79.67728	4244	6	q	10.25	0.404	635 ± 23	1.671 ± 0.062	KNSTD	24,297 ± 3026	24,305 ± 3014	23,335 ± 2477	27,087 ± 2582	**25,463 ± 2366**
	CK-23	32.49390	79.67825	4244	4	q	10.11	0.446	813 ± 21	2.397 ± 0.064	KNSTD	32,666 ± 3984	32,250 ± 3916	31,240 ± 3217	38,323 ± 3519	**34,695 ± 3097**
	CK-24	32.49338	79.67817	4244	4	q	10.81	0.439	580 ± 13	1.575 ± 0.037	KNSTD	22,772 ± 2755	22,853 ± 2753	21,897 ± 2232	25,100 ± 2275	**23,747 ± 2092**
CK M3	CK-40	32.48522	79.66877	4320	7	q	10.6278	0.448	2902 ± 55	8.174 ± 0.157	KNSTD	101,599 ± 12,452	98,764 ± 12,043	96,516 ± 9930	130,637 ± 12,011	**111,152 ± 9 2**
	CK-43	32.48427	79.66142	4390	2	q	10.197	0.439	2802 ± 64	8.065 ± 0.186	KNSTD	937,27 ± 11,531	90,947 ± 11,132	88,406 ± 9152	119,227 ± 11,044	**102,506 ± 9193**
	CK-44	32.48428	79.66092	4400	4	q	8.3398	0.444	3171 ± 67	11.297 ± 0.238	KNSTD	128,012 ± 15,836	123,115 ± 15,145	120,441 ± 12,513	171,108 ± 15,969	**143, 75 ± 12,962**
	CK-45	32.48442	79.65992	4410	9	q	10.0955	0.429	3234 ± 63	9.201 ± 0.18	KNSTD	109,390 ± 13,440	105,938 ± 12,947	103,533 ± 10,679	143,433 ± 13,241	**120,759 ± 10,772**
	CK-46	32.48433	79.65808	4425	7	q	10.1263	0.44	4118 ± 49	11.972 ± 0.144	KNSTD	137,171 ± 16,829	131,575 ± 16,048	128,639 ± 13,193	184,139 ± 16,914	**155,506 ± 13,76**
	CK-47	32.48433	79.65697	4435	8	q	10.3915	0.447	2564 ± 37	7.373 ± 0.107	KNSTD	87,926 ± 10,680	85,067 ± 10,279	82,598 ± 8402	111,758 ± 10,124	**97,020 ± 504**
	CK-48	32.48422	79.65548	4440	6	q	6.4497	0.455	2067 ± 58	9.765 ± 0.277	KNSTD	111,196 ± 13,868	107,613 ± 13,351	105,196 ± 11,078	146,536 ± 13,892	**123,134 ± 11,294**
CK M2 inner	CK-50§	32.48998	79.64917	4440	10	q	10.0812	2.06	377 ± 10	5.138 ± 0.139	KNSTD	75,161 ± 9883	72,829 ± 9510	70,440 ± 7784	97,187 ± 9851	**4,1 10 ± 174**
	CK-52	32.48985	79.64717	4460	7	q	10.1354	0.464	2052 ± 36	6.286 ± 0.11	KNSTD	72,978 ± 8861	70,720 ± 8544	68,646 ± 6992	92,924 ± 8430	**1,196 ± 7135**
	CK-53	32.48995	79.64593	4470	7	q	10.9275	0.435	1746 ± 34	4.655 ± 0.092	KNSTD	53,339 ± 6464	51,538 ± 6216	49,681 ± 5058	68,068 ± 6170	**59, 1 ± 525**
CK M2 outer	CK-54	32.48655	79.64740	4490	7	q	10.0825	0.416	1390 ± 33	3.841 ± 0.091	KNSTD	43,204 ± 5254	42,260 ± 5116	41,153 ± 4216	55,457 ± 5065	**47,59 ± 4219**
	CK-55	32.48665	79.64790	4485	6	q	9.9785	0.448	901 ± 17	2.706 ± 0.054	KNSTD	32,467 ± 3914	32,020 ± 3843	31,018 ± 3144	38,692 ± 3482	**34,977 ± 3056**
	CK-56	32.48668	79.64825	4480	5	q	10.4769	0.449	1168 ± 28	3.352 ± 0.08	KNSTD	38,407 ± 4666	37,736 ± 4564	36,808 ± 3769	47,755 ± 4355	**41,4 1 ± 3673**
	CK-57	32.48680	79.64872	4475	5	q	10.3005	0.44	1825 ± 37	5.209 ± 0.106	KNSTD	59,399 ± 7215	57,733 ± 6979	55,513 ± 5666	74,896 ± 6810	**65,560 ± 57 0**
	CK-58	32.48687	79.64925	4470	8	q	10.276	0.432	588 ± 16	1.655 ± 0.045	KNSTD	21,753 ± 2647	21,869 ± 2650	20,890 ± 2148	24,132 ± 2211	**22,922 ± 2043**
	CK-60	32.48772	79.65262	4440	6	q	6.5508	0.436	576 ± 21	2.567 ± 0.094	KNSTD	31,690 ± 3946	31,295 ± 3881	30,286 ± 3211	37,491 ± 3571	**34,032 ± 315**
	CK-61	32.48867	79.65462	4425	6	q	10.3351	0.421	1914 ± 51	5.214 ± 0.14	KNSTD	61,638 ± 7571	60,100 ± 7347	57,957 ± 6008	77,480 ± 7184	**67,6 6 ± 6091**
	CK-63	32.49023	79.65715	4390	7	q	10.2733	0.441	1641 ± 64	4.709 ± 0.183	KNSTD	57,034 ± 7186	55,283 ± 6935	53,134 ± 5709	71,654 ± 6948	**62,911 ± 5937**

(*continued*)

TABLE 2. ANALYTICAL RESULTS OF ^{10}Be GEOCHRONOLOGY AND SURFACE-EXPOSURE AGES ALONG THE BANGONG-CHAXIKANG AND GAR BASIN SEGMENTS (*continued*)

Sample number	Lat (°N)	Long (°E)	Elev (m)	Thickness (cm)	Quartz/granite	Quartz (g)	Be carrier (mg)	^{10}Be/^{9}Be ($\times10^{-15}$)	^{10}Be ($\times10^{6}$ atom/g)	Standard used*	Desilets ages (yr)#	Dunai ages (yr)#	Lifton ages (yr)#	LS indep ages (yr)#	LS dep ages (yr)#
Gar fan (GF)															
GF-1	32.25053	79.53751	4365	4	q	10.44	0.432	252 ± 6	0.699 ± 0.019	KNSTD	10,465 ± 1270	10,921 ± 1320	10,207 ± 1046	10,535 ± 962	**10,433 ± 927**
GF-2	32.25167	79.53753	4365	7	q	10.49	0.439	646 ± 21	1.807 ± 0.058	KNSTD	24,844 ± 3058	24,830 ± 3043	23,814 ± 2486	28,006 ± 2616	**26,221 ± 2384**
GF-3	32.25155	79.53753	4365	10	q	10.33	0.433	320 ± 8	0.898 ± 0.025	KNSTD	13,780 ± 1676	14,195 ± 1719	13,338 ± 1371	14,209 ± 1302	**14,026 ± 1250**
GF-4	32.25165	79.53753	4393	7	q	10.11	0.433	240 ± 6	0.689 ± 0.017	KNSTD	10,410 ± 1259	10,867 ± 1308	10,154 ± 1036	10,491 ± 951	**10,390 ± 916**
GF-5	32.25150	79.53753	4393	6	q	10.09	0.443	980 ± 22	2.877 ± 0.067	KNSTD	36,147 ± 4384	35,574 ± 4296	34,586 ± 3534	43,798 ± 3983	**38,600 ± 3408**
GF-6	32.25182	79.53753	4393	6	q	10.04	0.429	559 ± 13	1.599 ± 0.038	KNSTD	21,926 ± 2652	22,051 ± 2656	21,055 ± 2146	24,227 ± 2195	**22,979 ± 2024**
GF-7	32.25182	79.53753	4393	4	q	10.07	0.456	377 ± 9	1.142 ± 0.027	KNSTD	16,086 ± 1944	16,413 ± 1975	15,539 ± 1583	16,992 ± 1539	**16,560 ± 1458**
GF-8	32.25218	79.53754	4365	3	q	10.08	0.449	469 ± 11	1.395 ± 0.033	KNSTD	19,292 ± 2332	19,521 ± 2350	18,554 ± 1890	20,902 ± 1893	**20,073 ± 1767**
GF-9	32.25218	79.53754	4365	10	g	10.27	0.444	542 ± 12	1.566 ± 0.037	KNSTD	22,463 ± 2717	22,562 ± 2717	21,576 ± 2199	24,885 ± 2255	**23,538 ± 2073**
GF-10	32.25230	79.53754	4365	13	g	10.04	0.442	252 ± 6	0.741 ± 0.018	KNSTD	11,834 ± 1431	12,292 ± 1480	11,482 ± 1171	12,039 ± 1092	**11,922 ± 1051**
GF-11	32.25218	79.53754	4365	11	q	10.01	0.441	244 ± 6	0.721 ± 0.018	KNSTD	11,334 ± 1370	11,798 ± 1420	11,023 ± 1124	11,499 ± 1043	**11,378 ± 1004**
GF-12	32.25223	79.53754	4348	7	g	10.66	0.507	961 ± 24	3.055 ± 0.077	KNSTD	38,841 ± 4730	38,189 ± 4630	37,214 ± 3823	48,026 ± 4398	**41,617 ± 3701**
GF-13	32.25202	79.53753	4348	9	g	10.02	0.451	119 ± 3	0.36 ± 0.01	KNSTD	5837 ± 709	6168 ± 746	5781 ± 594	5693 ± 521	**5734 ± 510**
GF-14	32.25185	79.53753	4348	7	g	10	0.443	212 ± 5	0.628 ± 0.016	KNSTD	9801 ± 1185	10,261 ± 1236	9584 ± 978	9787 ± 888	**9702 ± 857**

Note: The samples were processed at the Lawrence Livermore National Laboratory (LLNL), and the ^{10}Be/^{9}Be ratios were measured at the Center for Accelerator Mass Spectrometry (CAMS) at LLNL. All samples are cobbles (<25 cm in diameter). Ages were calculated with the CRONUS 2.2 (with constants 2.2.1) calculator. LS dep (indep)—Lal (1991)/Stone (2000) time-dependent (independent) production rate model. Shielding factor is 0.99; sample density is 2.7 g/cm^3 for granite and 2.65 g/cm^3 for quartzite.

*^{10}Be isotope ratios for KNSTD = 3.11×10^{-12} and for LLNL3000 = 3×10^{-12}.

†Global positioning system (GPS) position is centered on the site due to access restriction, which prevented us from recording individual positions.

§Corrected for excess ^{9}Be (concentration measured in Inductively coupled plasma rather than weighted).

#External uncertainties (analytical and production rate) are reported at the 1σ confidence level. Desilets and Zreda (2003), Desilets et al. (2006), Dunai (2000, 2001), Lifton et al. (2005).

Because we analyzed inset surfaces, we also checked for stratigraphic consistency of the age distributions across the terrace sets. For instance, inheritance may be assumed to be similar across a set of terraces if due to transport in the catchment. Erosion, however, may affect terraces of various ages differently (for example, a more pronounced bar-and-swale morphology may be observed on older surfaces), although processes affecting young terraces must also affect the older ones (for example, chemical or physical alteration).

We will assume negligible erosion of the targeted alluvial surfaces based on several observations. First, the region is located in a dry region of Tibet with limited precipitation, mostly in the form of occasional snow storms, so that postdepositional modification of the surfaces is minimized. Second, erosion of the clasts may be assessed. We tested for variable rock erosion by measuring the ^{10}Be concentration in cobbles and boulders of various resistance, such as granite and quartz vein blocks, sampled as pairs located less than 1 m from each other. This experiment was performed for eight sample pairs at site Chaxikang, located centrally between Gun and Gar fan, and showed no systematic difference in ^{10}Be concentration (Fig. 4; Table 2; Chevalier et al., 2011a). This simple experiment indicates that clast alteration (chemical and physical weathering) may not be significant (e.g., Briner, 2009). Bedrock surfaces have been found to erode rather slowly across Tibet (e.g., Lal et al., 2003; Strobl et al., 2012) with rates of 3–15 m/Ma. Applying such rates to the cobbles and boulders sampled at our sites would decrease a 10, 20, 40, and 50 ka model age by 4%, 7%, 16%, and 26%, respectively (Table 2; e.g., Ryerson et al., 2006). Without other means of constraining erosion, we consider the relatively well-preserved surfaces as an indication of negligible surface modification.

Snow or loess cover and possible associated shielding are also likely negligible. Snow cover is in general limited due to dry conditions, especially in the continental, arid western part of the plateau. There is no seasonal snow cover, and snowfall is usually short-lived and less than a few tens of centimeters thick. Although climatic conditions have certainly changed through the last glacial cycle, correction for snow is most likely not required and negligible. For comparison, the shielding effect of a 70 cm snow cover during the last 10 k.y. in Alaska (where snowfall is much more frequent and abundant than on the Tibetan Plateau) has been shown to affect the ages by only 10% (Mériaux et al., 2009). In addition, Strobl et al. (2012) have shown that a decrease in production rate of only 4.5% occurs if the annual precipitation from southern Tibet

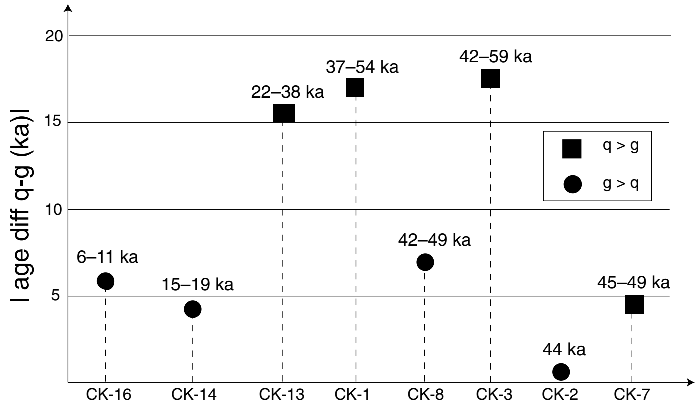

Figure 4. Absolute age value difference between quartzite (q) and granitic (g) sample pairs from the Chaxikang fan, and range of ages for each pair. Despite differences, no particular trend can be determined over the time scale considered (6–59 ka; Table 2). See text for details.

would fall as snow and remain on the ground for 6 months per year.

While loess may come and go as a function of changing climate, there is no hint at our sites that the targeted surfaces were mantled by a significant loess cover in the past. In general, when this is the case, loess remnants are significant and cannot be missed (e.g., Van der Woerd et al., 2002; Mériaux et al., 2005; Perrineau et al., 2011).

To summarize, we first used a basic visual rule to reject outliers. Samples with overlapping error bars were considered to belong to a cluster, and samples with no overlapping error bars were considered outliers (e.g., Van der Woerd et al., 1998). The most commonly used statistical criterion of Chauvenet (Bevington and Robinson, 1992; Taylor, 1997; Dunai, 2010) generally yields the same result (Mériaux et al., 2012). Chauvenet's criterion looks for a probability band, centered on the mean of a normal distribution (even though our ages are not normally distributed), that should reasonably contain all samples, therefore allowing removal of any sample lying outside this probability band (the rejected sample is an outlier). One may apply the criterion several times in a row (data returning values <0.5 are considered outliers, and there must be as many points closer to the mean as there are further away, i.e., each value has a 50% chance of survival), with the limitation that there must be a statistically sound number of samples left in the data set. Indeed, the population size is important. A large population is less likely to be affected by a single outlier, regardless of its value, while a small population is more sensitive to outlier selection. In cases of bi- or multimodal distributions or continuously scattered distributions, the criterion reaches its limits. All data points may be sequentially rejected, and one may stop after three iterations. Here, we carefully applied this statistical test for each data ensemble (Table 3), which allowed us to discard outliers and thus estimate the age of each surface. Note that the criterion is efficient at Gun, due to the presence of plateau ages with upper and lower tails (e.g., Matmon et al., 2006), but less efficient at Chaxikang or Gar fan, where ages are more regularly distributed or show a bimodal distribution, respectively (see following).

Throughout the text, we therefore refer to model ages calculated with no erosion and no inheritance, using the time-dependent Lal (1991)/Stone (2000) production rate model. Ages calculated with other available production rate models (Dunai, 2000, 2001; Desilets and Zreda, 2003; Lifton et al., 2005; Desilets et al., 2006) can be found in Table 2. Uncertainties for individual model ages refer to external uncertainties (i.e., analytical and production rate; Balco et al., 2008) and are reported at the 1σ confidence level (Table 2). In the text, we report median ages before and after outlier selection (for each surface) and calculated slip-rates using the method of Zechar and Frankel (2009), with uncertainties at the 1σ confidence interval about the median.

RESULTS

Gun Site

Geomorphology

The Gun fan complex is located at 32°33′N, 79°37′E, ~7 km NW of the Chaxikang fort, at an elevation of ~4280 m, between the Indus River and the north Ayilari Range. This fan complex was emplaced at the outlet of the Gun valley, a winding fluvioglacial valley, which extends over 18 km from the top of the range (~6000 m) to the range front (4450 m) (Fig. 3). The Gun and Chaxikang valleys are close to one another and have similar lengths and shapes, although the latter is wider and flatter (Fig. 3). The Gun valley has been incised by a shorter glacier than the one that carved the Chaxikang valley. The glacier that once occupied the Gun valley appears to have reached only about two thirds of the way between the top and the outlet of the valley, evidenced by the transition from a U- to a V-shaped valley and terminal moraines found ~6–7 km upstream from the range front (Fig. 3). Hence, the Gun glacier appears to have never crossed the range-front fault to deposit moraines in the Indus River floodplain, in sharp contrast with what is observed at Chaxikang (see following). Note also that the Chaxikang and Gun valleys do not merge upstream, where an ice-cap used to cover the range during glacial maxima (e.g., Chevalier et al., 2005a). The upstream catchment of the Gun glacier was thus likely smaller than that of the Chaxikang glacier.

While incising into the Ayilari Range bedrock and the moraines, the Gun River has emplaced two large imbricated fan complexes in the Indus River floodplain (Figs. 5 and 6). The oldest, dark-colored fan complex is located east of the Gun River, while the distal part of the youngest fan complex, lighter-colored, spreads out to the west of the Gun River. The river has incised into the fan complex deposits, forming a series of terraces with distinct hues on the images and in the field (Figs. 5–8). About halfway on the oldest fan, part of the present-day Gun River has been deviated eastward for irrigation purposes along water ducts that cross the natural channels (Fig. 5). Farther downstream, all the fans and terraces are crosscut by the active mid-valley branch of the Karakorum fault (Figs. 5–9). There are traces of large earthquakes along this mid-valley branch of the fault, most commonly visible as meter-size mole tracks, as well as very large (20 m high at places) cumulative pressure ridges (Figs. 7B–7E).

Northwest of the Gun site, the Karakorum fault displays mostly pure strike-slip movement across the fans, with springs outlining the fault trace (highlighted in black by darker vegetation on the satellite images; Fig. 5). Near the present-day Gun River, the fault sharply cuts and right-laterally offsets a set of three terraces (T1–T3). There, the main scarp along the mid-valley fault faces NE in the NW part of the fan complex, but it faces SW in its SE part. The fact that this shift occurs about midway across the fan (Figs. 6 and 8) suggests apparent vertical offset resulting from predominant strike-slip motion across a conical fan-shaped surface. This shift also coincides with a slight bend to the SE in the trace

TABLE 3. OUTLIERS REJECTION USING CHAUVENET'S CRITERION

	Chauvenet 1	Chauvenet 2	Chauvenet 3
Gun T1			
n =	11	10	8
Mean =	21,462	18,068	13,036
St dev =	15,674	11,496	4927
Mean square of weighted deviation (MSWD) =	31.48	24.44	14.53
Samples rejected	**Gun 16 (55,404 yr)**	**Gun 13 (40,064 yr)** **Gun 17 (36,322 yr)**	**Gun 14 (22,565 yr)** **Gun 5 (6502 yr)**
Chauvenet value	0.02	0.07 and 0.25	0.05 and 0.49
Gun T2			
n =	12	11	9
Mean =	33,974	24,200	19,187
St dev =	37,245	12,934	7079
MSWD =	71.28	30.3	21.57
Samples rejected	**Gun 23 (145,776 yr)**	**Gun 7 (50,508 yr)** **Gun 22 (41,613 yr)**	**Gun 24 (33,863 yr)**
Chauvenet value	0	0.04 and 0.44	0.02
Gun T3			
n =	5	4	3
Mean =	41,630	32,903	30,032
St dev =	20,255	6265	3071
MSWD =	49.19	33.66	30.19
Samples rejected	**Gun 27 (76,540 yr)**	Gun 26 (41,515 yr)	Gun 30 (33,575 yr)
Chauvenet value	0.07	0.21	0.31
Chaxikang (CK) F2			
n =	10	9	7
Mean =	18,415	16,265	16,454
St dev =	8878	6057	4071
MSWD =	22.23	18.25	17.3
Samples rejected	**CK 13b (37,761 yr)**	**CK 15 (25,427 yr)** **CK 16b (5783 yr)**	**CK 13a (22,464 yr)**
Chauvenet value	0.03	0.42 and 0.19	0.44
CK F3			
n =	6	5	4
Mean =	24,426	26,643	24,630
St dev =	6973	4889	2205
MSWD =	25.95	27.28	24.8
Samples rejected	**CK 20 (13,339 yr)**	**CK 23 (34695 yr)**	–
Chauvenet value	0.39	0.25	
CK F3′			
n =	16	14	11
Mean =	43,722	44,439	43,569
St dev =	8918	5136	3440
MSWD =	45.48	45	43.84
Samples rejected	**CK 3b (58,614 yr)** **CK 26 (18,800 yr)**	**CK 1b (53,846 yr)** **CK 9 (52,511 yr)** **CK 25 (36,526 yr)**	CK 1a (37,050 yr) CK 7b (49,197 yr) CK 8a (48,831 yr)
Chauvenet value	0.29 and 0	0.13 and 0.37 and 0.41	0.08 and 0.23 and 0.34
Gar fan (GF)			
n =	14	12	10
Mean =	18,798	15,246	15,100
St dev =	10,862	6533	5358
MSWD =	24.64	17.84	16.8
Samples rejected	**GF 5 (38,600 yr)** **GF 12 (41,617 yr)**	GF 2 (26,221 yr) GF 13 (5734 yr)	GF 6 (22,979 yr) GF 9 (23,538 yr)
Chauvenet value	0.14 and 0.04	0.21 and 0.47	0.38 and 0.26

of the fault (Fig. 8). The mid-valley fault trace is simple and linear across the NW part of the fan complexes, but in contrast, there are several minor extensional fault splays south of the fault across the SE part of the older complex (Figs. 6B and 8).

The different surfaces within the fan complexes have distinctive characteristics, all showing complex channel networks. As determined in the field and on satellite images, T1 is smoother with shallow braided gullies, mostly parallel to those in the Gun riverbed (Figs. 7A and 9A), and the surface rocks are mostly granite cobbles (<25 cm). The T1/T0 riser is extremely sharp and well preserved upstream from the fault but not downstream (Figs. 6B, 8A, and 9A). Two facts, (1) that the T1/T0 upstream riser stops abruptly at the fault (due to apparent vertical motion with the southwestern side up) and (2) that no measurable right-lateral offset is visible, imply that T1, NE of the fault, may be younger next to the stream than away from it. We sampled accordingly, i.e., away from the T1/T0 riser, but also away from the T2/T1 riser to avoid contamination from riser degradation (Figs. 6 and 8).

T2 is broader and incised by deeper channels than that on T1, but it is nevertheless composed of granite cobbles of similar sizes. Although not free-faced, the T2/T1 riser is very sharp downstream as well as upstream from the mid-valley fault, and it is clearly offset. Pull-apart sags are visible along the fault (highlighted by snow in Figs. 6, 8, and 9). The fault scarp on T2 is ~4 m high, facing NE (Fig. 7A). Most channels on T2 are ~N-S trending and tend to diverge, as is usual on distal parts of a fan, and meet the T2/T1 riser at rather high angle (up to 50°).

T3 is the darkest surface on the satellite images and in the field, with boulders up to 1 m large (Figs. 6–8), forming levee crests separating channels that are deeper than those on T2 and T1. The T3/T2 limit is quite different from the linear, sharply cut risers that separate the surfaces of T2, T1, and T0 upstream. While T3 and T2 on either side of this riser are quite different, the limit itself has a complex, sawtoothed shape with indentations and protruding lobes (Figs. 6 and 8), due to the roughness and deep incisions on T3, which over time, carved the T3/T2 limit more than the recent T2/T1 riser. In fact, most of the indentations are related to the oblique channels that intersect the T3/T2 limit. Even more than on T2, the channel geometry on T3 is typical of the distal part of a fan. The NE-facing fault scarp on T3 is up to ~6 m high closer to T2. The average slope of T3 fan is ~3°, as calculated from topographic map contours.

The different characteristics of the three main surfaces probably in part reflect different modes of emplacement. It appears that the fan complex apexes have migrated downstream along the glacial outwash (Figs. 3 and 5). Hence, the outwash regime near the fault has evolved from broad, distal, and depositional (fan mode), to more restricted channel aggradation and incision, which probably accounts for the different aspects of the terrace risers and edges. In addition, the emplacement of T3 seems to reflect a higher-energy depositional environment when compared to T2, and especially to T1 and T0. Indeed, T3 has larger, more angular debris, and the shape of the T3/T2 limit is sawtoothed rather than linear. It may also indicate that T2 was emplaced as a fill deposit, along the margin of the T3 fan surface.

Offsets

Several distinct right-lateral offsets can be identified and measured along the mid-valley fault across the Gun fan complex (Figs. 6, 8, and 9). Eastward from the Gun River, the height of the north-facing scarp increases from ~1 m on T1, to ~4 m on T2, to ~6 m on T3.

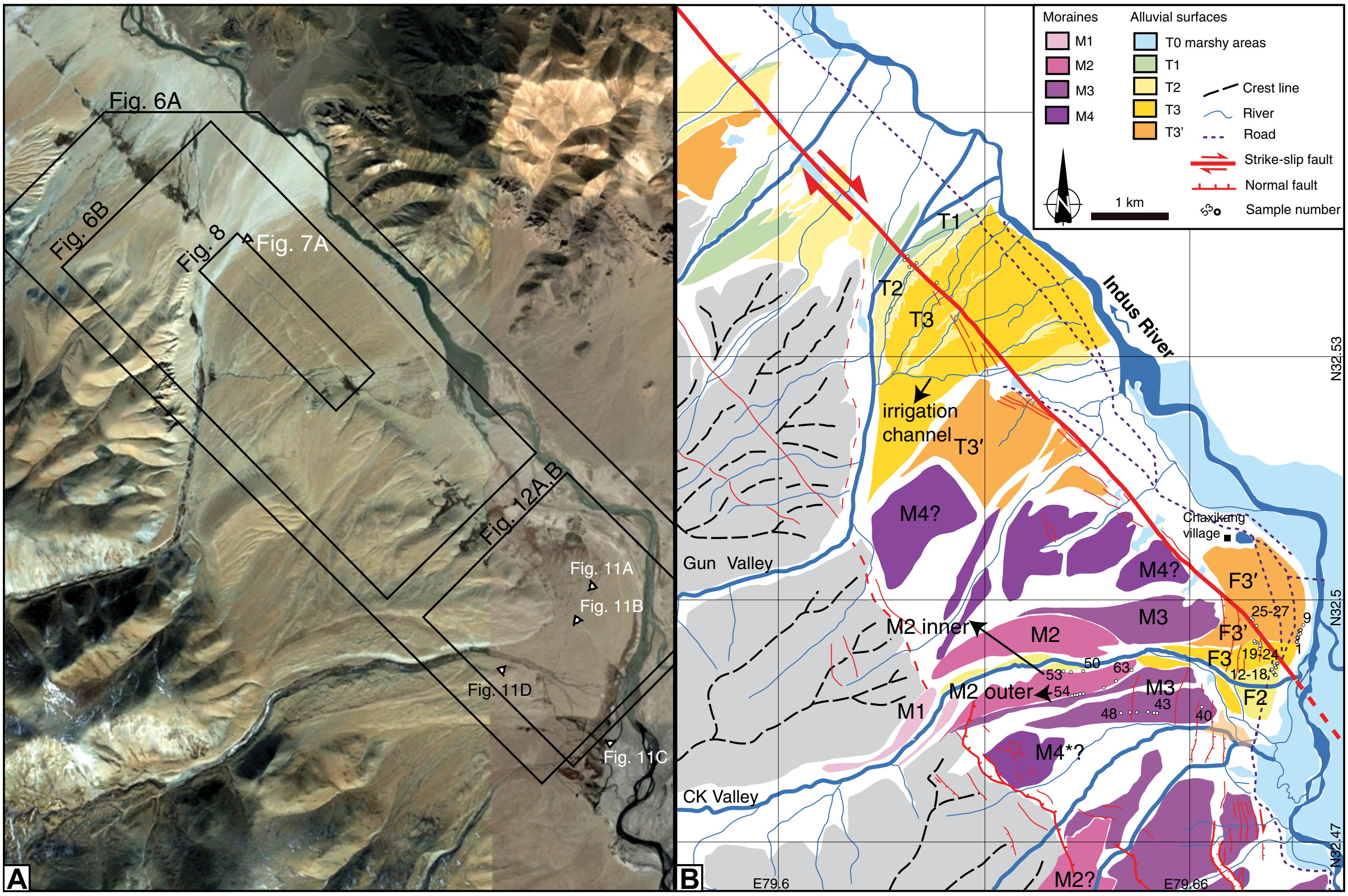

Figure 5. (A) GoogleEarth image of study area at sites Gun and Chaxikang (CK). (B) Geomorphological interpretation of A. Locations of field photos in Figures 7 and 11 are shown.

We interpret vertical offsets to be primarily due to displacement of conical fan-shaped surfaces, as discussed previously. We measured the cumulative offsets SE of the outwash by projecting the riser directions to the fault and realigning them across the fault (e.g., Gaudemer et al., 1995) on the 1-m-resolution *Ikonos* image (Fig. 9B). The best fits of the geomorphic markers (terrace risers, fan edges, and river channels) across the fault after retrodeformation of satellite images are as follow (Figs. 8 and 9): A 38 ± 5 m offset (Figs. 9C and 9D) is measured for the T2/T1 riser, for which a small uncertainty is assigned due to the very linear and sharp riser, which makes realignment across the fault straightforward. Note that this offset value may be a minimum due to the possible refreshment of the upstream T2/T1 riser (e.g., Cowgill, 2007). However, a similar offset of one large channel incised into T2 is also measured, with a slightly larger uncertainty due to the fact that the channel is not linear but meanders (Figs. 9C and 9D). After projecting the channel's main direction on each side of the fault, we obtain an offset of 38 ± 10 m (Figs. 9B and 9D). In addition, several other gullies on T2 are realigned when the image is retrodeformed by that amount (Figs. 9B and 9D). This channel offset value is identical to that of the T2/T1 riser and therefore is likely coeval with it, indicating that the T2/T1 riser began accumulating offset following abandonment of T2. The 38 (+10/–5) m offset value constitutes the clearest offset measurement at this site. The T3/T2 limit offset is more difficult to assess because of its irregular shape. It ranges from 90 to 150 m depending on the reconstruction (average 120 ± 30 m; Figs. 9E–9I). Last, the offsets between the upstream and downstream branches of the irrigation channel, probably located in older abandoned channels incising T3 to the SE, range from 150 to 220 m (Fig. 8B). These offsets overlap with the higher range of the T3/T2 offset, probably reflecting displacement of the oldest part of the fan surface T3, but they are not well constrained and will therefore not be used to constrain slip-rates. Although the range-front fault can be traced for tens of kilometers to the SW (Figs. 3 and 5), no clear offset is visible on the images, and we could not reach it in the field due to access restriction.

Surface Ages

Twenty-eight granite cobbles were collected on the three surfaces (Table 2; Fig. 8): 11 from T1 (five downstream from the fault: Gun 1–6, and six upstream: Gun 13–18), 12 from T2 (six downstream: Gun 7–12, and six upstream: Gun 19–24; closer to the T2/T1 riser to avoid possible contamination from T3), and five downstream from the fault on T3 (Gun 25–30).

The shape of the age distributions on each terrace (Fig. 10) shows a similar pattern of a relatively tight cluster of young ages with a significant upper tail (~30% of the ages), which is best explained by random inheritance. Despite the large age range (Fig. 10; Table 2), young clusters can nevertheless be defined after applying Chauvenet's criterion three times (Table 3). T3 ages range from 28 to 77 ka, with the oldest

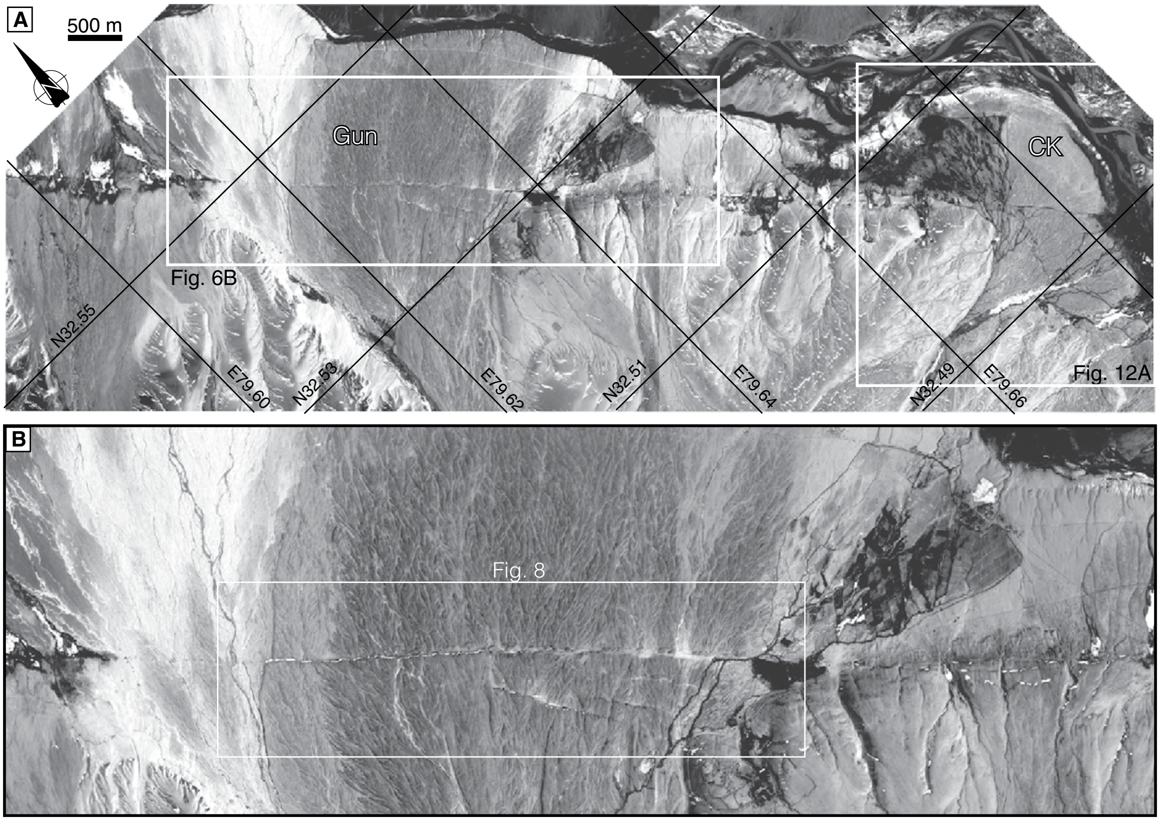

Figure 6. (A) *Ikonos* satellite image (pixel size = 1 m, image #90771, acquired in April 2002) of sites Gun and Chaxikang (CK). (B) Close-up of Gun site.

sample (Gun 27) being discarded after the first iteration of the statistical analysis (one outlier out of five samples, i.e., 20% of the samples; Fig. 10; Table 3). It is not meaningful to apply the criterion again here due to the limited number of samples on T3 (which would reject each sample one by one until the two samples with similar ages remain). The four remaining samples yield a median age of 31.4 (+9.0/–4.4) ka. On T2, the ages range from 12 to 146 ka. The four oldest samples were discarded after three successive iterations (four outliers out of 12 samples, i.e., 33% of the samples; Fig. 10; Table 3). The eight remaining samples yield a median age of 16.5 (+5.5/–3.8) ka, which is consistent with the fact that T2 is lower than, and inset in, T3. On T1, the ages range from 7 to 55 ka. The four oldest samples and the youngest one were discarded after three successive iterations (five outliers out of 11 samples, i.e., 45% of the samples; Fig. 10; Table 3). The median age of the remaining six samples is 12.2 (+3.5/–2.5) ka.

It is plausible that T3 was emplaced as a high-energy debris-flow fan during the interglacial postdating the late marine isotope stage (MIS) 3 (ca. 40 ka), at places the largest glacial advance in Tibet (e.g., Finkel et al., 2003; Mériaux et al., 2004; Owen et al., 2008; Chevalier et al., 2011a; Heyman et al., 2011; Hetzel, 2013), explaining its rough surface topography compared to those of T2 and T1, which are clearly post–Last Glacial Maximum (LGM) to early Holocene terraces. The scatter of ages toward older ages on T1 and T2 may be due to their small surface areas, close to the fault. It may also be related to the fact that these terraces were emplaced at the distal end of a rather long and winding fluvioglacial valley and catchment, with several moraines and terrace deposits located upstream, which are all possible sources of samples with significant pre-exposure. Finally, contamination of lower, younger surfaces by samples from older, higher ones might have been enhanced by the ubiquitous presence of channels oblique to the terrace risers. The fact that most of the oldest ages on T1 come from samples on the smallest terrace patch upstream is consistent with this inference. T1, which is almost at the level of the present-day riverbed downstream from the fault, is likely much younger than T2. A mid-Holocene age for T1 would be more consistent with other similar Tibetan alluvial sites (e.g., Van der Woerd et al., 1998, 2000, 2002; Mériaux et al., 2004, 2005, 2012; Li et al., 2005; Cowgill et al., 2009; Gold et al., 2009, 2011; Harkins et al., 2010; Chevalier et al., 2011b, 2012) and would imply a significant average inheritance in all the samples.

Slip-Rates

The T3 fan offset (120 ± 30 m) is associated with the median age of T3 (31.4 [+9.0/–4.4] ka), resulting in a minimum slip-rate of 3.8 (+1.5/–1.1) mm/yr. Associating the best-defined and best-constrained offset (38 [+10/–5] m) with the median age of T2 (16.5 [+5.5/–3.8] ka; the T2/T1 riser offset began accumulating following abandonment of T2) results in a slip-rate of 2.5 ± 1 mm/yr. Averaging these two rates yields a minimum of 3.1 ± 0.4 mm/yr at Gun for the last 30 ka.

Chaxikang (CK) Site

Geomorphology

The Chaxikang (CK) site is located downstream from the Chaxikang moraines and 7 km SE of the Gun site, near the village of Chaxikang (Fig. 5). At the Chaxikang site, several alluvial fans (F2, F3, and F3′) were deposited and cut by the Karakorum fault. The fans and

Geological Society of America Bulletin, published online on 29 July 2015 as doi:10.1130/B31269.1

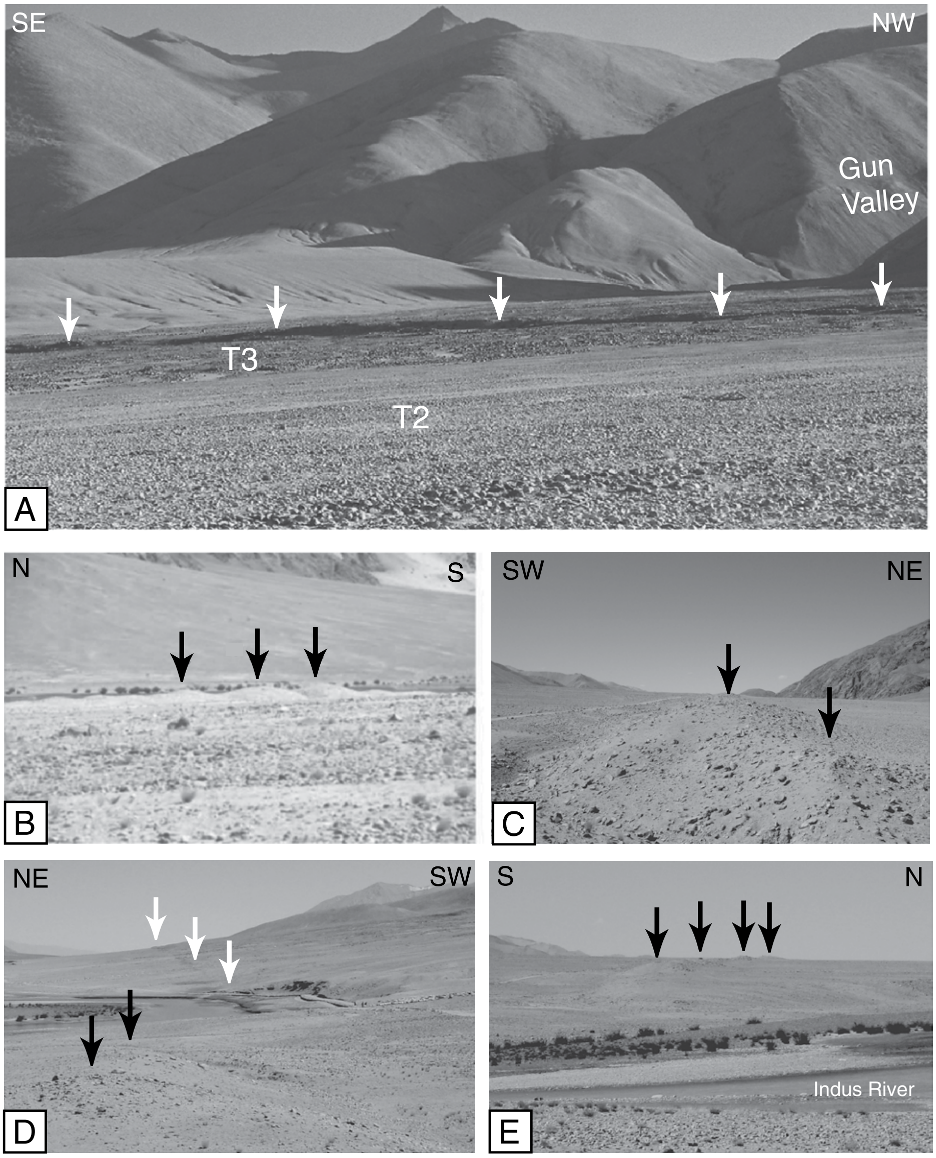

Figure 7. Field photos of Gun site (location in Figs. 3B and 5A). (A) General view of T3 and T2. Mid-valley branch of the Karakorum fault is highlighted by NE-facing scarp (white arrows). (B–E) Large cumulative pressure ridges (black arrows) located just north of Gun site (32.679°N, 79.483°E) along the Karakorum fault (white arrows). Scale: the fault scarp is ~4–6 m high and the mole tracks in B, C, and D are ~20 m high.

moraines lie between the Indus River and the north Ayilari Range, at the outlet of a large U-shaped glacial valley (Chaxikang valley; Figs. 3 and 5). At periods of large glacial extents, the glacier almost reached the Indus River, located ~20 km away from the ice cap that once topped that part of the Ayilari Range (5800–5900 m). Today, only ice remnants are visible, in contrast to the larger ice cap to the south near Manikala (Fig. 3). Following the work of Liu (1993) based on *SPOT* image interpretation, Chevalier et al. (2011a) mapped four distinct moraines. The youngest moraine (M1, Fig. 5) extends ~1.6 km NE of the range front and is incised ~20–30 m by the present Chaxikang River. Only one set of abandoned terraces is visible along the current Chaxikang River. An intermediate moraine complex (M2) extends ~3.6 km from the range front and is incised by a narrow, 50–60 m-deep canyon. The older moraine complex (M3) extends 5.2 km from the range front, where its terminus has been eroded and breached by the Chaxikang River. The M1, M2, and M3 moraines studied for paleoclimatic purposes (e.g., section 3.1.7 in Chevalier et al., 2011a) were formed during the LGM, MIS 3–4, and MIS 5–6, respectively, spanning a whole glacial cycle. Additional tills are located on both sides of the Chaxikang moraines, with one M4 till (M4* in Fig. 5) south of the Chaxikang valley now facing a triangular facet, indicative of right-lateral motion along the range-front fault. This moraine might not have a counterpart north of the valley because of dextral shift, and correlative erosion by glacial and fluvial action (e.g., Chevalier et al., 2005a).

The Chaxikang fan complex between the M3 moraine terminus and the Indus River is composed of three main imbricated fan deposits, F2, F3, and F3′ (Figs. 11 and 12). The youngest and lowest surface, F2, made of well-rounded cobbles/boulders ~10 – 50 cm in diameter, is located where the present-day Chaxikang River divides into several divergent channels (Figs. 5, 6A, 11D, and 12). Parts of the channels have been deviated for irrigation purposes along water canals that cross the natural channels. The next fan surface is F3, standing higher than the level of F2 and characterized by more deeply incised gullies. F3′, the oldest fan surface at the site, has broader bars that stand higher than F3. Detailed inspection of the fan complex on satellite images and in the field suggests that F3′ and F3, NE of the mid-valley fault, are smoother, lighter colored (Figs. 6A and 12), and more distal, with smaller cobbles and more subtle rills, and with radial channeling at high angle to the edge of the fan, as compared to F3 and F3′ SW of the fault (Figs. 12A and 12C). While the difference between F3 and F3′ is visible SW of the fault in the field and on the satellite images, the limit between these two surfaces NE of the fault is less clear. The mid-valley branch of the Karakorum fault, along which pull-apart sags are visible (Figs. 12A and 12C), cuts and right-laterally offsets the fan surfaces F3 and F3′. In addition to the mid-valley branch of the Karakorum fault, the F3 and F3′ fan surfaces SW of the fault are cut by several east-dipping normal faults that splay southward from the main Karakorum fault, with the highest cumulative scarps being ~4 m high. These normal faults belong to the transfer zone that marks the widening of the Gar pull-apart basin (see above and Fig. 3).

Offsets

Several right-lateral offsets are determined along the main branch of the Karakorum fault at site Chaxikang, even though none of them is as clear as at the Gun site. As the distal part of the fan, NE of the fault, is right-laterally displaced, it offsets the western bank of the Indus River, marked by the limit of the water at the date of the image (in 2002; Fig. 12), and also by the limit of the maximum flooding outlined by the sharp difference between the sloping rocky surface of the fan and a subhorizontal zone

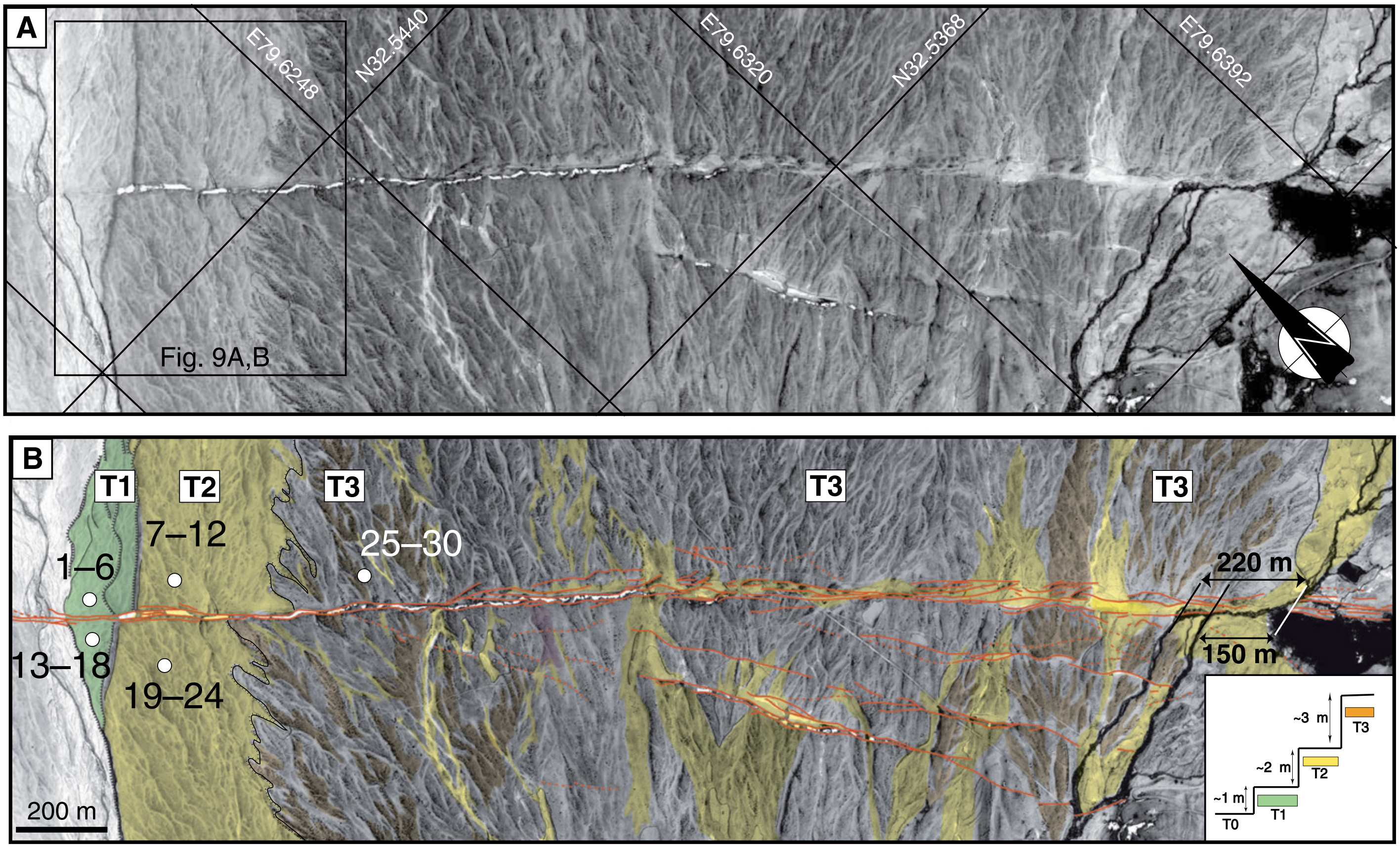

Figure 8. Close-up of Gun site on *Ikonos* image (A) and its interpretation (B). The river channels incising T3 to the east are offset by ~150 and 220 m. Sample location is approximate due to military restriction while in the field, preventing us from recording individual global positioning system (GPS) positions. Note that the yellow patches on T3 represent lower surfaces incised on T3, corresponding to the level of T2.

occupied by vegetation (Fig. 12). Even though the Indus River banks, which are not yet passive geomorphic markers, may have evolved through time, we can tentatively assign a 150–180 m offset of its western bank today, which is on the order of other features' offsets, as described next. Despite the fact that the F3/F2 riser SW of the fault is not present NE of the fault, an offset of ~190 m may be assigned to the eastern edge of F3. Finally, the F3′/F3 riser mapped south of the fault may be inferred NE of the fault, and this yields a possible offset of at least 200 m (Fig. 12).

The mid-valley fault scarp faces NE along the western half of the fan (as evidenced by channels crossing the fault and veering toward NW), but it faces SW along the eastern half of the fan (Fig. 12A). This change of scarp facing direction occurs exactly halfway across the fan (near where samples CK-25, 26, and 27 were collected), i.e., exactly where expected in case of a horizontally shifted fan surface. Some N-S–striking normal faults connected to the mid-valley fault make up scarps across the SW part of the fan. These normal faults make parts of the fan go down but do not alter the general shape of the fan and main fault scarp. It should also be noted that the NE part of the fan, displaced in front of the main Indus River course, does not show any sign of river incision across its surface in the form of a steep and higher riser, but instead, similar to the SW part, it smoothly merges with the Indus riverbed, indicating minor or no vertical motion across the mid-valley fault. Although the only topographic data available are at the 1:50,000 scale, it is interesting to note that reconstructing the 4240 m contour yields an offset of ~200 m. Coincidentally or not, this offset is once again in agreement with the F3′/F3 offset, the offset of the eastern edge of F3, and the offset of the western bank of the Indus River.

Surface Ages

In total, 32 cobbles were collected on the three subfans F2, F3, and F3′ (Figs. 5, 12, and 13; Table 2): 16 (CK-1–9, 25–27) NE of the fault on F3′, six (CK-19–24) SW of the fault on F3, and 10 on F2 (CK-12–18) SW of the fault. On the fans, we sampled granite and quartzite sample pairs where possible (Figs. 4 and 13), as described in the methods section. The sample age distributions on the three sampled surfaces show large scatter with no clear cluster of ages. However, after outlier rejections, they do not overlap and represent three distinct age populations. The 16 samples on F3′ range from 19 to 59 ka. Two successive iterations of Chauvenet's criterion discarded the three oldest and the two youngest samples (five outliers out of 16 samples, i.e., 31% of the samples; Fig. 13; Table 3). It is not meaningful to apply the criterion again here because it would reject each sample one by one until too few samples remain. The remaining 11 samples on F3′ yield a median age of 43.4 (+5.2/–4.9) ka. On F3, six sample ages range from 13 to 35 ka. Two successive iterations were sufficient to discard the oldest and the youngest sample (two outliers out of six samples, i.e., 33% of the samples; Fig. 13; Table 3). The remaining four samples yield a median age of 24.5 (+3.2/–2.9) ka. Lastly, on F2, 10 sample ages range from 6 to 38 ka. Three successive iterations were sufficient to discard the three oldest and the youngest samples (four outliers out of 10 samples, i.e., 40% of the samples; Fig.

13; Table 3). The remaining six samples yield a median age of 14.9 (+4.7/–3) ka. Note that the median values of all ages before outlier rejection for the three surfaces, F3′, F3, and F2, are similar at 44.0 (+8.4/–7) ka, 24.5 (+6.6/–9) ka, and 16.8 (+8.6/–5.5) ka, respectively.

It is worth noting the similarity in ages between the main surfaces dated at Gun and at Chaxikang. F2, dated at 12–20 ka, is similar in age to T2 at site Gun (12–22 ka), and both are clearly post-LGM. At first glance, T3 at site Gun (27–40 ka) has a similar age as the older surface F3-F3′ at Chaxikang (21–48 ka), and may both be correlated to the interglacial following MIS 3, which is well expressed in the moraine M2 at this site (Figs. 5 and 13; Table 2; Chevalier et al., 2011a). We will further detail climatic correlations with surface ages in the discussion section.

Slip-Rates

The F3/F2 riser is only well defined SW of the fault. Assuming that its continuation NE of the fault corresponds to the southeastern rim of F3, then the 190 m offset may be bracketed between the ages of F3 and F2, i.e., ca. 15 and ca. 25 ka, yielding a rate of 8–12 mm/yr. The F3′/F3 riser is not clearly defined NE of the fault. Assuming that the total cumulative 200 m offset of the fan complex is also the offset of F3′/F3, then its age may be bracketed between the ages of F3 and F3′, i.e., ca. 25 and ca. 43 ka, yielding a rate of 4–8 mm/yr. Both these rate determinations assume that the inset fans F3 and F2 were deposited across the fault, which, in the absence of ages on each of these surfaces on both sides of the fault, remains to be demonstrated. Taking the F3′ fan offset of 200 m and the oldest surface age of 49 ka (CK-7B) yields a plausible minimum rate of 4.1 mm/yr. However, matching the ~200 m offset we measured using four different markers with the oldest age we have for this site before (59 ka, CK-3B) or after (49 ka, CK-7B) outlier rejections, respectively, yields a minimum rate of 3.4 mm/yr, which is similar to the value we determined at site Gun. In the absence of additional age constraints on all surfaces, these slip-rates should be considered cautiously.

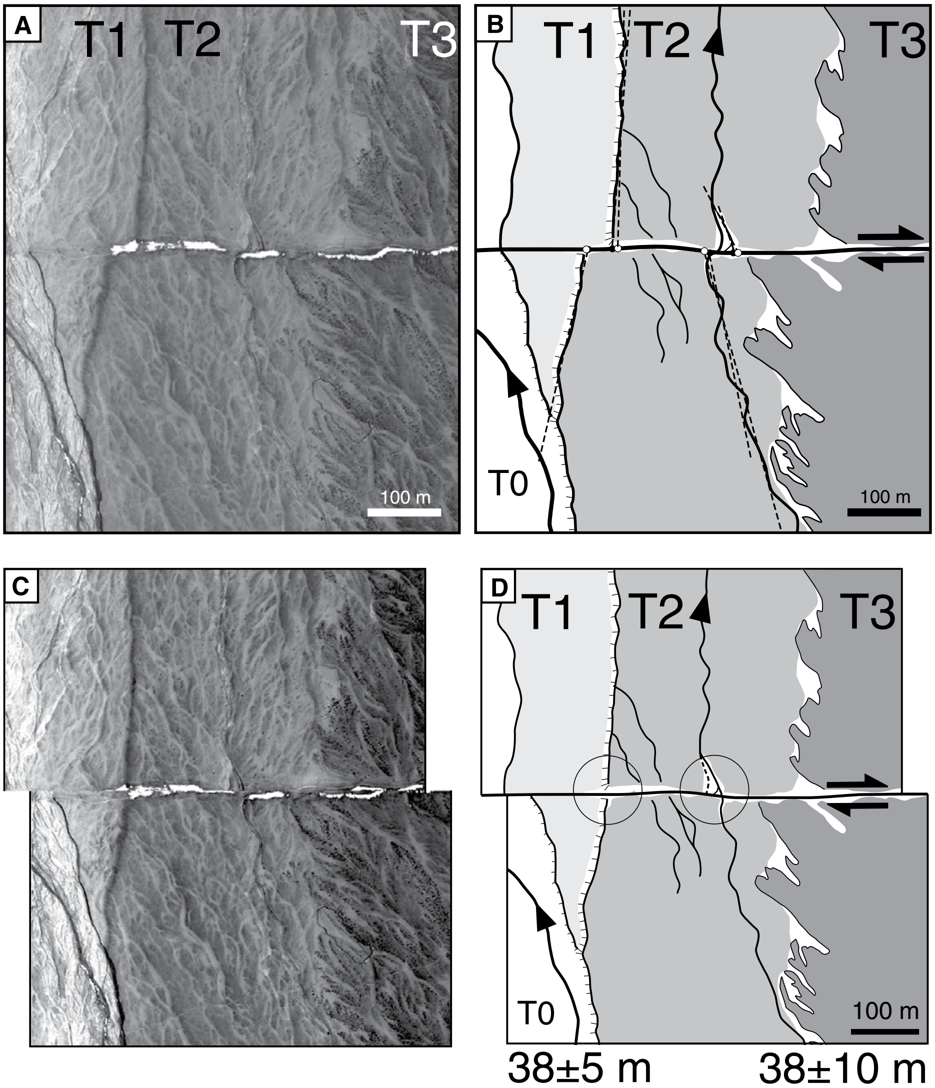

Figure 9 (*on this and following page*). Offsets at Gun site. (A–B) Gun site today. (C–D) Retro-deforming the *Ikonos* image by 38 m realigns both the T2/T1 riser and channels on T2.

Gar Fan (GF) Site

Geomorphology

The Gar fan site (GF) is located ~35 km SE of Chaxikang, and just NW of the Gar transfer zone (Fig. 3). It is a debris-flow fan with meter-high levee ridges located at 32°15′N, 79°52′E, at an elevation of ~4350 m above sea level (Fig. 14). The fan surface dips >8° to the NE (determined from topographic map contours), shows a convex-upward morphology typical of debris-flow fans (Fig. 15B), and was fed by a rather short (<3-km long) and steep catchment, which drains only part of a large triangular facet at the front of the Ayilari Range. The V shape of the valley attests that it was never glaciated, even though an ice cap covered the summits of the Ayilari Range during glacial maxima. Here, the Karakorum fault has one main strike-slip branch, with several minor extensional splays, particularly at the foot and across the triangular facets, which bear traces of recent earthquakes (Figs. 14 and 15B). The fault traces are underlined by springs and vegetation patches. The main strike-slip branch of the fault cuts and offsets the bar and swale morphology on the surface of the Gar fan debris-flow fan, as well as other adjacent catchments and surfaces to the NW and SE (Figs. 14, 15D, and 15E).

Offsets

At the Gar fan site, cumulative channel and surface offsets are clear in the field and can be measured by retrodeforming the satellite images across the Gar fan and its vicinity (Fig. 16). The Gar fan surface is clearly the result of several phases of deposition and channel incision. Its surface shows patches with variable roughness that can be attributed to progressive aging and surface smoothing by alteration of the rock at its surface and/or accumulation of soil or loess. Several cumulative offsets of channels incised in its surface can be determined at 12 and 22 m. The 12 m offset is the smallest offset visible on the images and corresponds to the reconstruction of several channels incised in the middle of the fan and the active bed to the NW (Fig. 16B). The 22 m offset allows oblique channels to be

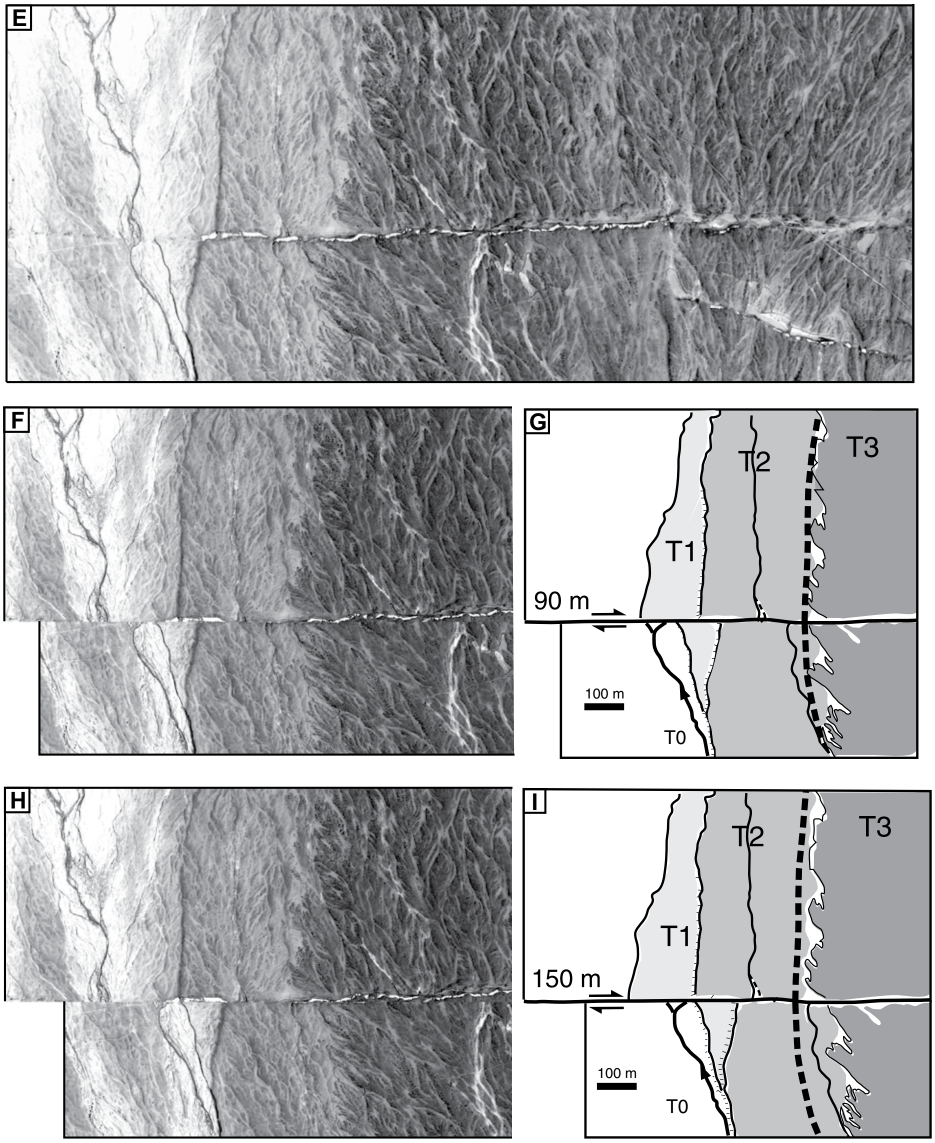

Figure 9 (*continued*). (E–I) Here, 90–150 m (dashed lines), i.e., 120 ± 30 m, of back slip realigns the T3/T2 limit.

reconstructed on the Gar fan surface to the SE, as well as a small drainage NW of the Gar fan, which is made of channels deeply incised into an older surface (Figs. 15D, 15E, and 16C). It also realigns both rims of the Gar fan outlined on the satellite image and in the field by the color difference between the fan surface and the nearby active stream beds. Last, a total offset of 60–70 m reconstructs a second channel from the drainage NW of the Gar fan, as well as several additional features (Figs. 15D, 15E, and 16D). It may also be viewed as reconstructing the margin of the Gar fan, to a lesser extent.

Surface Ages

Fourteen samples (GF 1–14; Table 2; Figs. 14 and 17) were collected on the levees of the Gar fan debris-flow downslope from the main fault. The sample ages range from 6 to 42 ka and show a bimodal distribution with an upper and a lower tail (Fig. 17). One iteration of Chauvenet's criterion discards the two oldest samples (two outliers out of 14 samples, i.e., 14% of the samples; Fig. 17; Table 3). The remaining 12 samples yield a median age of 13 (+10.3/–3.4) ka. Note that taking all samples from Gar fan yields a similar median age of 15.2 (+13.0/–5.3) ka. The age of Gar fan is thus similar to the ages of T2-T1 at Gun and F2 at Chaxikang, in agreement with the formation of debris-flow fans and terraces after the LGM. While the first iteration of the criterion does not justify the rejection of ages older than 15 ka, the main probability density function (pdf) is nevertheless centered around 10 ka (Fig. 17), or the early Holocene. This may further support the inference that Gar fan formed as a result of intense debris-flow emplacement during the glacial-interglacial transition at the end of the LGM and that the age of 13–15 ka is a maximum for the Gar fan surface.

Slip-Rates

Taking the median age of Gar fan (13 [+10.3/–3.4] ka) and the 22 m offset of the channels incised on its surface defines a minimum bound of the slip-rate of 1.7 mm/yr. If the most significant peak of the age distribution is considered, i.e., 10 ka, a slightly higher rate of 2.2 mm/yr is determined. This rate is on the order of, but slightly lower than, what we determined at sites Gun and Chaxikang. Note that taking the 65 ± 5 m offset reconstruction of the margin of the Gar fan yields a slip-rate of 4.9–6.5 mm/yr (if using 13 or 10 ka, respectively). Therefore, the 1.7 or 2.2 mm/yr rate is strictly a minimum.

DISCUSSION

Climatic Origin of Regional Geomorphology along the Southern Karakorum Fault

The ages of the fan surfaces at Chaxikang indicate that they formed contemporaneously or after emplacement of moraines M2 and M1 (Fig. 13). F3′, dated at ca. 38–48 ka, may be related to the deglaciation following the major glacial advance dated at ca. 40 ka (MIS 3) along the Ayilari Range to the SE (e.g., Chevalier et al., 2005a, 2011a) or elsewhere in Tibet (e.g., Finkel et al., 2003; Mériaux et al., 2004; Owen et al., 2008; Chevalier et al., 2011a; Heyman et al., 2011; Hetzel, 2013). F3, dated at 21–28 ka, predates the LGM (20 ka), and its age overlaps with the age of T3 at Gun (27–40 ka). The age of F2 (12–20 ka) indicates that it formed after the LGM, thus most probably after the emplacement of moraine M1 (although M1 has not been dated here, it may correspond to the last significant maximum advance after the largest advance of M2, Fig. 5). Its age is similar to the age of T2 at Gun (12–22 ka). The correspondence between the glacier reconstructions and the fan and terrace emplacement at both Gun and Chaxikang sites supports the geomorphic age determinations and a posteriori validates both the assumptions made about outlier rejections and interpretation of the cobble ages. This reflects accumulation of ^{10}Be nuclide mostly following surface emplacement, with also minor postdepositional modification. Regarding Gar fan, the fact that the fan emplacement age (10–23 ka) appears to also be coeval with both T2-T1 at Gun and

Geological Society of America Bulletin, published online on 29 July 2015 as doi:10.1130/B31269.1

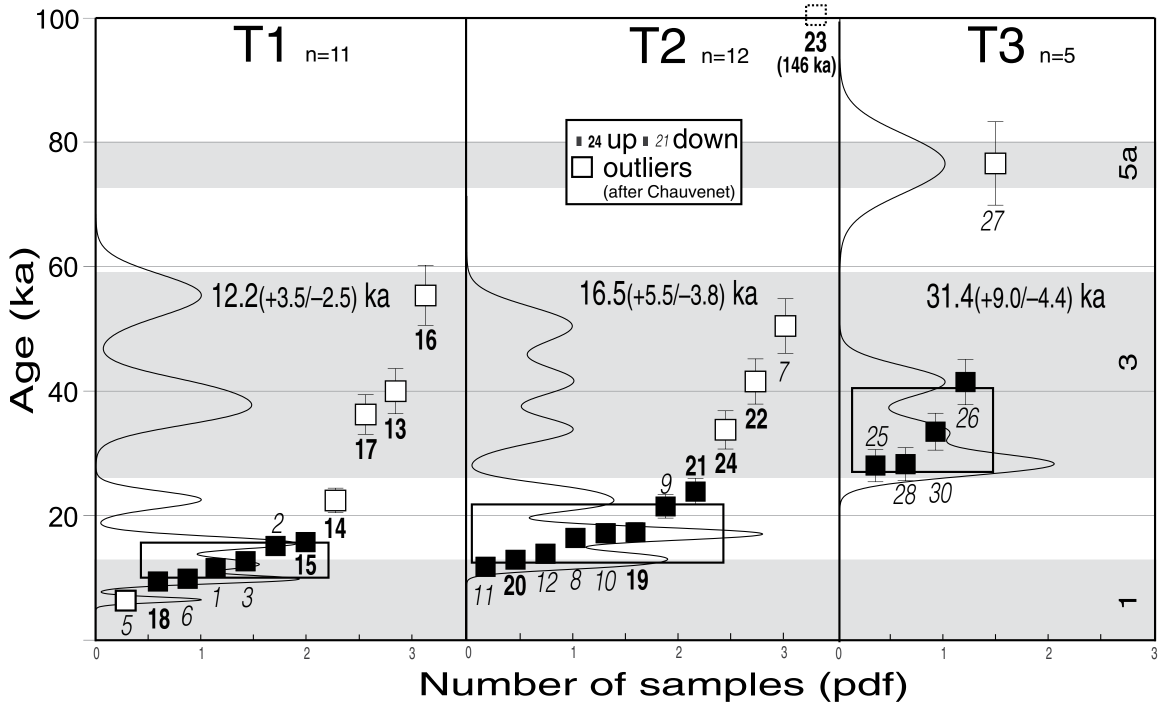

Figure 10. ^{10}Be ages and probability density function (pdf) distributions of surface samples at Gun site. Outliers (white) were rejected following Chauvenet's criterion (see text for details). Median ages with 1σ uncertainty were calculated after rejecting outliers. Gray-shaded sectors are marine isotope stages (MIS) with corresponding numbers to the right (Imbrie et al., 1984); up/down—upstream/downstream from fault.

F2 at Chaxikang (we discussed earlier the possibility of an early Holocene emplacement age at 10 ka, corresponding to the best-defined age distribution peak) may suggest that it was formed as an intense debris-flow fan surface deposited during the glacial-interglacial transition at the end of the LGM.

To the south, at the Manikala site (Chevalier et al., 2005a; C5 in Fig. 1), the moraines dated at ca. 20–42 ka (M1) and ca. 150–195 ka (M3; Chevalier et al., 2011a) correlate with glacial stages MIS 2–3 and MIS 6, similar to Chaxikang site M1 and M3 moraines, respectively (Chevalier et al., 2011a). Further south, along the Menshi-Kailas segment of the Karakorum fault, as well as in the Pulan graben (C12 in Fig. 1), Chevalier et al. (2012) dated 12 surfaces at seven sites, at a 200 ka time scale. At Menshi site, the ages of T1 (19–35 ka) and T3 (70–137 ka), even though scattered, may indicate emplacement during warm and humid interstadials or interglacials, which are periods considered favorable to fluvial deposition. Indeed, on T1, a few sample ages are post-LGM and a few others are post–MIS 3 (ca. 40 ka; similar to fans F3 and F3′ at Chaxikang), while on T3, samples appear to have been deposited during the MIS 5 interglacial.

Further east, at site La Zhi Tang (Chevalier et al., 2012), the well-defined cluster at 10–12 ka on T1s (*n* = 16 out of 21 samples) appears to be coeval with the plateau of ages at Gar fan (ca. 10 ka) and to T1 at the Gun site, and it reveals a clear depositional event during the early Holocene climatic optimum, a warm and humid pluvial that has now been demonstrated to be a major period of fan deposition and terrace aggradation in other parts of Tibet (e.g., Mériaux et al., 2004, 2005; Van der Woerd et al., 1998, 2000; Hetzel, 2013). T2 at La Zhi Tang, dated at 41–63 ka, may have been deposited during the MIS 3 interstadial, similar to F3′ at Chaxikang. Just east of the La Zhi Tang site, at the base of Mount Kailas (Fig. 1), Chevalier et al. (2012) dated three moraine crests: A Qu at ca. 22–37 ka, West Xiong Se at 17–48 ka, and East Xiong Se at 13–17 ka. While A Qu and West Xiong Se most likely reflect an emplacement during MIS 2–3 glacial stages, coeval with Manikala M1, East Xiong Se corresponds to an LGM emplacement, most likely like Chaxikang M1. Just south of Kailas, where the Karakorum fault connects with the normal fault following the base of the Gurla Mandhata in the Pulan graben (Fig. 1), Chevalier et al. (2012) studied one fluvial site (Rengongpu) and one moraine site (Rongguo), also studied by Owen et al. (2010). At Rengongpu, T3 ages are more scattered (27–42 ka) and may be correlated to a post–MIS 3 glacial, similar to F3-F3′ at Chaxikang and T3 at Gun. T2 is 6–11 ka and T1 is 6 ka, clearly defining emplacement ages during the early Holocene climatic optimum, similar to La Zhi Tang T1 surfaces and to Gar fan, and T1 at Gun. At Rongguo, M1 (19–45 ka) from the study by Chevalier et al. (2012) (corresponding to M4a [9–55 ka] of Owen et al., 2010) is consistent with an emplacement during MIS 2–3, similar to the West Xiong Se, A Qu, and Manikala M1 moraines (as well as possibly Chaxikang M1), while M2 (28–95 ka) from the study by Chevalier et al. (2012) at Rongguo (corresponding to M3 [28–64 ka] of Owen et al., 2010) may coincide with the short glacials during MIS 5, closer to Chaxikang M2 ages.

Along the northern end of the Bangong-Chaxikang segment, where the Karakorum fault splits into two parallel strands, the Bangong and Tangtse branches, two geomorphological studies revealed a 11–14 ka debris-flow fan emplacement age for the Bangong strand (Brown et al., 2002) and a 31–37 ka debris-flow age for the Tangtse strand (Bohon, 2014). The former fan deposition ages may correspond to T1 at Gun, Gar fan, T1 at La Zhi Tang, and

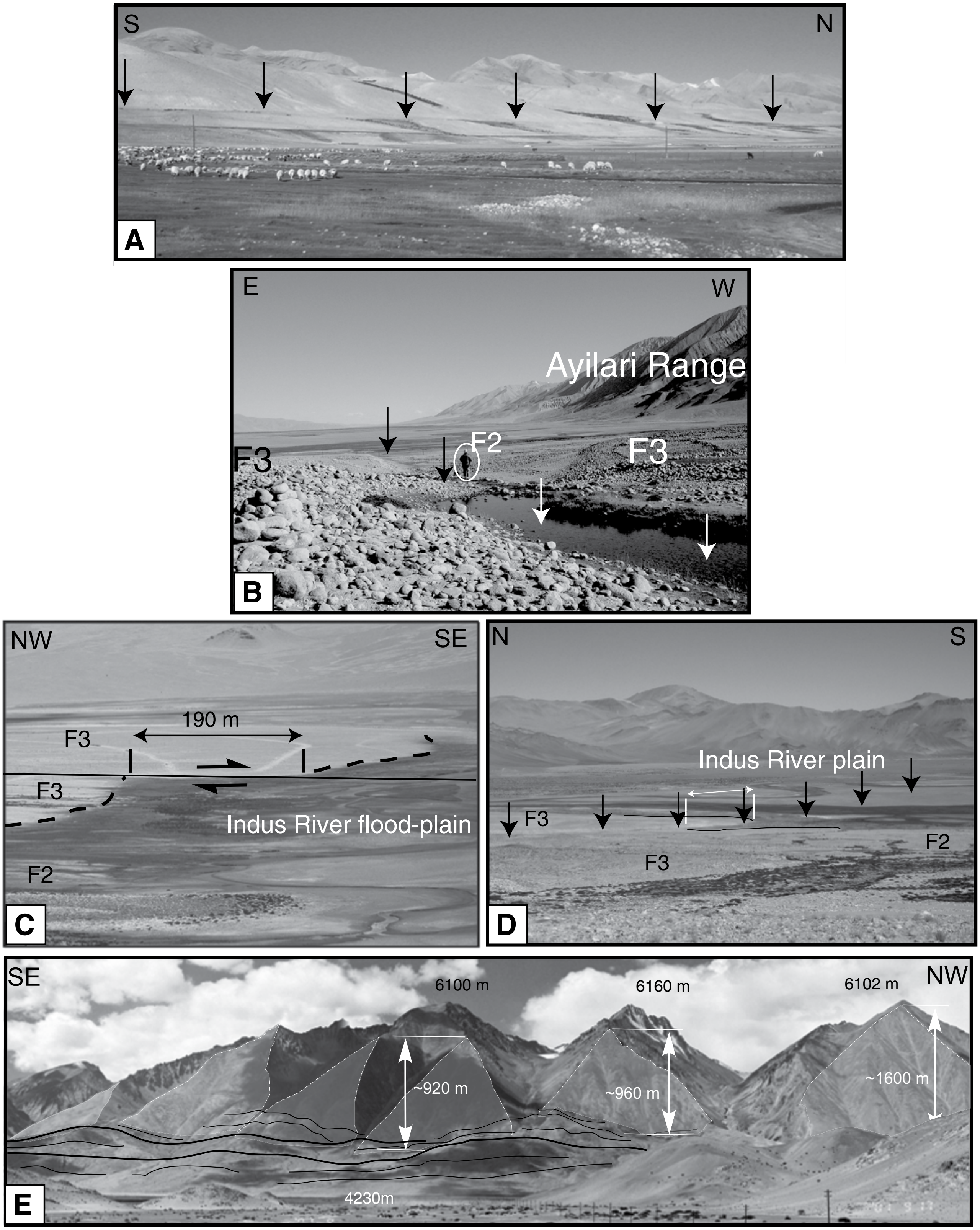

Figure 11. Field photos of Chaxikang site (location in Figs. 3B and 5A). (A) Mid-valley fault highlighted by springs and vegetation patches (black arrows). (B) Large cobbles located on fans along mid-valley branch of Karakorum fault, highlighted by arrows, with NE side up. Small water-filled pull-apart basins can be seen along fault trace. Person circled for scale. (C–D) Field views of F3/F2 edge offset (190 m). (E) Approximately 1000 m-high triangular facets along range front south of Chaxikang site with faults represented by black lines (thicker for main).

Geological Society of America Bulletin, published online on 29 July 2015 as doi:10.1130/B31269.1

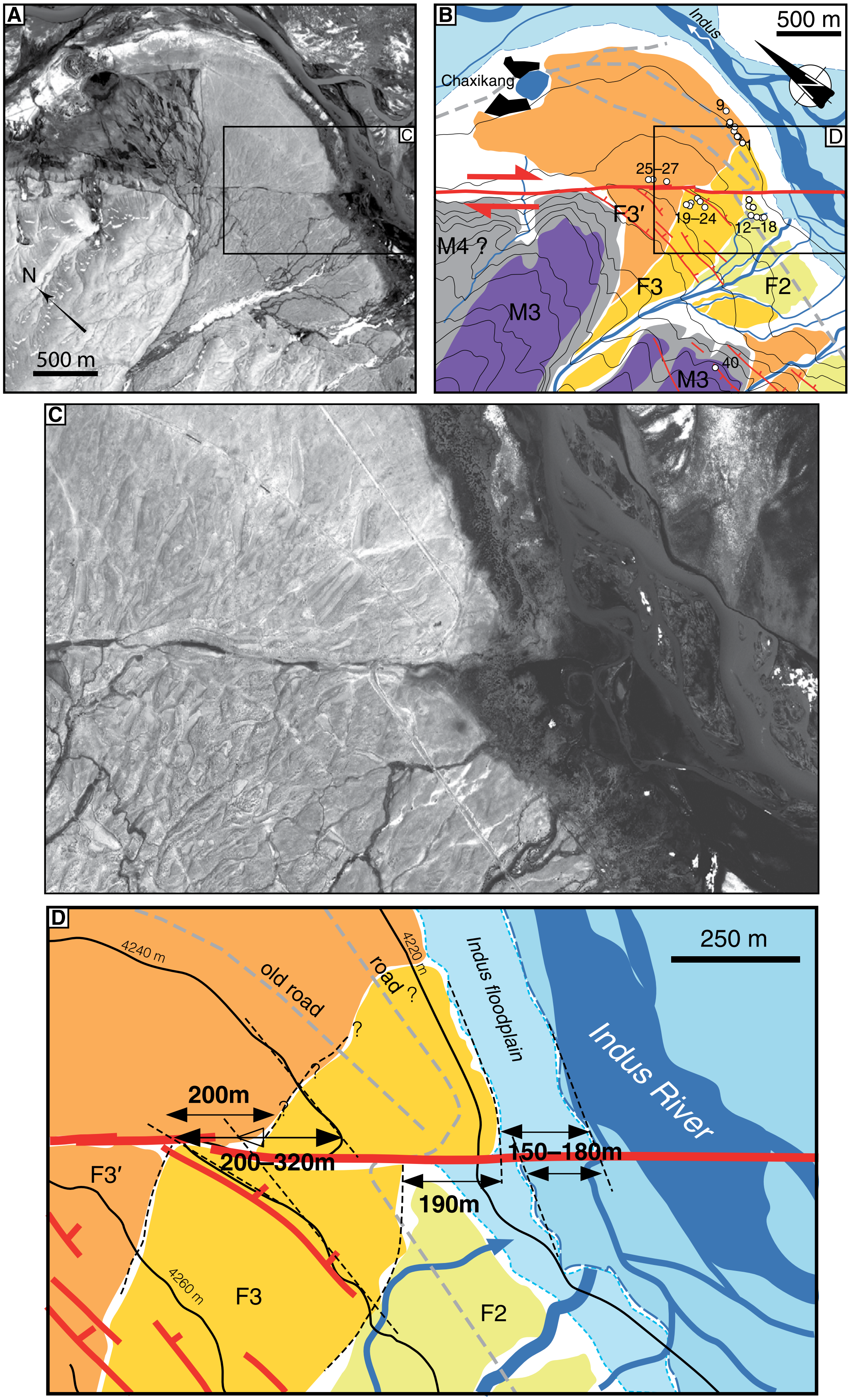

Figure 12. Offsets at Chaxikang site: *Ikonos* image of Chaxikang site (A) with interpretation (B). (C–D) Several offset values may be determined: The eastern rims of F3 may be reconstructed with an offset of 190 m, while the very distal parts of the fans show an offset of 150–180 m. The F3′/F3 riser may be offset by 200 m, but its location is unclear. Taking the 4240 m topographic contour allows us to measure an offset of at least 200 m. See text for details. Location is shown in Figure 6. Contours are from 1:50,000 Chinese topographic maps. Legend is same as in Figure 5B.

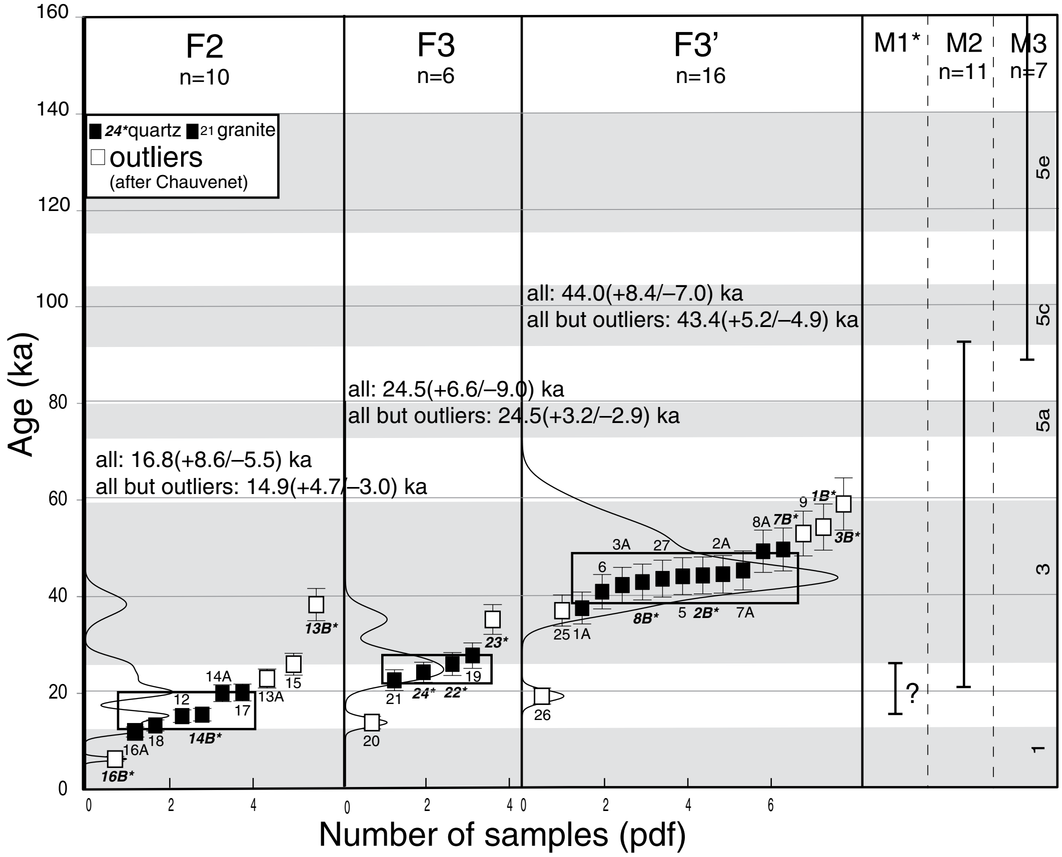

Figure 13. ^{10}Be ages and probability density function (pdf) distributions of surface samples at Chaxikang site. Legend is same as in Figure 10; quartz/granite—original quartzite/granite sample collected; M1, M2, M3—moraines from Chevalier et al. (2011a). The age of M1* has not been dated but is inferred to be Last Glacial Maximum (see text for details).

to some extent to T2 at Rengongpu, while the latter may be coeval with T3 at Gun and T3 at Rengongpu. Overall, by compiling all the dated alluvial and glacial deposits (Chevalier et al., 2011a) in southwestern Tibet, it appears that the major fan- or terrace-building episodes are regionally correlated and thus related to climatic events, as expected.

Significance of ^{10}Be Model Age Distribution

Our interpretation of age distribution on alluvial surfaces is mostly determined by the processes at play when these geomorphic markers are emplaced. We view river terraces or alluvial-fan emplacement as discrete depositional events followed by surface abandonment and incision by the active streams. This interpretation is probably valid in arid environments where streams are intermittent and mostly fed by rare storms or summer meltwaters where glaciers are present. It is thus expected that if the rocks mantling these geomorphic markers originated from a similar source (assuming negligible hillslope erosion and transport time), their cosmogenic isotope content should be very similar, with a tight cluster of ages. However, such clusters may only show up if a sufficient number of samples are analyzed on each one of the markers. Deviation from the cluster toward younger or older ages (i.e., toward lower or greater isotope concentration) only affecting part of the sample ages distribution can thus be viewed as the result of a specific process affecting these samples and can justify their a posteriori sorting.

Ages obtained for pairs of samples with different lithology (quartzite vs. granite, 8 pairs; Fig. 4; Table 2) show no trend. Quartzite model ages can be both older and younger than granite model ages for similar samples (CK-1, 3, 7, and 13 vs. samples CK-8, 14, and 16, respectively). Only one pair (CK-2) yielded the same age. If granite samples were always younger than quartzite samples, it would imply that granite samples are more significantly affected by erosion compared to quartzite. The absence of such a trend thus suggests that erosion is a minor player at the time scale and for the samples considered here. In addition, Chaxikang pairs of ages range from 6 to 59 ka (Fig. 4; Table 2), largely covering the glacial-interglacial transition period, as well as all the terrace ages we studied here. Therefore, the fact that no trend is observed also confirms that erosion does not significantly affect the ages, at least not in a systematic manner.

Slip-Rates along the Southern Half of the Karakorum Fault

The first qualitative estimates of the Karakorum fault's late Quaternary slip-rate (Liu, 1993) were based on climatic inference, given the dearth of direct dating techniques at the time. Because Liu (1993) inferred that the Chaxikang fans and moraines were emplaced ca. 10 and 18 ka, instead of ca. 12–48 ka and ca. 44–84 ka (M2 median or oldest age), respectively, the slip-rate he inferred (>18–35 mm/yr) is therefore two to four times larger. A slip-rate two to four times smaller, i.e., 4.5–9 mm/yr, would be consistent with what we determine in this study at Chaxikang (>3.4 mm/yr).

Using dating techniques such as cosmogenic surface-exposure ^{10}Be dating, our results here complement those from Chevalier et al. (2005a, 2012) as well as Brown et al. (2002) and Bohon (2014), and provide the most comprehensive set of quantitative geomorphic constraints on the slip-rate along the southern Karakorum fault. The extremely clear (on satellite images and in the field, large mole tracks, etc.), simple (not transpressive nor transtensive, no change of direction, etc.), and linear Bangong-Chaxikang segment of the Karakorum fault has long been

Geological Society of America Bulletin, published online on 29 July 2015 as doi:10.1130/B31269.1

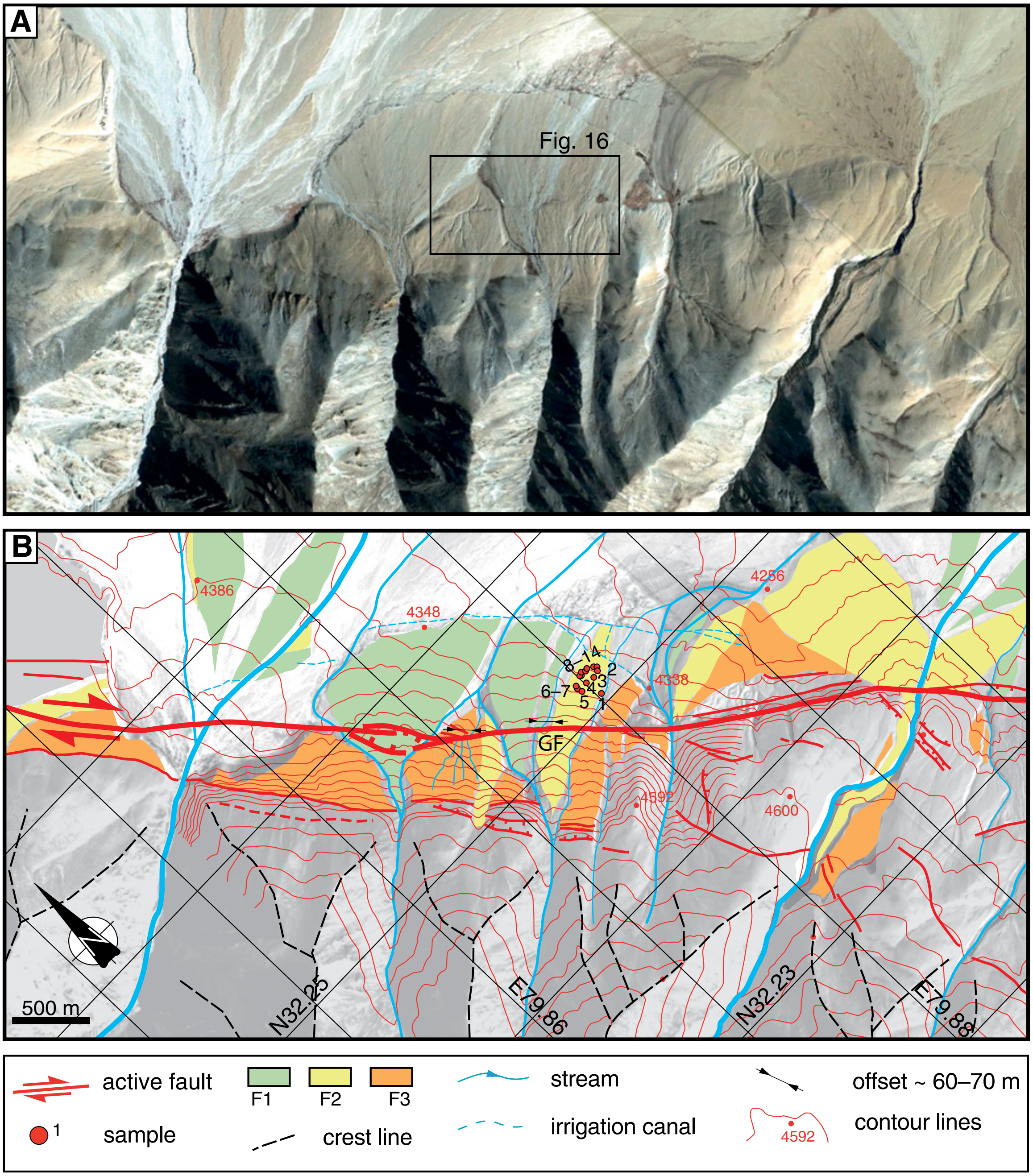

Figure 14. Gar fan site: *Quickbird* satellite image (Google Earth) (A) and geomorphological interpretation (B). Contours are every 20 m.

the center of attention, but its access is now restricted due to its strategic location near international borders. In particular, the 120 km offset of the Indus River that is visible along this segment has been used as a minimum geological offset to derive the long-term slip-rate or initiation age of the Karakorum fault (e.g., Gaudemer et al., 1989; Liu, 1993; Lacassin et al., 2004; Valli et al., 2007, 2008). Despite the importance of determining a late Quaternary slip-rate along this important segment, no quantitative data were available until now. Even though our rates may not be as well constrained as at other sites to the south (Chevalier et al., 2005a, 2012) or to the north (Brown et al., 2002; Bohon, 2014), they nevertheless provide new data that allow us to suggest the most likely slip-rate values along the Bangong-Chaxikang and Gar Basin segments of the Karakorum fault, which are summarized in Figures 18B and 18C. From NW to SE, the slip-rate along the mid-valley branch of the Bangong-Chaxikang segment of the Karakorum fault over a ca. 10–60 ka age range is 3.1 ± 0.4 mm/yr at Gun, >3.4 mm/yr at Chaxikang, and >1.7 mm/yr at Gar fan.

South of Gar fan, in the Gar Basin segment of the Karakorum fault, along the range-front fault only, the slip-rate at Manikala is a minimum of 5.4 mm/yr at time scales 0–40 ka, or if the oldest age is favored (Brown et al., 2005), slightly

Geological Society of America Bulletin, published online on 29 July 2015 as doi:10.1130/B31269.1

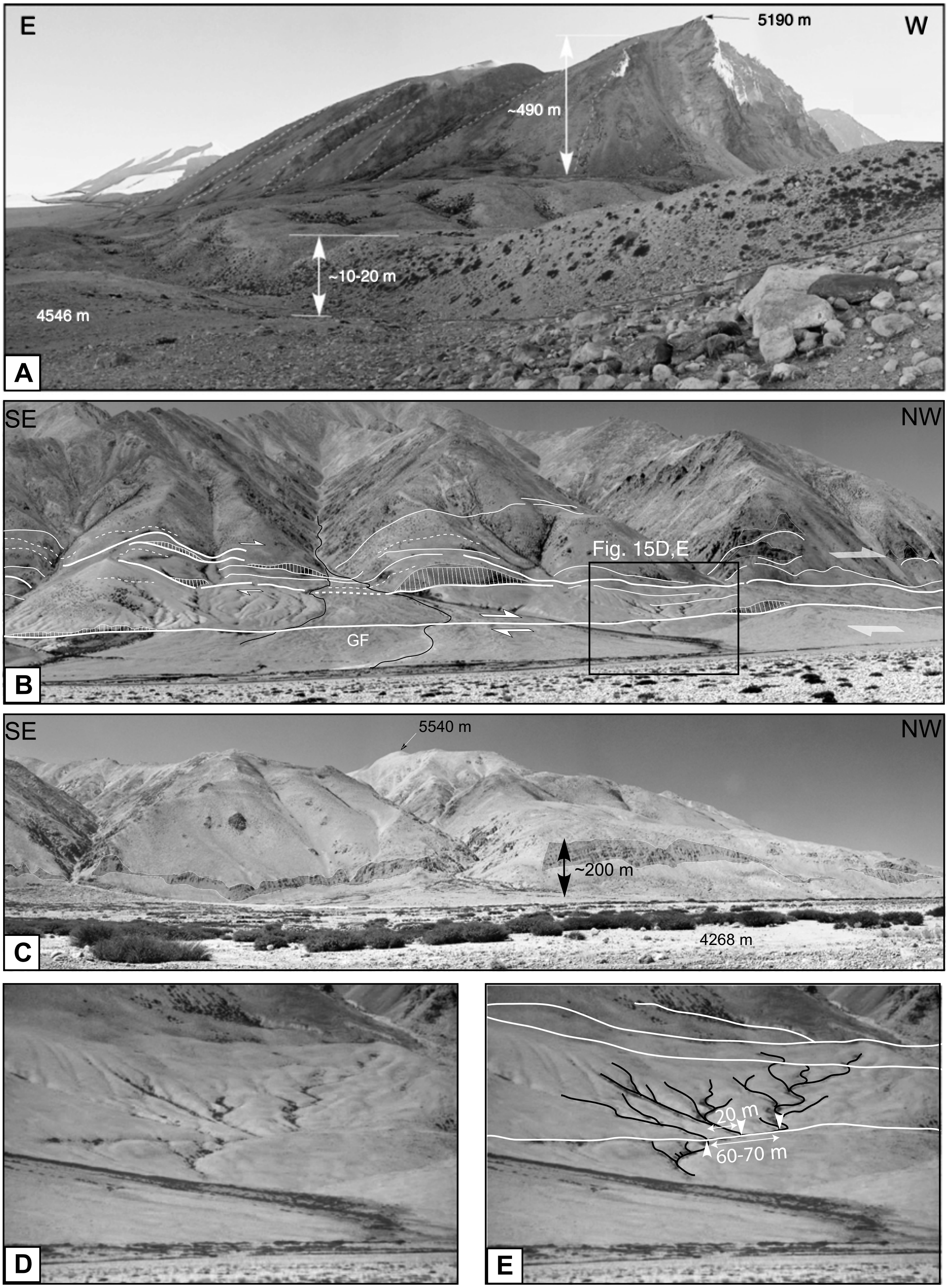

Figure 15. Field photos of Gar fan site (location in Fig. 3B). (A) Scarp along range-front fault west of Gar fan. (B) View of Gar fan and its vicinity. (C) Prominent N-S–striking normal fault that transfers fraction of total slip to range-front fault farther south. Cumulative scarp along this fault is as much as 200 m high. (D–E) Close-up of channel cumulative offsets (white arrows), ~20 and ~60–70 m.

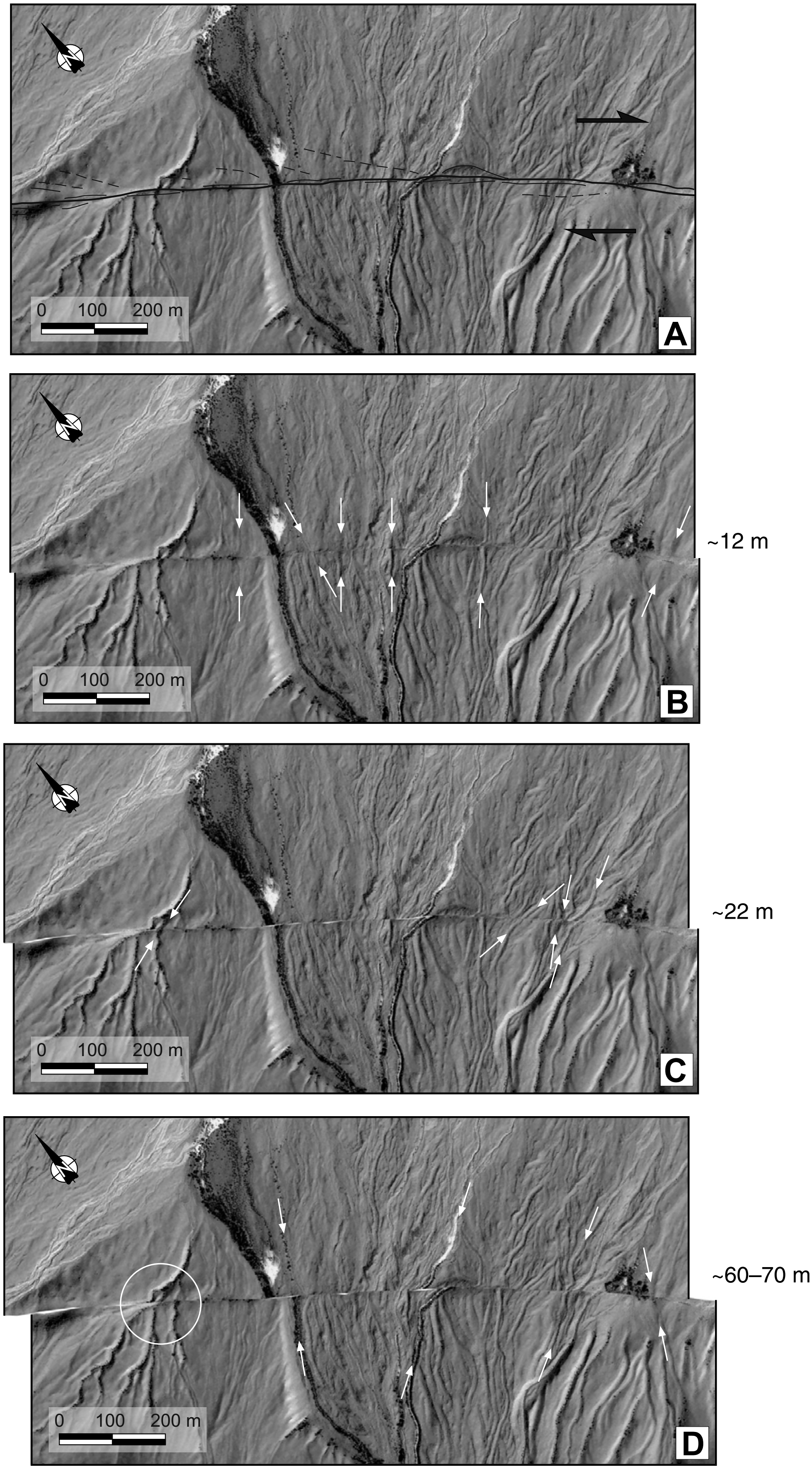

Figure 16. *Quickbird* satellite image (Google Earth) of Gar fan. (A) Gar fan site today and after back-slipping the image by 12 m (B), 22 m (C), and ~60–70 m (D), realigning several channels, as well as a drainage made of three channels to the north (circle in D).

faster than what we determined in this study, and it is ~11 mm/yr at time scales 40–200 ka, or if the mean age is favored (Chevalier et al., 2005a, 2005b), 3–5 times higher than what we just determined to the north. South of the town of Baer, after an ~30° bend in the fault, the dextral slip-rate across two of several fault branches observed in the Menshi-Kailas Basin (Chevalier et al., 2012), measured over a ca. 200 ka range, is >7.1 mm/yr at Menshi and >7.9 mm/yr at Kailas (these are minimum rates because of multiple active fault strands and because a significant vertical component has not been constrained). North of all these sites, just NW of Bangong Lake, the ~10 mm/yr slip-rate obtained with the same technique along the Tangtse and Bangong strands of the fault (4 ± 1 mm/yr since <14 ka [Brown et al., 2002] plus 5.6 mm/yr since 34 ka [Bohon, 2014]) is similar to the rate in the Menshi-Kailas Basin and to the highest rate at Manikala, if both strands were active at the same time. If the two strands were not active at the same time, the rate for each strand is also in agreement with what we determined in this study, as well as the minimum rate at Manikala.

How dextral motion on the faults at the Gar fan site is transferred farther south along the west side of the Gar Basin is most likely complex. It involves an interplay between oblique normal fault strands and strike-slip strands that vanish into the Gar Basin swamps. This may explain why the rate we determined at Gar fan is lower than at other places. Although we did not sample other surfaces in that area, one N-S–striking normal fault (Fig. 15C) is so prominent in the landscape that we infer it transfers a significant fraction of the total slip to the range-front fault system farther south. The cumulative scarp along this fault reaches 200 m, but its age cannot be assessed at this stage. More detailed work, including further dating and better topographic measurement (especially near the range front at sites Gun and Chaxikang), is needed to obtain firmer results and to quantify the dextral and vertical slip-rates on the range-front fault, which could slightly increase the slip-rates we obtain here.

Overall, the slip-rate from south of Bangong Lake to Kailas therefore appears to increase over the southernmost ~500 km of the Karakorum fault, from >3 mm/yr at Gun and Chaxi-

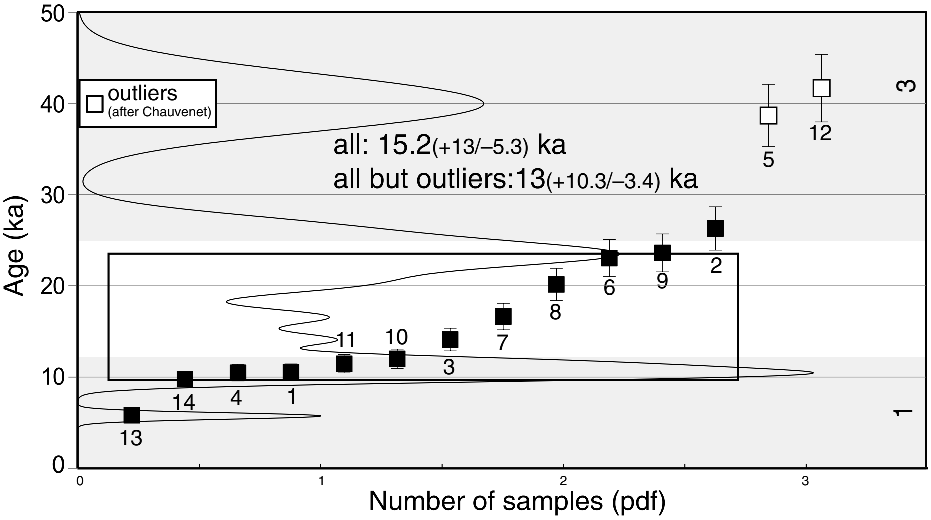

Figure 17. [10]Be ages and probability density function (pdf) distributions of surface samples from Gar fan at Gar fan site. Legend is same as in Figure 10.

kang to >5.4 mm/yr at Manikala to >7–8 mm/yr at Kailas. This is in contradiction with the inference from other studies (e.g., Searle et al., 1998; Murphy et al., 2000; Phillips et al., 2004; Valli et al., 2008; Robinson, 2009a; Styron et al., 2011; Kundu et al., 2014), which suggested that the rate and magnitude of offset might be decreasing toward its tips, like that observed along the Altyn Tagh fault (e.g., Meyer et al., 1996; Mériaux et al., 2005; Zhang et al., 2007; Chevalier et al., 2015) and the eastern Kunlun fault (e.g., Van der Woerd et al., 2002; Kirby et al., 2007). The southeastward increase in slip-rate may just reflect the fact that the rate is constrained across two branches of the fault (Chevalier et al., 2012) in the south, instead of just one, or it may possibly be due to the presence of active faults along the southern side of the Ayilari Range, absorbing some of the deformation north of Baer (Fig. 1). It may also be due to the presence of distributed extension north of the Karakorum fault, along the small conjugate strike-slip faults of central Tibet (Taylor et al., 2003). The approximation of a spatially constant slip-rate along the southern Karakorum fault (Menshi-Kailas segment) recently proposed by Chevalier et al. (2012), or its possible increase to the south (from Bangong Lake to Kailas) as suggested here, reinforces the idea that the Karakorum fault does not end just east of Kailas (e.g., Ratschbacher et al., 1994; Murphy et al., 2002) but extends to where its slip-rate decreases, i.e., further east along the Yarlung Zangbo suture (Peltzer and Tapponnier, 1988; Lacassin et al., 2004) and southeastward along the Gurla Mandhata–Humla fault system (e.g., Armijo et al., 1989; Chen et al., 2004; Lacassin et al., 2004; Murphy and Copeland, 2005; Styron et al., 2011; McCallister et al., 2014) and into western Nepal (Murphy et al., 2014).

Interestingly, we generally observe (Fig. 2) that geodetic and geologic rates may agree, within error, with the late Quaternary slip-rates. At a more detailed level, some rates appear to be slightly slower (Jade et al., 2004, 2010; Wright et al., 2004; Kundu et al., 2014), similar (Chen et al., 2004; Wang and Wright, 2012; Wang et al., 2012; Langstaff and Meade, 2013; Bohon, 2014; Kundu et al., 2014), or slightly higher (e.g., Banerjee and Bürgmann, 2002; Lacassin et al., 2004; Valli et al., 2007; S. Wang et al., 2009, 2011; Boutonnet et al., 2012, 2013; Gourbet et al., 2015) than what we obtain here. Chevalier et al. (2005a) suggested that this might be due to temporal variations as a result of the very different time spans involved (~15 yrs for geodetic and ~100 ka for late Quaternary, or Ma for geochronology studies). Robinson (2009b) instead suggested that the inferred active Karakorum fault termination at its intersection with the Longmu–Gozha Co fault (near Tangtse) might explain the possible slip-rate decrease from 10.7 mm/yr (Chevalier et al., 2005a, 2005b) >250 km south of the junction to 4 mm/yr (Brown et al., 2002) just south of it, but to which one may add 5.6 mm/yr (Bohon, 2014). Alternatively, the rates obtained at the different time scales (Fig. 2) might be viewed as in agreement with each other, with variations most likely due to measurement uncertainties or technical shortcomings. Indeed, InSAR data were not corrected for tropospheric effects, which are significant along the northern edge of Tibet (Elliott et al., 2008) and difficult to adjust for. Also, GPS data are extremely sparse in SW Tibet (only one station north of the Karakorum fault, "SHIQ", which was recently considered unreliable by Kundu et al. [2014] due to exceptionally high uncertainties), with the few existing stations located close to the fault, within the elastic deformation zone. Additionally, He and Chery (2008) argued that low GPS-derived slip-rates may be unreliable due to the way that geodetic measurements are extrapolated in time to obtain long-term slip-rates. Last, even though the Karakorum fault is one of the major active faults in Asia, its seismic activity has been quite low for M >5 earthquakes, maybe explaining observed low GPS/InSAR rates. Regarding long-term geologic rates, the minimum bounds of most studies seems to agree with rates determined at shorter time scales. On the contrary, the maximum bounds would be more in favor of an ~11 mm/yr rate (Fig. 2), i.e., twice as high as what late Quaternary rates suggest. This may indicate a recent decrease in fault motion, for which the precise timing and cause would remain to be constrained, possibly having strong implications on average slip-rate and total offset measurements.

The characteristics of the Karakorum fault, being the only right-lateral strike-slip fault in western Tibet, with continuity over more than 1000 km for the last >13–23 Ma, as well as having a significant slip-rate of >3–>8 mm/yr, attest to the important role of the Karakorum fault in the tectonics of Tibet, together with the left-lateral strike-slip Altyn Tagh and Kunlun faults. The evidence of a long-lasting, large-scale discontinuity tends to favor a model closer to the block model than to the continuum model as the most adequate description of lithospheric deformation north of the Himalayas, even though continuous-like deformation may occur at smaller scale within the blocks (e.g., Taylor et al., 2003).

The total geological offset along the Karakorum fault ranges from 66 km along the southernmost segment (Murphy et al., 2000, 2002) to >200–480 km (e.g., Ratschbacher et al., 1994; Matte et al., 1996; Lacassin et al., 2004; Valli et al., 2008; Gourbet et al., 2015) elsewhere, with intermediate values around 100–150 km (e.g., Gaudemer et al., 1989; Liu, 1993; Searle, 1996; Searle et al., 1998). Matching these long-term offsets with the initiation age of >13–23 Ma yields a long-term slip-rate of >2.9 mm/yr (if 66 km) or >8.7 mm/yr (if 200 km). These rates are consistent with what we determined at the late Quaternary time scale. The fact that the Karakorum fault may have been moving at a rate of >3 mm/yr over >13–23 Ma (or maybe >8 mm/yr) attests that it accommodates an important part of the deformation due to the India-Asia collision, together with the Altyn

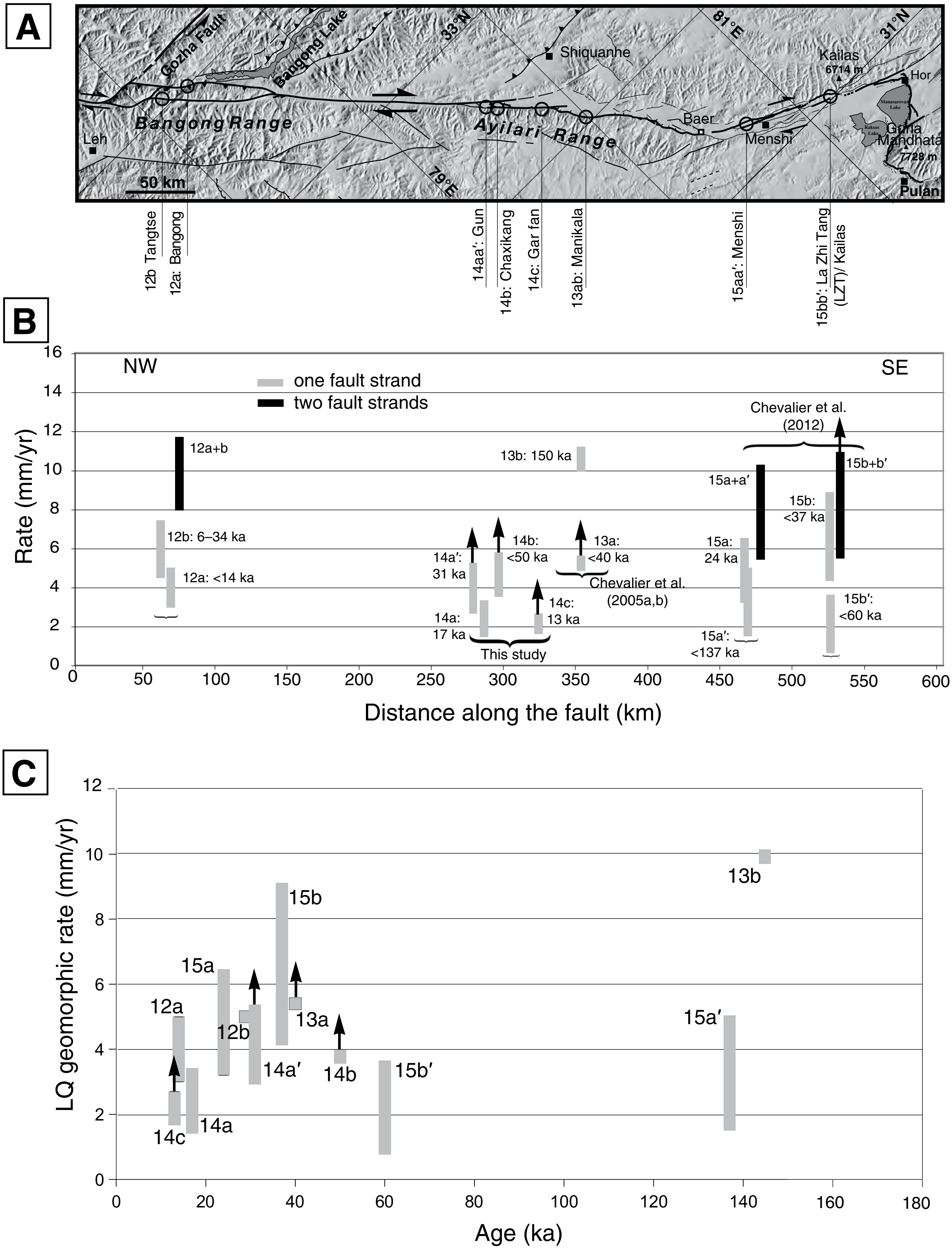

Figure 18. Slip-rates along Karakorum fault. (A–B) Slip-rates vs. distance along strike for southern half of the Karakorum fault, from Bangong Lake to Kailas. (C) Close-up of the late Quaternary (LQ) geomorphic rates vs. ages. See Table 1 for a list of the plotted studies and text for details. Black arrows indicate that the rates are minimum rates.

Tagh fault along the northern boundary of the Tibetan Plateau (moving at >9 mm/yr). In addition, the presence of smaller conjugate strike-slip faults in central Tibet moving at a rate of 1–2 mm/yr since 8–14 Ma (Taylor et al., 2003) confirms that the deformation in Tibet is primarily absorbed by large-scale strike-slip faults along the borders of Tibet, and to a lesser degree within the plateau. This confirms that Tibet is extruded to the east, and that deformation at first order is best described with a block model rather than with a continuous model.

CONCLUSIONS

By investigating three fluvial sites along the main branch of the Bangong-Chaxikang and Gar Basin segments of the Karakorum fault, representing a total of seven markers that are offset by up to ~200 m and spanning ~60 ka, we determined slip-rates of 3.1 mm/yr at the Gun site, of >3.4 mm/yr at Chaxikang, and >1.7 mm/yr at Gar fan. These rates are slightly lower than what was previously determined in the central segment of the Karakorum fault near Bangong Lake (Bangong 4 mm/yr [Brown et al., 2002] plus Tangtse 5.6 mm/yr [Bohon, 2014]; i.e., 10 mm/yr) and at Manikala (>5–11 mm/yr; Chevalier et al., 2005a, 2005b), as well as in the south along the Menshi-Kailas segment (two branches, >7–8 mm/yr; Chevalier et al., 2012). Even though these rates lie within the currently published range of slip-rates (0–11 mm/yr), including geodetic and long-term geologic (Ma) rates, they suggest a possible late Quaternary slip-rate increase toward the SE, along the southernmost 500 km of the Karakorum fault from Bangong Lake to Kailas. The Karakorum fault's length (>1000 km), initiation age (>13–23 Ma), and slip-rate (>3–8 mm/yr) confirm its important kinematic role in the tectonics of Tibet. The evidence that the Karakorum fault is thus a long-lasting, large-scale discontinuity north of the Himalayas, similar to the left-lateral Altyn Tagh and Kunlun strike-slip faults, is in favor of a deformation model for Tibet closer to a block model to describe lithospheric deformation north of the Himalayas. However, the still sparse and discrepant data along the Karakorum fault make it necessary to investigate more sites at different time scales to better refine its temporal and spatial kinematic behavior.

ACKNOWLEDGMENTS

This work was conducted under the auspices of the U.S. Department of Energy by the University of California, Lawrence Livermore National Laboratory (LLNL), as well as Institut National des Sciences de l'Univers and Centre National de la Recherche Scientifique (Paris, France). This study was also financially supported by the China Geological Survey (project 1212011121267) and the Basic Outlay of Scientific Research Work from the Ministry of Science and Technology, China (J1126).

Ikonos image acquisition was made possible thanks to special funding from University of California–Los Angeles (G. Peltzer's contract NAS 13–98048). We thank the Associate Editor F. Pazzaglia, and the reviewers M. Oskin and J. Harvey for their thorough and constructive comments.

REFERENCES CITED

Allen, C., Gillespie, A.R., Yuan, H., Sieh, K.E., Buchun, Z., and Chengnan, Z., 1984, Red River and associated faults, Yunnan Province, China: Quaternary geology, slip- rates and seismic hazard: Geological Society of America Bulletin, v. 95, p. 686–700, doi:10.1130/0016-7606(1984)95<686:RRAAFY>2.0.CO;2.

Anderson, R.S., Repka, J.L., and Dick, G.S., 1996, Explicit treatment of inheritance in dating depositional surfaces using in situ ^{10}Be and ^{26}Al: Geology, v. 24, p. 47–51, doi:10.1130/0091-7613(1996)024<0047:ETOIID>2.3.CO;2.

Applegate, P.J., Urban, N.M., Keller, K., Lowell, T.V., Laabs, B.J.C., Kelly, M.A., and Alley, R.B., 2012, Improved moraine age interpretations through explicit matching of geomorphic process models to cosmogenic nuclide measurements from single landforms: Quaternary Research, v. 77, p. 293–304, doi:10.1016/j.yqres.2011.12.002.

Armijo, R., Tapponnier, P., Mercier, J.L., and Han, T.L., 1986, Quaternary extension in southern Tibet: Field observations and tectonic implications: Journal of Geophysical Research, v. 91, p. 13,803–13,872, doi:10.1029/JB091iB14p13803.

Armijo, R., Tapponnier, P., and Tonglin, H., 1989, Late Cenozoic right-lateral strike-slip faulting in southern Tibet: Journal of Geophysical Research, v. 94, p. 2787–2838, doi:10.1029/JB094iB03p02787.

Avouac, J.P., and Tapponnier, P., 1993, Kinematic model of active deformation in central Asia: Geophysical Research Letters, v. 20, p. 895–898, doi:10.1029/93GL00128.

Balco, G., Stone, J.O., Lifton, N.A., and Dunai, T.J., 2008, A complete and easily accessible means of calculating surface exposure ages or erosion rates from ^{10}Be and ^{26}Al measurements: Quaternary Geochronology, v. 3, p. 174–195, doi:10.1016/j.quageo.2007.12.001.

Banerjee, P., and Bürgmann, R., 2002, Convergence across the northwest Himalaya from GPS measurements: Geophysical Research Letters, v. 29, p. 13, doi:10.1029/2002GL015184.

Bendick, R., Bilham, R., Freymueller, J., Larson, K., and Yin, G., 2000, Geodetic evidence for a low slip rate in the Altyn Tagh fault system: Nature, v. 404, p. 69–72, doi:10.1038/35003555.

Benedetti, L., and Van der Woerd, J., 2014, Cosmogenic nuclide dating of earthquakes, faults, and toppled blocks: Elements, v. 10, no. 5, p. 357–361.

Bennet, R.A., Friedrich, A.M., and Furlong, K.P., 2004, Codependent histories of the San Andreas and San Jacinto fault zones from inversion of fault displacement rates: Geology, v. 32, p. 961–964, doi:10.1130/G20806.1.

Bevington, P.R., and Robinson, D.K., 1992, Data Reduction and Error Analysis for the Physical Sciences: Boston, Massachusetts, WCB/McGraw-Hill, 328 p.

Bierman, P., 1994, Using in situ produced cosmogenic isotopes to estimate rates of landscape evolution: A review from the geomorphic perspective: Journal of Geophysical Research, v. 99, p. 13,885–13,896, doi:10.1029/94JB00459.

Bohon, W., 2014, Late Cenozoic–Recent Tectonics of the Southwestern Margin of the Tibetan Plateau, Ladakh, Northwest India [Ph.D. thesis]: Tempe, Arizona, Arizona State University, 205 p.

Boutonnet, E., Leloup, P.H., Arnaud, N., Paquette, J.L., and Hattori, D.W.J., 2012, Synkinematic magmatism, heterogeneous deformation, and progressive strain localization in a strike-slip shear zone. The case of the right-lateral Karakorum fault: Tectonics, v. 31, TC4012, doi:10.1029/2011TC003049.

Boutonnet, E., Leloup, P.H., Sassier, C., Gardien, V., and Ricard, Y., 2013, Ductile strain rate measurements document long-term strain localization in the continental crust: Geology, v. 41, no. 8, p. 819–822, doi:10.1130/G33723.1.

Briner, J.P., 2009, Moraine pebbles and boulders yield indistinguishable ^{10}Be ages: A case study from Colorado, USA: Quaternary Geochronology, v. 4, p. 299–305, doi:10.1016/j.quageo.2009.02.010.

Brown, E.T., Bendick, R., Bourles, D.L., Gaur, V., Molnar, P., Raisbeck, G.M., and Yiou, F., 2002, Slip rates of the Karakorum fault, Ladakh, India, determined using cosmic ray exposure dating of debris flows and moraines: Journal of Geophysical Research, v. 107, no. B9, p. 2192–2205, doi:10.1029/2000JB000100.

Brown, E.T., Molnar, P., and Bourlès, D.L., 2005, Comment on "Slip-rate measurements on the Karakorum fault may imply secular variations in fault motion": Science, v. 309, p. 1326b, doi:10.1126/science.1112508.

Brunel, M., Arnaud, N., Tapponnier, P., Pan, Y., and Wang, Y., 1994, Kongur Shan normal fault: Type example of mountain building assisted by extension (Karakoram fault, eastern Pamir): Geology, v. 22, p. 707–710, doi:10.1130/0091-7613(1994)022<0707:KSNFTE>2.3.CO;2.

Chen, Q., Freymueller, J.T., Yang, Z., Xu, C., Jiang, W., Wang, Q., and Liu, J., 2004, Spatially variable extension in southern Tibet based on GPS measurements: Journal of Geophysical Research, v. 109, B09401, doi:10.1029/2002JB002350.

Chen, Z., Burchfiel, B.C., Liu, Y., King, R.W., Royden, L.H., Tang, W., Wang, E., Zhao, J., and Zhang, X., 2000, Global positioning system measurements from eastern Tibet and their implications for India/Eurasia intercontinental deformation: Journal of Geophysical Research, v. 105, no. B7, p. 16,215–16,227, doi:10.1029/2000JB900092.

Chevalier, M.L., Ryerson, F.J., Tapponnier, P., Finkel, R., Van der Woerd, J., Li, H., and Liu, Q., 2005a, Slip-rate measurements on the Karakorum fault may imply secular variations in fault motion: Science, v. 307, no. 5708, p. 411–414, doi:10.1126/science.1105466.

Chevalier, M.L., Ryerson, F.J., Tapponnier, P., Finkel, R.C., Van Der Woerd, J., Li, Haibing, and Liu, Q., 2005b, Response to comment on "Slip-rate measurements on the Karakorum fault may imply secular variations in fault motion": Science, v. 309, p. 1326c, doi:10.1126/science.1112629.

Chevalier, M.L., Hilley, G., Tapponnier, P., Van Der Woerd, J., Liu-Zeng, J., Finkel, R.C., Ryerson, F.J., Li, H., and Liu, X., 2011a, Constraints on the late Quaternary glaciations in Tibet from cosmogenic exposure ages of moraine surfaces: Quaternary Science Reviews, v. 30, p. 528–554, doi:10.1016/j.quascirev.2010.11.005.

Chevalier, M.L., Li, H., Pan, J., Pei, J., Wu, F., Xu, W., Sun, Z., and Liu, D., 2011b, Fast slip rate along the northern end of the Karakorum fault system, western Tibet: Geophysical Research Letters, v. 38, L22309, doi:10.1029/2011GL049921.

Chevalier, M.L., Tapponnier, P., Van Der Woerd, J., Ryerson, F.J., Finkel, R.C., and Li, H., 2012, Spatially constant slip rate along the southern segment of the Karakorum fault since 200 ka: Tectonophysics, v. 530–531, p. 152–179, doi:10.1016/j.tecto.2011.12.014.

Chevalier, M.L., Pan, J., Li, H., Sun, Z., Liu, D., Pei, J., Xu, W., and Wu, C., 2015a, First tectonic-geomorphology study along the Longmu–Gozha Co fault system, western Tibet: Gondwana Research, doi:10.1016/j.gr.2015.03.008 (in press).

Chevalier, M.L., Pan, J., Li, H., Liu, D., and Wang, M., 2015b, Quantification of both normal and right-lateral late quaternary activity along the Kongur Shan extensional system, Chinese Pamir: Terra Nova (in press).

Cowgill, E., 2007, Impact of riser reconstructions on estimation of secular variation in rates of strike-slip faulting: Revisiting the Cherchen River site along the Altyn Tagh fault, NW China: Earth and Planetary Science Letters, v. 254, no. 3–4, p. 239–255, doi:10.1016/j.epsl.2006.09.015.

Cowgill, E., Gold, R.D., Chen, X., Wang, X.-F., Arrowsmith, J.R., and Southon, J.R., 2009, Low Quaternary slip rate reconciles geodetic and geologic rates along the Altyn Tagh fault, northwestern Tibet: Geology, v. 37, no. 7, p. 647–650, doi:10.1130/G25623A.1.

Desilets, D., and Zreda, M., 2003, Spatial and temporal distribution of secondary cosmic- ray nucleon intensities and applications to in-situ cosmogenic dating: Earth and Planetary Science Letters, v. 206, p. 21–42, doi:10.1016/S0012-821X(02)01088-9.

Desilets, D., Zreda, M., and Prabu, T., 2006, Extended scaling factors for in situ cosmogenic nuclides: New measurements at low latitude: Earth and Planetary Science Letters, v. 246, p. 265–276, doi:10.1016/j.epsl.2006.03.051.

Dunai, T.J., 2000, Scaling factors for production rates of in situ produced cosmogenic nuclides: A critical reevaluation: Earth and Planetary Science Letters, v. 176, p. 157–169, doi:10.1016/S0012-821X(99)00310-6.

Dunai, T.J., 2001, Influence of secular variation of the geomagnetic field on the production rates of in situ produced cosmogenic nuclides: Earth and Planetary Science Letters, v. 193, p. 197–212, doi:10.1016/S0012-821X(01)00503-9.

Dunai, T.J., 2010, Cosmogenic Nuclides Principles: Concepts and Applications in the Earth Surface Sciences: Cambridge, UK, Cambridge University Press, 198 p.

Elliott, J.R., Biggs, J., Parsons, B., and Wright, T.J., 2008, InSAR slip rate determination on the Altyn Tagh fault, northern Tibet, in the presence of topographically correlated atmospheric delays: Geophysical Research Letters, v. 35, L12309, doi:10.1029/2008GL033659.

England, P., and Molnar, P., 2005, Late Quaternary to decadal velocity fields in Asia: Journal of Geophysical Research, v. 110, B12401, doi:10.1029/2004JB003541.

Finkel, R.C., Owen, L.A., Barnard, P.L., and Caffee, M.W., 2003, Beryllium-10 dating of Mount Everest moraines indicates a strong monsoon influence and glacial synchroneity throughout the Himalaya: Geology, v. 31, p. 561–564, doi:10.1130/0091-7613(2003)031<0561:BDOMEM>2.0.CO;2.

Flesch, L., and Bendick, R., 2007, Present-day kinematics at the India-Asia collision zone: Comment: Geology, v. 35, p. e160, doi:10.1130/G24443C.1.

Friedrich, A.M., Wernicke, B.P., Niemi, N.A., Bennett, R.A., and Davis, J.L., 2003, Comparison of geodetic and geologic data from the Wasatch region, Utah, and implications for the spectral character of Earth deformation at periods of 10 to 10 million years: Journal of Geophysical Research, v. 108, no. B4, 2199, doi:10.1029/2001JB000682.

Gan, W., Zhang, P., Shen, Z.-K., Niu, Z., Wang, M., Wan, Y., Zhou, D., and Cheng, J., 2007, Present-day crustal motion within the Tibetan Plateau inferred from GPS measurements: Journal of Geophysical Research, v. 112, B08416, doi:10.1029/2005JB004120.

Gaudemer, Y., Tapponnier, P., and Turcotte, D.L., 1989, River offsets across active strike slip faults: Annales Tectonicae, v. 3, no. 2, p. 55–76.

Gaudemer, Y., Tapponnier, P., Meyer, B., Peltzer, G., Guo, S., Chen, Z., Dai, H., and Cifuentes, I., 1995, Partitioning of crustal slip between linked active faults in the eastern Qilian Shan, and evidence for a major seismic gap, the "Tianzhu gap," on the western Haiyuan fault, Gansu (China): Geophysical Journal International, v. 120, p. 599–645, doi:10.1111/j.1365-246X.1995.tb01842.x.

Gold, R.D., Cowgill, E., Arrowsmith, J.R., Gosse, J., Wang, X., and Chen, X., 2009, Riser diachroneity, lateral erosion, and uncertainty in rates of strike-slip faulting: A case study from Tuzidun along the Altyn Tagh fault, NW China: Journal of Geophysical Research, v. 114, B04401, doi:10.1029/2008JB005913.

Gold, R.D., Cowgill, E., Arrowsmith, J.R., Chen, X., Sharp, W.D., Cooper, K.M., and Wang, X.F., 2011, Faulted terrace risers place new constraints on the late Quaternary slip rate for the central Altyn Tagh fault, northwest Tibet: Geological Society of America Bulletin, v. 123, no. 5–6, p. 958–978, doi:10.1130/B30207.1.

Gourbet, L., Maheo, G., Leloup, P.H., Paquette, J.L., Sorrel, P., Henriquet, M., Liu, X., and Liu, X., 2015, Western Tibet relief evolution since the Oligo-Miocene: Gondwana Research, doi:10.1016/j.gr.2014.12.003 (in press).

Hallet, B., and Putkonen, J., 1994, Surface dating of dynamic landforms: Young boulders on aging moraines: Science, v. 265, p. 937–940, doi:10.1126/science.265.5174.937.

Hanks, T.C., and Thatcher, W., 2006, The slip-rate discrepancy for the Altyn Tagh fault: An example of epistemic uncertainty: San Francisco, California, American Geophysical Union, Fall meeting 2006, abstract T21E-03.

Harkins, N., Kirby, E., Shi, X., Wang, E., Burbank, D., and Fan, C., 2010, Millennial slip rates along the eastern Kunlun fault: Implications for the dynamics of intracontinental deformation in Asia: Lithosphere, v. 2, no. 4, p. 247–266, doi:10.1130/L85.1.

He, J., and Chery, J., 2008, Slip rates of the Altyn Tagh, Kunlun and Karakorum faults (Tibet) from 3D mechanical modeling: Earth and Planetary Science Letters, v. 274, p. 50–58, doi:10.1016/j.epsl.2008.06.049.

Hetzel, R., 2013, Active faulting, mountain growth, and erosion at the margins of the Tibetan Plateau constrained by in situ–produced cosmogenic nuclides: Tectonophysics, v. 582, p. 1–24, doi:10.1016/j.tecto.2012.10.027.

Heyman, J., Stroeven, A.P., Harbor, J., and Caffee, M.W., 2011, Too young or too old: Evaluating cosmogenic exposure dating based on an analysis of compiled boulder exposure ages: Earth and Planetary Science Letters, v. 302, p. 71–80, doi:10.1016/j.epsl.2010.11.040.

Houlié, N., and Phillips, R.J., 2013, Quaternary rupture behavior of the Karakoram fault and its relation to the dynamics of the continental lithosphere, NW Himalaya–western Tibet: Tectonophysics, v. 599, p. 1–7, doi:10.1016/j.tecto.2013.03.029.

Imbrie, J., Hays, J.D., Martinson, D.G., McIntyre, A., Mix, A.C., Morley, J.J., Pisias, N.G., Press, W., and Shackleton, N.J., 1984, The orbital theory of Pleistocene climate, *in* Berger, A.L., ed., Support from a Revised Chronology of the Marine δ^{18}O Record, in Milankovitch and Climate: Boston, Massachusetts, D. Reidel, p. 269–305.

Jade, S., Bhatt, B.C., Yang, Z., Bendick, R., Gaur, V.K., Molnar, P., Anand, M.B., and Kumar, D., 2004, GPS measurements from Ladakh Himalaya, India: Preliminary tests of plate-like or continuous deformation in Tibet: Geological Society of America Bulletin, v. 116, p. 1385–1391, doi:10.1130/B25357.1.

Jade, S., Raghavendra Rao, H.J., Vijayan, M.S.M., Gaur, V.K., Bhatt, B.C., Kumar, K., Jaganathan, S., Ananda, M.B., and Dileep Kumar, P., 2010, GPS-derived deformation rates in northwestern Himalaya and Ladakh: International Journal of Earth Sciences, v. 100, p. 1293–1301, doi:10.1007/s00531-010-0532-3.

King, G.C.P., Klinger, Y., Bowman, D., and Tapponnier, P., 2005, Slip-partitioned surface breaks for the Mw7.8, 2001 Kokoxili earthquake, China: Bulletin of the Seismological Society of America, v. 95, p. 731–738, doi:10.1785/0120040101.

Kirby, E., Harkins, N., Wang, E., Shi, X., Fan, C., and Burbank, D., 2007, Slip rate gradients along the eastern Kunlun fault: Tectonics, v. 26, TC2010, doi:10.1029/2006TC002033.

Klinger, Y., Xu, X., Tapponnier, P., Van der Woerd, J., Lasserre, C., and King, G.C.P., 2005, High-resolution satellite imagery mapping of the surface rupture and slip distribution of the Mw7.8, 14 November 2001 Kokoxili earthquake, Kunlun fault, northern Tibet, China: Bulletin of the Seismological Society of America, v. 95, p. 1970–1987, doi:10.1785/0120040233.

Kundu, B., Yadav, R.K., Bali, B.S., Chowdhury, S., and Gahalaut, V.K., 2014, Oblique convergence and slip partitioning in the NW Himalaya: Implications from GPS measurements: Tectonics, v. 33, p. 2013–2024, doi:10.1002/2014TC003633.

Lacassin, R., Valli, F., Arnaud, N., Leloup, P.H., Paquette, J.L., Li, H., Tapponnier, P., Chevalier, M.L., Guillot, S., Maheo, G., and Xu, Z., 2004, Large-scale geometry, offset and kinematic evolution of the Karakorum fault, Tibet: Earth and Planetary Science Letters, v. 219, p. 255–269, doi:10.1016/S0012-821X(04)00006-8.

Lal, D., 1991, Cosmic-ray labeling of erosion surfaces—In situ nuclide production rates and erosion models: Earth and Planetary Science Letters, v. 104, no. 2–4, p. 424–439, doi:10.1016/0012-821X(91)90220-C.

Lal, D., Harris, N., Sharma, K., Gu, Z., Ding, L., Liu, T., Dong, W., Caffee, M.W., and Jull, A., 2003, Erosion history of the Tibetan Plateau since the last interglacial: Constraints from the first studies of cosmogenic ^{10}Be from Tibetan bedrock: Earth and Planetary Science Letters, v. 217, p. 33–42, doi:10.1016/S0012-821X(03)00600-9.

Langstaff, M.A., and Meade, B.J., 2013, Edge-driven mechanical microplate models of strike-slip faulting in the Tibetan Plateau: Journal of Geophysical Research, v. 118, p. 1–11, doi:10.1002/jgrb.50272.

Le Dortz, K., Meyer, B., Sebrier, M., Braucher, R., Bourles, D., Benedetti, L., Nazari, H., and Foroutan, M., 2012, Interpreting scattered in situ produced cosmogenic nuclide depth-profile data: Quaternary Geochronology, v. 11, p. 98–115, doi:10.1016/j.quageo.2012.02.020.

Leloup, P.H., Arnaud, N., Lacassin, R., Kienas, J.R., Harrison, T.M., Phan Trong, T.T., Replumaz, A., and Tapponnier, P., 2001, New constraints on the structure, thermochronology, and timing of the Ailao Shan–Red River shear zone, SE Asia: Journal of Geophysical Research, v. 106, no. B4, p. 6683–6732, doi:10.1029/2000JB900322.

Li, H., Van der Woerd, J., Tapponnier, P., Klinger, Y., Xuexiang, Q., Jingsui, Y., and Yintang, Z., 2005, Slip rate on the Kunlun fault at Hongshui Gou, and recurrence time of great events comparable to the 14/11/2001, Mw ~7.9 Kokoxili earthquake: Earth and Planetary Science Letters, v. 237, no. 1–2, p. 285–299, doi:10.1016/j.epsl.2005.05.041.

Lifton, N., Bieber, J., Clem, J., Duldig, M., Evenson, P., Humble, J., and Pyle, R., 2005, Addressing solar modulation and long-term uncertainties in scaling secondary cosmic rays for in situ cosmogenic nuclide applications: Earth and Planetary Science Letters, v. 239, p. 140–161, doi:10.1016/j.epsl.2005.07.001.

Liu, Q., 1993, Paleoclimat et Contraintes Chronologiques sur les Mouvements Recent dans l'Ouest du Tibet: Failles du Karakorum et de Longmu Co–Gozha Co, Lacs en Pull-Apart de Longmu Co et de Sumxi Co [Ph.D. thesis]: Paris, Université Paris, v. VII, 358 p.

Loveless, J.P., and Meade, B.J., 2011, Partitioning of localized and diffuse deformation in the Tibetan Plateau from joint inversions of geologic and geodetic observations: Earth and Planetary Science Letters, v. 303, p. 11–24, doi:10.1016/j.epsl.2010.12.014.

Matmon, A., Schwartz, D.P., Haeussler, P.J., Finkel, R.C., Lienkaemper, J.J., Stenner, H.D., and Dawson, T.E., 2006, Denali fault slip rates and Holocene–late Pleistocene kinematics of central Alaska: Geology, v. 34, no. 8, p. 645–648, doi:10.1130/G22361.1.

Matte, P., Tapponnier, P., Arnaud, N., Bourjot, L., Avouac, J.P., Vidal, P., Liu, Q., Pan, Y., and Wang, Y., 1996, Tectonics of western Tibet, between the Tarim and the Indus: Earth and Planetary Science Letters, v. 142, p. 311–330, doi:10.1016/0012-821X(96)00086-6.

McCallister, A.T., Taylor, M.H., Murphy, M.A., Styron, R.H., and Stockli, D.F., 2014, Thermochronologic constraints on the late Cenozoic exhumation history of the Gurla Mandhata metamorphic core complex, southwestern Tibet: Tectonics, v. 33, p. 27–52, doi:10.1002/2013TC003302.

Meade, B., 2007a, Present-day kinematics at the India-Asia collision zone: Geology, v. 35, p. 81–84, doi:10.1130/G22924A.1.

Meade, B., 2007b, Present-day kinematics at the India-Asia collision zone: Reply: Geology, v. 36, doi:10.1130/G24640Y.1.

Mériaux, A.S., Ryerson, F.J., Tapponnier, P., Van der Woerd, J., Finkel, R., Xu, X.W., Xu, Z.Q., and Caffee, M., 2004, Rapid slip along the central Altyn Tagh fault: Morphochronologic evidence from Cherchen He and Sulamu Tagh: Journal of Geophysical Research, v. 109, B06401, doi:10.1029/2003JB002558.

Mériaux, A.S., Tapponnier, P., Ryerson, F.J., Xiwei, X., King, G., Van der Woerd, J., Finkel, R., Haibing, L., Caffee, M., Zhiqin, X., and Wenbin, C., 2005, The Aksay segment of the northern Altyn Tagh fault: Tectonic geomorphology, landscape evolution, and Holocene slip rate: Journal of Geophysical Research, v. 110, no. B4, p. 1–32, doi:10.1029/2004JB003210.

Mériaux, A.S., Sieh, K., Finkel, R.C., Rubin, C.M., Taylor, M.H., Meltzner, A.J., and Ryerson, F.J., 2009, Kinematic behavior of southern Alaska constrained by westward decreasing postglacial slip rates on the Denali fault, Alaska: Journal of Geophysical Research, v. 114, B03404, doi:10.1029/2007JB005053.

Mériaux, A.S., Van der Woerd, J., Tapponnier, P., Ryerson, F.J., Finkel, R.C., Lasserre, C., and Xu, X., 2012, The Pingding segment of the Altyn Tagh fault (91 E): Holocene slip-rate determination from cosmogenic radionuclide dating of offset fluvial terraces: Journal of Geophysical Research, v. 117, B09406, doi:10.1029/2012JB009289.

Meyer, B., Tapponnier, P., Gaudemer, Y., Peltzer, G., Guo, S.M., and Chen, Z.T., 1996, Rate of left-lateral movement along the easternmost segment of the Altyn Tagh fault, east of 96 E (China): Geophysical Journal International, v. 124, p. 29–44, doi:10.1111/j.1365-246X.1996.tb06350.x.

Murphy, M.A., and Copeland, P., 2005, Transtensional deformation in the central Himalaya and its role in accommodating growth of the Himalayan orogen: Tectonics, v. 24, TC4012, doi:10.1029/2004TC001659.

Murphy, M.A., Yin, A., Kapp, P., Harrison, T.M., Lin, D., and Guo, J.H., 2000, Southward propagation of the Karakoram fault system, southwest Tibet: Timing and magnitude of slip: Geology, v. 28, p. 451–454, doi:10.1130/0091-7613(2000)28<451:SPOTKF>2.0.CO;2.

Murphy, M.A., Yin, A., Kapp, P., Harrison, T.M., Manning, C.E., Ryerson, F.J., Lin, D., and Jinghui, G., 2002, Structural evolution of the Gurla Mandhata detachment system, southwest Tibet: Implications for the eastward extent of the Karakoram fault system: Geological Society of America Bulletin, v. 114, p. 428–447, doi:10.1130/0016-7606(2002)114<0428:SEOTGM>2.0.CO;2.

Murphy, M.A., Taylor, M.H., Gosse, J., Silver, C.R.P., Whipp, D.M., and Beaumont, C., 2014, Limit of strain partitioning in the Himalaya marked by large earthquakes in western Nepal: Nature Geoscience, v. 7, p. 38–42, doi:10.1038/NGEO2017.

Owen, L.A., Caffee, M.W., Finkel, R.C., and Seong, Y.B., 2008, Quaternary glaciation of the Himalayan-Tibetan orogen: Journal of Quaternary Science, v. 23, p. 513–531, doi:10.1002/jqs.1203.

Owen, L.A., Yi, C., Finkel, R.C., Davis, N.K., 2010, Quaternary glaciation of Gurla Mandhata (Naimon'anyi): Quaternary Science Reviews, v. 29, p. 1817–1830, doi:10.1016/j.quascirev.2010.03.017.

Owen, L.A., Chen, J., Hedrick, K.A., Caffee, M.W., Robinson, A.C., Schoenbohm, L.M., Yuan, Z., Li, W., Imrecke, D.B., and Liu, J., 2012, Quaternary glaciation of the Tashkurgan Valley, southeast Pamir: Quaternary Science Reviews, v. 47, p. 56–72, doi:10.1016/j.quascirev.2012.04.027.

Peltzer, G., and Tapponnier, P., 1988, Formation and evolution of strike-slip faults, rifts, and basins during the India-Asia collision: An experimental approach: Journal of Geophysical Research, v. 93, no. 12, p. 15,085–15,117, doi:10.1029/JB093iB12p15085.

Peltzer, G., Tapponnier, P., and Armijo, R., 1989, Magnitude of late Quaternary left- lateral movement along the north edge of Tibet: Science, v. 246, p. 1285–1289, doi:10.1126/science.246.4935.1285.

Perfettini, H., and Avouac, J.P., 2004, Postseismic relaxation driven by brittle creep: A possible mechanism to reconcile geodetic measurements and the decay rate of aftershocks, application to the Chi-Chi earthquake, Taiwan: Journal of Geophysical Research, v. 109, B02304, doi:10.1029/2003JB002488.

Perrineau, A., Van der Woerd, J., Gaudemer, Y., Liu-Zeng, J., Pik, R., Tapponnier, P., Thuizat, R., and Zheng, R., 2011, Incision rate of the Yellow River in northeastern Tibet constrained by ^{10}Be and ^{26}Al cosmogenic isotope dating of fluvial terraces: Implications for catchment evolution and plateau building, *in* Gloaguen, R., and Ratschbacher, L., eds., Growth and Collapse of the Tibetan Plateau: Geological Society of London Special Publication 353, p. 189–219, doi:10.1144/SP353.10

Phillips, R.J., Parrish, R.R., and Searle, M.P., 2004, Age constraints on ductile deformation and long-term slip rates along the Karakoram fault zone, Ladakh: Earth and Planetary Science Letters, v. 226, p. 305–319, doi:10.1016/j.epsl.2004.07.037.

Raterman, N.S., Cowgill, E., and Lin, D., 2007, Variable structural style along the Karakoram fault explained using triple junction analysis of intersecting faults: Geosphere, v. 3, p. 71–85, doi:10.1130/GES00067.s1.

Ratschbacher, L., Frisch, W., Liu, G., and Chen, C.C., 1994, Distributed deformation in southern and western Tibet during and after the India-Asian collision: Journal of Geophysical Research, v. 99, p. 19,917–19,945, doi:10.1029/94JB00932.

Replumaz, A., and Tapponnier, P., 2003, Reconstruction of the deformed collision zone between India and Asia by backward motion of lithospheric blocks: Journal of Geophysical Research, v. 108, 2285, doi:10.1029/2001JB000661.

Replumaz, A., Lacassin, R., Tapponnier, P., and Leloup, P., 2001, Large river offsets and Plio-Quaternary dextral slip-rate on the Red River fault (Yunnan, China): Journal of Geophysical Research, v. 106, p. 819–836, doi:10.1029/2000JB900135.

Ritz, J.F., Vassallo, R., Braucher, R., Brown, E.T., Carretier, S., and Bourles, D.L., 2006, Using in situ–produced ^{10}Be to quantify active tectonics in the Gurvan Bogd mountain range (Gobi-Altay, Mongolia), *in* Siame, L., Bourles, D.L., and Brown, E.T., eds., In Situ–Produced Cosmogenic Nuclides and Quantification of Geological Processes: Geological Society of America Special Paper 415, p. 87–110.

Robinson, A.C., 2009a, Geologic offsets across the northern Karakorum fault: Implications for its role and terrane correlations in the western Himalayan–Tibetan orogen: Earth and Planetary Science Letters, v. 279, p. 123–130, doi:10.1016/j.epsl.2008.12.039.

Robinson, A.C., 2009b, Evidence against Quaternary slip on the northern Karakorum fault suggests kinematic reorganization at the western end of the Himalayan-Tibetan orogen: Earth and Planetary Science Letters, v. 286, p. 158–170, doi:10.1016/j.epsl.2009.06.025.

Robinson, A.C., Yin, A., Manning, C.E., Harrison, T.M., Zhang, S.H., and Wang, X.F., 2007, Cenozoic evolution of the eastern Pamir: Implications for strain accommodation mechanisms at the western end of the Himalayan-Tibetan orogen: Geological Society of America Bulletin, v. 119, no. 7–8, p. 882–896, doi:10.1130/B25981.1.

Robinson, A.C., Owen, L.A., Chen, J., Schoenbohm, L.M., Hedrick, K.A., Blisniuk, K., Sharp, W.D., Imrecke, D.B., Li, W., Yuan, Z., Caffee, M.W., and Mertz-Kraus, R., 2015, No late Quaternary strike-slip motion along the northern Karakoram fault: Earth and Planetary Science Letters, v. 409, p. 290–298, doi:10.1016/j.epsl.2014.11.011.

Rutter, E.H., Faulkner, D.R., Brodie, K.H., Phillips, R.J., and Searle, M.P., 2007, Rock deformation processes in the Karakoram fault zone, eastern Karakoram, Ladakh, NW India: Journal of Structural Geology, v. 29, p. 1315–1326, doi:10.1016/j.jsg.2007.05.001.

Ryerson, F.J., Tapponnier, P., Finkel, R.C., Mériaux, A.S., Van der Woerd, J., Lasserre, C., Chevalier, M.L., Xiwei, X., Li, H., and King, G.C.P., 2006, Applications of morphochronology to the active tectonics of Tibet, *in* Siame, L.L., Bourles, D.L., and Brown, E.T. ,eds., Application of Cosmogenic Nuclides to the Study of Earth Surface Processes: The Practice and the Potential: Geological Society of America Special Paper 415, p. 61–86, doi:10.1130/2006.2415(05).

Sanchez, V.I., Murphy, M.A., Dupre, M.R., Ding, L., and Zhang, R., 2010, Structural evolution of the Neogene Gar Basin, western Tibet: Implications for releasing bend development and drainage patterns: Geological Society of America Bulletin, v. 122, no. 5/6, p. 926–945, doi:10.1130/B26566.1.

Savage, J.C., and Prescott, W.H., 1978, Asthenosphere readjustment and the earthquake cycle: Journal of Geophysical Research, v. 83, p. 3369–3376, doi:10.1029/JB083iB07p03369.

Schmidt, S., Hetzel, R., Kuhlmann, J., Mingorance, F., and Ramos, V.A., 2011, A note of caution on the use of boulders for exposure dating of depositional surfaces: Earth and Planetary Science Letters, v. 302, p. 60–70, doi:10.1016/j.epsl.2010.11.039.

Searle, M.P., 1996, Geological evidence against large-scale pre-Holocene offsets along the Karakoram fault: Implications for the limited extrusion of the Tibetan Plateau: Tectonics, v. 15, p. 171–186, doi:10.1029/95TC01693.

Searle, M.P., Weinberg, R.F., and Dunlap, W.J., 1998, Transpressional tectonics along the Karakoram fault zone, northern Ladakh: Constraints on Tibetan extrusion, *in* Holdsworth, R.E., et al., eds., Continental Transpressional and Transtensional Tectonics: Geological Society of London Special Publication 74, p. 307–326, doi:10.1144/GSL.SP.1998.135.01.20.

Segall, P., 2002, Integrating geologic and geodetic estimates of slip rate on the San Andreas fault system: International Geology Review, v. 44, p. 62–82, doi:10.2747/0020-6814.44.1.62.

Stone, J.O., 2000, Air pressure and cosmogenic isotope production: Journal of Geophysical Research, v. 105, no. B10, p. 23,753–23,759, doi:10.1029/2000JB900181.

Strobl, M., Hetzel, R., Niedermann, S., Ding, L., and Zhang, L., 2012, Landscape evolution of a bedrock peneplain on the southern Tibetan Plateau revealed by in situ–produced cosmogenic ^{10}Be and ^{21}Ne: Geomorphology, v. 153–154, p. 192–204, doi:10.1016/j.geomorph.2012.02.024.

Styron, R.H., Taylor, M.H., and Murphy, M.A., 2011, Oblique convergence, arc-parallel extension, and the role of strike-slip faulting in the High Himalaya: Geosphere, v. 7, no. 2, p. 582–596, doi:10.1130/GES00606.1.

Tapponnier, P., Xu, Z., Roger, F., Meyer, B., Arnaud, N., Wittlinger, G., and Yang, J., 2001, Oblique stepwise rise and growth of the Tibet Plateau: Science, v. 294, no. 5547, p. 1671–1677, doi:10.1126/science.105978.

Taylor, J.R., 1997, An Introduction to Error Analysis. The Study of Uncertainties in Physical Measurements (2nd ed.): Herndon, Virginia, University Science Books, 327 p.

Taylor, M., Yin, A., Ryerson, F., Kapp, P., and Ding, L., 2003, Conjugate strike slip fault accommodates coeval north-south shortening and east-west extension along the Bangong-Nujiang suture zone in central Tibet: Tectonics, v. 22, 1044, doi:10.1029/2002TC001361.

Thatcher, W., 2007, Microplate model for the present-day deformation of Tibet: Journal of Geophysical Research, v. 112, B05411, doi:10.1029/2005JB004244.

Thatcher, W., 2009, How the continents deform: The evidence from tectonic geodesy: Annual Review of Earth and Planetary Sciences, v. 37, p. 237–262, doi:10.1146/annurev.earth.031208.100035.

Valli, F., Arnaud, N., Leloup, P.H., Sobel, E.R., Maheo, G., Lacassin, R., Guillot, S., Li, H., Tapponnier, P., and Xu, Z., 2007, Twenty million years of continuous deformation along the Karakorum fault, western Tibet: A thermochronological analysis: Tectonics, v. 26, TC4004, doi:10.1029/2005TC001913.

Valli, F., Leloup, P.H., Paquette, J.L., Arnaud, N., Li, H., Tapponnier, P., Lacassin, R., Guillot, S., Liu, D., Deloule, E., Xu, Z., and Maheo, G., 2008, New U-Th/Pb constraints on timing of shearing and long-term slip-rate on the Karakorum fault: Tectonics, v. 27, TC5007, doi:10.1029/2007TC002184.

Van der Woerd, J., Ryerson, F.J., Tapponnier, P., Gaudemer, Y., Finkel, R., Mériaux, A.S., Caffee, M., Guoguang, Z., and Qunlu, H., 1998, Holocene left slip rate determined by cosmogenic surface dating on the Xidatan segment of the Kunlun fault (Qinghai, China): Geology, v. 26, p. 695–698, doi:10.1130/0091-7613(1998)026<0695:HLSRDB>2.3.CO;2.

Van der Woerd, J., Ryerson, F.J., Tapponnier, P., Mériaux, A.S., Gaudemer, Y., Meyer, B., Finkel, R., Caffee, M., Guoguang, Z., and Zhiqin, X., 2000, Uniform slip rates across the Kunlun fault: Implications for seismic behavior and large-scale tectonics: Geophysical Research Letters, v. 27, no. 16, p. 2353–2356, doi:10.1029/1999GL011292.

Van der Woerd, J., Tapponnier, P., Ryerson, F.J., Mériaux, A.S., Meyer, B., Gaudemer, Y., Finkel, R.C., Caffee, M.W., Zhao, G., and Xu, Z., 2002, Uniform postglacial slip-rate along the central 600 km of the Kunlun fault (Tibet), from ^{26}Al, ^{10}Be and ^{14}C dating of riser offsets, and climatic origin of the regional morphology: Geophysical Journal International, v. 148, p. 356–388, doi:10.1046/j.1365-246x.2002.01556.x.

Vassallo, R., Ritz, J.G., and Carretier, S., 2011, Control of geomorphic processes on ^{10}Be concentrations in individual clasts: Complexity of the exposure history in Gobi-Altay

Range (Mongolia): Geomorphology, v. 135, no. 1–2, p. 35–47, doi:10.1016/j.geomorph.2011.07.023.

Wallace, K., Yin, G., and Bilham, R., 2004, Inescapable slow slip on the Altyn Tagh fault: Geophysical Research Letters, v. 31, p. 1–4, doi:10.1029/2004GL019724.

Wang, H., and Wright, T.J., 2012, Satellite geodetic imaging reveals internal deformation of western Tibet: Geophysical Research Letters, v. 39, L07303, doi:10.1029/2012GL051222.

Wang, H., Liu, M., Cao, J., Shen, X., and Zhang, G., 2011, Slip rates and seismic moment deficits on major active faults in mainland China: Journal of Geophysical Research, v. 116, B02405, doi:10.1029/2010JB007821.

Wang, Q., Zhang, P., Freymueller, J., Bilham, R., Larson, K., Lai, X., You, X., Niu, Z., Wu, J., Li, Y., Liu, J., Yang, Z., and Chen, Q., 2001, Present-day crustal deformation in China constrained by global positioning system measurements: Science, v. 294, p. 574–577, doi:10.1126/science.1063647.

Wang, S., Fang, X., Lai, Q., Zheng, D., and Wang, Y., 2009, New radiometric dating constrains the time for initiation of the Karakorum fault zone (KFZ), SW Tibet: Tectonophysics, v. 475, p. 503–513, doi:10.1016/j.tecto.2009.06.016.

Wang, S., Wang, E., Fang, X., and Lai, Q., 2011, U-Pb SHRIMP and $^{40}Ar/^{39}Ar$ ages constrain the deformation history of the Karakoram fault zone (KFZ), SW Tibet: Tectonophysics, v. 509, p. 208–217, doi:10.1016/j.tecto.2011.06.011.

Wang, S., Wang, C., Phillips, R.J., Murphy, M.A., Fang, X., and Yue, Y., 2012, Displacement along the Karakoram fault, NW Himalaya, estimated from LA-ICP-MS U-Pb dating of offset geologic markers: Earth and Planetary Science Letters, v. 337–338, p. 156–163, doi:10.1016/j.epsl.2012.05.037.

Wright, T.J., Parsons, B., England, P.C., and Fielding, E.J., 2004, InSAR observations of low slip rates on the major faults of western Tibet: Science, v. 305, no. 5681, p. 236–239, doi:10.1126/science.1096388.

Xu, X., Tapponnier, P., Van Der Woerd, J., Ryerson, F.J., Wang, F., Zheng, R., Chen, W., Ma, W., Yu, G., Chen, G., and Mériaux, A.S., 2005, Late Quaternary sinistral slip rate along the Altyn Tagh fault and its structural transformation model: Science in China, v. 48, p. 384–397, doi:10.1360/02yd0436.

Yue, Y., Ritts, B.D., Graham, S.A., Wooden, J.L., Gehrels, G.E., and Zhang, Z., 2003, Slowing extrusion tectonics: Lowered estimate of post–early Miocene slip rate for the Altyn Tagh fault: Earth and Planetary Science Letters, v. 217, p. 111–122, doi:10.1016/S0012-821X(03)00544-2.

Zechar, J.D., and Frankel, K.L., 2009, Incorporating and reporting uncertainties in fault slip rates: Journal of Geophysical Research, v. 114, B12407, doi:10.1029/2009JB006325.

Zhang, P.Z., Shen, Z., Wang, M., Gan, W., Bürgmann, R., Molnar, P., Wang, Q., Niu, Z., Sun, J., Wu, J., Hanrong, S., and Xinzhao, Y., 2004, Continuous deformation of the Tibetan Plateau from global positioning system data: Geology, v. 32, no. 9, p. 809–812, doi:10.1130/G20554.1.

Zhang, P.Z., Molnar, P., and Xu, X., 2007, Late Quaternary and present-day rates of slip along the Altyn Tagh fault, northern margin of the Tibetan Plateau: Tectonics, v. 26, TC5010, p. 1–24, doi:10.1029/2006TC002014.

Science Editor: David Ian Schofield
Associate Editor: Frank J. Pazzaglia

Manuscript Received 5 January 2015
Revised Manuscript Received 20 May 2015
Manuscript Accepted 29 June 2015

Printed in the USA

Geological Society of America Bulletin

Late Quaternary slip-rate along the central Bangong-Chaxikang segment of the Karakorum fault, western Tibet

Marie-Luce Chevalier, Jérôme Van der Woerd, Paul Tapponnier, Haibing Li, Frederick J. Ryerson and Robert C. Finkel

Geological Society of America Bulletin published online 29 July 2015;
doi: 10.1130/B31269.1

Notes